Semiconductor ultraviolet detectors

M. Razeghi[a] and A. Rogalski[b]
Center for Quantum Devices, Department of Electrical Engineering and Computer Science, Northwestern University, Evanston, Illinois 60201

(Received 7 September 1995; accepted for publication 12 January 1996)

In this review article a comprehensive analysis of the developments in ultraviolet (UV) detector technology is described. At the beginning, the classification of UV detectors and general requirements imposed on these detectors are presented. Further considerations are restricted to modern semiconductor UV detectors, so the basic theory of photoconductive and photovoltaic detectors is presented in a uniform way convenient for various detector materials. Next, the current state of the art of different types of semiconductor UV detectors is presented. Hitherto, the semiconductor UV detectors have been mainly fabricated using Si. Industries such as the aerospace, automotive, petroleum, and others have continuously provided the impetus pushing the development of fringe technologies which are tolerant of increasingly high temperatures and hostile environments. As a result, the main efforts are currently directed to a new generation of UV detectors fabricated from wide band-gap semiconductors the most promising of which are diamond and AlGaN. The latest progress in development of AlGaN UV detectors is finally described in detail. © *1996 American Institute of Physics.* [S0021-8979(96)06110-7]

TABLE OF CONTENTS

GLOSSARY OF FREQUENTLY USED SYMBOLS

a	lattice constant
A	detector area
b	electron to hole mobility ratio
c	speed of light
D, D_a, D_e, D_h	diffusion coefficient, ambipolar, of electrons, of holes
D^*, D^*_{BLIP}	detectivity, background limited
E_g, E_F, E_t	energy gap, Fermi energy, trap level energy
Δf	bandwidth
G	recombination rate
g	optical gain
$h, \hbar$	Planck's constant $h/2\pi$
$I, I_e, I_h, I_{\mathrm{ph}}$	current, of electrons, of holes, photocurrent
$I_D, I_{\mathrm{GR}}, I_T, I_n$	diffusion, generation–recombination, tunneling, and noise current
I_d, I_s	dark, saturation current

[a]Electronic mail: razeghi@eecs.nwu.edu
[b]Present address: Institute of Technical Physics, Military University of Technology, 01-489 Warsaw, Kaliskiego 2, Poland.

$J, J_e, J_h, J_{\text{ph}}$	current density, of electrons, of holes, photocurrent density
k	Boltzmann's constant
l	length
L, L_e, L_h	diffusion length, of electrons, of holes
m	free electron mass
m^*, m_c^*, m_n^*	effective mass, of electrons, of holes
n, n_i	electron and intrinsic carrier concentration
$n_0, n_n, n_p, \Delta n$	equilibrium electron concentration, majority and minority electron concentration, excess free electrons
N_a, N_d	concentration of acceptors, of donors
NEP	noise equivalent power
$p, p_0, p_p, p_n, \Delta p$	hole concentration, equilibrium, majority and minority hole concentration, excess free holes
q	electron charge
r	surface reflectance
R, R_L, R_s	resistance, load, series
R_0	zero bias detector resistance
R_i, R_v	current and voltage responsivity
s	surface recombination
t	thickness
T	temperature
$v, v_d, v_a, v_{\text{th}}$	velocity, drift, ambipolar, saturation, and thermal carrier
$V, V_b, V_{\text{bi}}, V_n$	electrical voltage, bias, built-in and noise
w	width
x	alloy composition, distance variable
α	absorption coefficient
β	coefficient of I–V diode characteristic
ε_0	permittivity of space
$\varepsilon, \varepsilon_0, \varepsilon_\infty$	dielectric coefficient, relative static and optical
η	quantum efficiency
$\lambda, \lambda_p, \lambda_c$	wavelength, peak wavelength, cutoff wavelength
ν	frequency
μ, μ_e, μ_h	mobility of carriers, of electrons, of holes
$\tau, \tau_e, \tau_h, \tau_{\text{ef}}$	carrier lifetime, of electrons, of holes and effective lifetime
$\tau_{\text{RC}}, \tau_d, \tau_s$	response time limited by RC, diffusion, and transit time
τ_0	carrier lifetime in depletion junction region
Φ_B, Φ_s	background, signal photon flux
ϕ	work function
Ψ	barrier potential
ω	angular frequency

I. INTRODUCTION

The ultraviolet (UV) region is commonly divided into the following subdivisions. These names are widely used and are recommended:

near ultraviolet	NUV	400–300 nm
mid ultraviolet	MUV	300–200 nm
far ultraviolet	FUV	200–100 nm
extreme ultraviolet	EUV	100–10 nm

In addition to the above names, the following names for wavelength regions may be encountered:

vacuum ultraviolet	VUV	200–10 nm
deep ultraviolet	DUV	350–190 nm
ultraviolet-A	UV-A	400–320 nm
ultraviolet-B	UV-B	320–280 nm

Again, it must be emphasized that these appear to be the most common names and wavelength limits, but others will be found.

Ultraviolet research began in the latter half of the 19th century, when the invisible radiation beyond the blue end of the visible spectrum began to receive attention. It was soon realized that the Earth's atmosphere set limitations on ultraviolet research. For solar and celestial observations, stratospheric ozone limited the wavelengths reaching the surface of the Earth to about 300 nm. Spectrographs carried to higher altitudes on mountains gave intriguing evidence that solar and stellar emissions continued to shorter wavelengths. In laboratory spectrographs, atmospheric molecular oxygen absorption limited the useful lower wavelengths to about 200 nm, unless the spectrograph could be placed in a vacuum chamber. The wavelengths shorter than 200 nm thus came to be called the vacuum ultraviolet. Because of the lack of good vacuum pumps and associated technology, research was difficult and not widely done. In addition to atmospheric limitations, optical methods used in the visible failed in the ultraviolet because of the lack of materials having good transmissivity and reflectivity. In the beginning of the 1880s, Rowland and co-workers developed concave diffraction gratings and discovered the Rowland circle mount for vacuum spectrographs. This was a great step forward, since only single reflection and no transmission were needed to obtain spectra on a photographic plate. Vacuum ultraviolet spectrography was pioneered by Schumann, Lyman, and others in the early decades of this century. The lack of suitable windows, filters, gratings, calibration standards, light sources, and vacuum pumps resulted in difficulties in experimentation. The next large stimulus occurred after World War II, when it was possible to use first sounding rockets and then satellites to investigate the Earth's upper atmosphere and to make solar and astronomical observations without interference by the atmosphere. These applications areas opened up the need for better instrumentation, including better windows, gratings, filters, detectors, and light sources as well as improved spectroscopy of the atoms, molecules, and ions of planetary and stellar atmospheres and reliable standards for calibrations.

The major constituents of the terrestrial atmosphere are strong absorbers of radiation at wavelengths below 300 nm. Radiation of mid ultraviolet (MUV) wavelengths between 200 and 300 nm is absorbed primarily by ozone while molecular oxygen is the major absorber at far ultraviolet (FUV) between 110 and 250 nm. Consequently, at wavelengths below about 200 nm, the use of evacuated instrumentation is mandatory. At extreme ultraviolet (EUV) wavelengths of 110 nm, atomic and molecular gases become strong absorbers.

Several books from the mid 1960s describe the ultraviolet technology of this time. These books are on vacuum ultraviolet spectroscopic techniques,[1] the middle ultraviolet [near ultraviolet (NUV) and MUV, generally],[2] ultraviolet

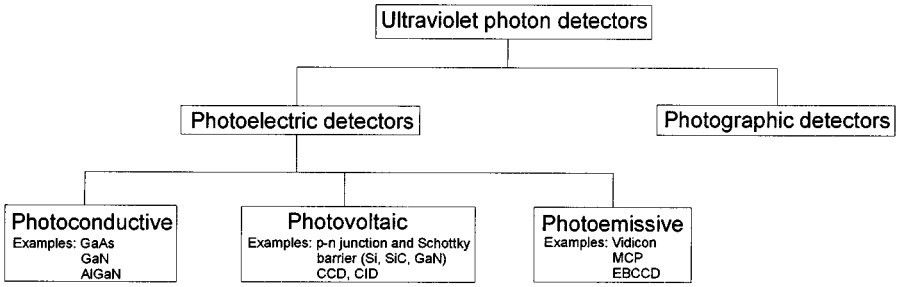

FIG. 1. Classification of ultraviolet photon detectors.

light sources,[3] and spectroscopy.[4] The historical development of spectroscopy is traced in the introductory chapter in Samson's book,[1] also the chapter in Green's book by Hennes and Dunkleman,[5] entitled *Ultraviolet Technology*, is an available source for the development of experimental techniques of that time. Recently, Huffman has published two books about the ultraviolet spectral regions.[6,7] The second of them[7] supplements previously published books, since this volume is a collection of reprints that present the milestone articles in ultraviolet optics and technology.

The issue of UV detectors is treated in several monographs and reviews. An extensive examination of various detector systems for both imaging and nonimaging applications is presented by Carruthers.[8] Timothy and Madden[9] have restricted their review to photon detectors that are currently available for use at ultraviolet and x-ray wavelengths. More information about the history of the development of UV detectors and their current status in astronomy can be found in an excellent book entitled *Low light level detectors in astronomy* by Eccles, Sim, and Tritton.[10] Another of Timothy's review articles is devoted mainly to detectors for optical wavelengths,[11] and a comparison of charge coupled devices (CCDs) to other optical detectors is given by Janesick *et al.*[12] The reviews of the present and future technological concepts currently being considered in astrophysics and astronomy are given by Welsh and Kaplan,[13] Joseph,[14] and by Ulmer *et al.*[15] However, the UV detectors have also found terrestrial applications. They can detect UV emissions from flames in the presence of hot backgrounds (such as infrared emission from the hot bricks in a furnace). This provides an excellent flame on/off determination system for controlling the gas supply to large furnaces and boiler systems. Flame safeguard and fire control areas are just two of the various possible applications for the UV detectors.

In this article we will first present the classification of UV detectors and general requirements imposed on these detectors. Further consideration will be restricted to modern semiconductor UV detectors, so the basic theory of photoconductive and photovoltaic detectors will be presented in a uniform way convenient for various detector materials. Next, the current state of the art of different types of semiconductor UV detectors will be presented. The main effort will be especially directed to a new generation of UV detectors. This generation of detectors is the product of five years of materials and device research, which resulted in the development of high quality GaN layers.

II. CLASSIFICATION OF ULTRAVIOLET DETECTORS

In general, UV detectors fall into two categories: photon detectors (also named photodetectors) and thermal detectors. In photon detectors the incident photons are absorbed within the material by interaction with electrons. The observed electrical signal results from the changed electronic energy distribution. The photon detectors measure the rate of arrival of quanta and show a selective wavelength dependence of the response per unit incident radiation power. In thermal detectors, the incident radiation is absorbed and raises the temperature of the material. The output signal is observed as a change in some temperature-dependent property of the material. In pyroelectric detectors a change in the internal electrical polarization is measured, whereas in the case of bolometers a change in the electrical resistance is measured. The thermal effects are generally wavelength independent since the radiation can be absorbed in a ''black'' surface coating. Because of greater sensitivity, photon detectors are more commonly utilized at UV wavelengths. Thermal detectors, however, are sometimes employed at UV wavelengths as absolute radiometric standards.

UV photon detectors (see Fig. 1) have traditionally been devoted into two distinct classes, namely, photographic and photoelectric. Photographic emulsion has the great advantage of an image-storing capability and can thus record a large amount of data in a single exposure. However, photographic emulsion has a number of limitations: sensitivity is considerably lower than that of a photoelectric detector, the dynamic range is limited, the response is not a linear function of the incident photon flux at a specific wavelength, and emulsion is sensitive to a very wide energy range (accordingly the elimination of background fog levels induced by scattered light and by high-energy charged particles is extremely difficult).

Photoelectric detectors, on the other hand, are more sensitive, have a greater stability of response and provide better linearity characteristics. In the last decade considerable progress in the image-recording capability of photoelectronic devices has been observed. Recently developed photovoltaic array detectors [such as the charge coupled devices] and photoemissive array detectors [such as the microchannel array plates (MCPs)] for the first time combine the sensitivity and radiometric stability of a photomultiplier with a high-resolution imaging capability.

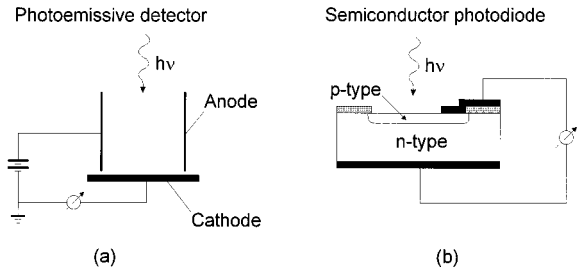

FIG. 2. Principle operation of photoemissive (a) and semiconductor detectors (b).

In the most commonly employed photoemissive UV detectors, the photon is allowed to impact a solid surface realizing a photoelectron into the vacuum environment [Fig. 2(a)]. Applying a voltage between the photocathode surface and a positively biased anode causes a photoelectron current to flow in proportion to the intensity of the incident radiation. Since these detectors make use of the external photoelectric effect, the wavelength range of sensitivity is defined primarily by the work function of the surface material.

In the semiconductor detectors, the photons are absorbed in the bulk of the semiconductor material producing electron-hole pairs which are separated by an electrical field. These detectors make use of the internal photoelectric effect where the energy of the photons is large enough to raise the electrons into the conduction band of the semiconductor material. In the case of photovoltaic detectors, the electron-hole pairs are separated by the electrical field of p-n junctions, Schottky barrier, or metal-insulator-semiconductor (MIS) capacitors, which leads to an external photocurrent proportional to the number of detected photons [Fig. 2(b)]. Applying a voltage across the absorbing region causes a current to flow in proportion to the intensity of the incident radiation.

In the photoemissive detectors, the primary photoelectron can be multiplied by the process of secondary emission to produce a large cloud of electrons. The occurrence of a single photoelectron event then can be detected either directly with conventional electronic circuits or by accelerating the electron cloud to high energy and allowing it to impact a phosphor screen. The emitted pulse of visible-light photons can then be viewed directly, or detected and recorded by additional photosensitive systems. Detectors operated in this pulse-counting mode can provide the ultimate level of sensitivity set by the quantum efficiency of the photocathode.

There are a number of important differences between the two classes of detectors. In the photoemissive detectors, the primary photoelectron produced by the photocathode can be multiplied by the process of secondary emission to produce a large cloud of electrons. The degree of multiplication is called the gain of the detector. If the gain is sufficiently large, the electron cloud generated by a single photoelectron can be detected directly with conventional electronic circuits. Alternatively, the electron cloud can be accelerated to high energy and allowed to impact a phosphor screen. The resulting pulse of visible-light photons emitted from the phosphor can be viewed directly or can be detected and recorded by additional photosensitive systems. Detectors operated in this pulse-counting mode can provide the ultimate level of sensitivity at very low signal level. That form of intensification implies, however, high voltages and the inherent associated difficulties. Moreover, it is not possible in this mode of operation to store the detected events within the detector, and the detected signal must be integrated in a separate recording system. Table I compares these two types of UV detectors.

The importance of UV semiconductor detectors has resulted in the recent meteoric expansion of the semiconductor industry, and second, the continuing emphasis on the development of low-light-level imaging systems for military and civilian surveillance applications. These detectors should:

(1) not be sensitive to light at optical wavelengths (commonly referred to as being solar blind),
(2) have high quantum efficiency,
(3) have a high dynamic range of operation,
(4) have low backgrounds since noise arising from the background often dominates in faint UV observations.

Multiplying the number of primary charge carriers is generally not possible in semiconductor detectors (although this deficiency may be offset by the very high internal quantum efficiency of the semiconductor material). These detectors are thus less sensitive at the lowest signal levels than the photoemissive detectors operating in pulse-counting mode. However, the semiconductor detectors have the ability to store charge and integrate the detected signal for significant periods of time. Recently, there has been much development of CCD detectors for use in the UV spectral ranges.[7,8,12,16–18] On the contrary, for visible spectral range devices the use of Si CCDs in the UV region is not yet well established because of the many problems connected with the interaction of UV radiation with the materials typically used in silicon technol-

TABLE I. Comparison of photoemissive and semiconductor UV detectors.

Type	Advantages	Disadvantages
Photoemissive detectors	Easy to operate	Low quantum efficiency
	High sensitivity	Strong spectral dependence of responsivity
	Solar blind	Sensitiveness to surface contaminations
Semiconductor detectors	Broad spectral responsivity	Induced aging effects
	Excellent linearity	
	High quantum efficiency	
	High dynamic range of operation	
	Large-format image arrays	

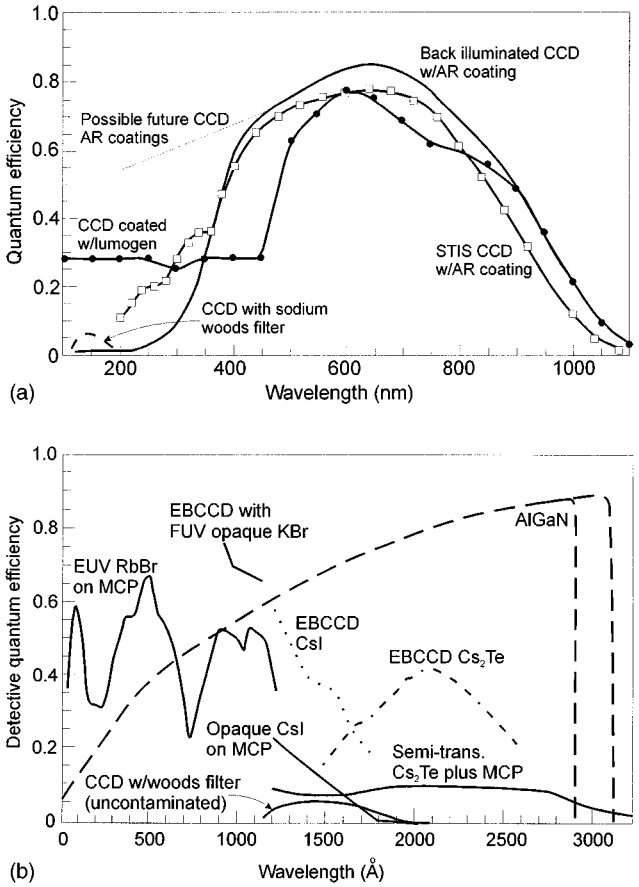

FIG. 3. Quantum efficiency of thinned backside illuminated CCDs (a) and solar-blind efficiencies of various UV detectors (b). The detective quantum efficiency (DQE) of a complete detector system takes into account any loss of detected photons and the quantum efficiency of each stage of the system. The DQE can be expressed in terms of the signal-to-noise characteristics of the input and output signals as the ratio $\mathrm{DQE}=(S/N_{\mathrm{out}})^2/(S/N_{\mathrm{in}})^2$ (after Ref. 14).

ogy. For example, the relatively thin gate oxide layer (500–1200 Å) on the CCD front face is strongly absorbing of UV radiation, so that it is not possible to use front-illuminated CCDs for direct detection of this radiation. The electron-hole pairs created in this layer are not separated by an internal field and will therefore not contribute to the photocurrent. Thinned, back-illuminated CCDs also have some problems. In fact, after the device is thinned, a native back-oxide layer forms naturally, and even if it is very thin, typically less than 50 Å, this dramatically influences overall sensor performance. A number of solutions have been tried, ranging from the deposition of a scintillator, such as coronene[19] or lumigen,[20] to the backside illumination of thinned devices, so to avoid the absorption of radiation by the thick polysilicon gate structure. Some methods have been developed to reduce the surface state problems using ''back-accumulation'' techniques.[21] They are based on the hypothesis that the back surface potential can be pinned by heavily populating it with holes which create an electric field that directs the photogenerated charges away from the back surface. They can be divided into three categories: backside charging, flash gate techniques, and ion implantation.[8,21]

A semiconductor array can also be used to directly detect the photoelectron released from a photocathode. The photoelectron is accelerated to very high energy by an electrostatic field and allowed to bombard the semiconductor material. If sufficient energy is released within the absorbing region, enough electron-hole pairs can be produced to provide a measurable signal from a single photoelectron impact.

Figure 3 shows the current status of the quantum efficiency of common detectors. The top plot in Fig. 3 shows the quantum efficiencies that can be obtained with various configurations of thinned, back-illuminated CCDs. Future antireflection coatings, depicted as a dot-dash line, may extend the range well into the UV range. Figure 3(b) shows the solar-blind efficiencies obtained for various UV detectors.

III. ULTRAVIOLET PHOTODETECTORS

Ultraviolet semiconductor photodetectors work in three fundamental modes:

(1) photoconductive detectors,
(2) photodiode p-n junctions, and
(3) Schottky barrier detectors.

Below, after describing the general theory of photodetectors, the basic theories of photoconductors, p-n junctions, and Schottky barriers are presented. In the last part of this section, a short presentation of semiconductor materials used for the fabrication of UV detectors is included.

A. General theory of photodetectors

The photodetector is a slab of homogeneous semiconductor with the actual ''electrical'' area A_e which is coupled to a beam of infrared radiation by its optical area A_o. Usually, the optical and electrical areas of the device are the same or close. The use of optical concentrators can increase the A_o/A_e ratio.

The current responsivity of the photodetector is determined by the quantum efficiency η and by the photoelectric gain g. The quantum efficiency value describes how well the detector is coupled to the radiation to be detected. It is usually defined as the number of electron-hole pairs generated per incident photon. The idea of photoconductive gain g was put forth by Rose[22] as a simplifying concept for the understanding of photoconductive phenomena and is now widely used in the field. The photoelectric gain is the number of carriers passing contacts per one generated pair. This value shows how well the generated electron-hole pairs are used to generate the current response of a photodetector. Both values are assumed here as constant over the volume of the device.

The spectral current responsivity is equal to

$$R_i=\frac{\lambda\eta}{hc}qg, \tag{1}$$

where λ is the wavelength, h is Planck's constant, c is the light velocity, q is the electron charge, and g is the photoelectric current gain. Assuming that the current gains for photocurrent and noise current are the same, the current noise due to generation and recombination processes is[22]

$$I_n^2=2(G+R)A_e t\Delta f q^2 g^2, \tag{2}$$

where G and R are the generation and recombination rates, Δf is the frequency band, and t is the thickness of the detector.

Detectivity D^* is the main parameter characterizing normalized signal-to-noise performance of detectors and can be defined as

$$D^* = \frac{R_i (A_o \Delta f)^{1/2}}{I_n}. \tag{3}$$

According to Eqs. (1)–(3)[23]

$$D^* = \frac{\lambda}{hc}\left(\frac{A_o}{A_e}\right)^{1/2} \eta [2(G+R)t]^{-1/2}. \tag{4}$$

For a given wavelength and operating temperature, the highest performance can be obtained by maximizing $\eta/[t(G+R)]^{1/2}$ which corresponds to the condition of the highest ratio of the sheet optical generation to the square root of sheet thermal generation–recombination.

The effects of a fluctuating recombination can frequently be avoided by arranging for the recombination process to take place in a region of the device where it has little effect due to low photoelectric gain: for example, at the contacts in sweep-out photoconductors or in the neutral regions of diodes. In this case, the noise can be reduced by a factor of 2.5 and detectivity increased by the same factor. The generation process with its associated fluctuation, however, cannot be avoided by any means.

At equilibrium the generation and recombination rates are equal, and assuming that $A_o = A_e$ we have

$$D^* = \frac{\lambda}{2hc}\frac{\eta}{t^{1/2}} G^{-1/2}. \tag{5}$$

The total generation rate is a sum of the optical and thermal generation

$$G = G_{\text{th}} + G_{\text{op}}. \tag{6}$$

The optical generation may be due to the signal or thermal background radiation. For infrared detectors, usually thermal background radiation is higher compared to the signal radiation. If the thermal generation is reduced much below the background level, the performance of the device is determined by the background radiation [conditions for background limited infrared photodetector (BLIP)]. The noise equivalent power (NEP) in this approximation is given by[24,25]

$$\text{NEP} = \frac{(A\Delta f)^{1/2}}{D^*} = h\gamma\left(\frac{2A\Phi_B \Delta f}{\eta}\right)^{1/2}, \tag{7}$$

where Φ_B is the total background photon flux density reaching the detector, and Δf is the electrical bandwidth of the receiver. The background photon flux density received by the detector depends on its angular view of the background and on its ability to respond to the wavelengths contained in this source.

When photodetectors are operated in conditions where the background flux is less than the optical (signal) flux, the ultimate performance of detectors is determined by the signal fluctuation limit (SFL). It is achieved in practice with photomultipliers operating in the visible and ultraviolet region, but it is rarely achieved with solid-state devices, which are normally detector-noise or electronic-noise limited. The (NEP) and detectivity of detectors operating in this limit have been derived by a number of authors (see, e.g., Kruse *et al.*[24,25]).

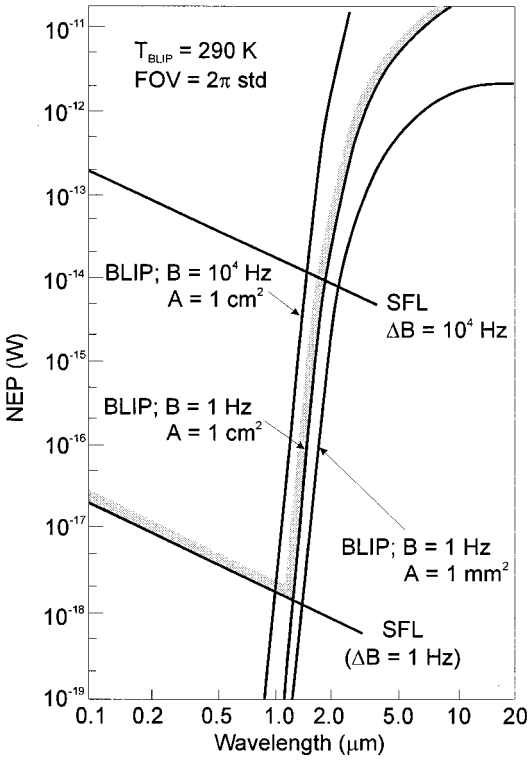

FIG. 4. Minimum detectable monochromatic power as a function of wavelength for composite of SFL and BLIP limit for two detector areas and electrical bandwidths. Background temperature is 290 K and FOV is 2π steradiants. Detector long wavelength limit is equal to source wavelength (after Ref. 25).

The NEP in the SFL is given by

$$\text{NEP} = \frac{2hc\Delta f}{\eta\lambda} \tag{8}$$

when Poisson statistics are applicable. This threshold value implies a low number of photons per observation interval. A more meaningful parameter is the probability that a photon will be detected during an observation period. Kruse[25] shows that the minimum signal power to achieve 99% probability that a photon will be detected in an observation period t_o is

$$\text{NEP}_{\min} = \frac{9.22hc\Delta f}{\eta\lambda}, \tag{9}$$

where Δf is assumed to be $1/2t_o$. Note that the detector area does not enter into the expression and that $\text{NEP}_{\min}$ depends linearly upon the bandwidth, which differs from the case in which the detection limit is set by internal or background noise.

Seib and Aukerman[26] also have derived an expression for the SFL identical to Eq. (9) except that the multiplicative constant is not 9.22 but $2^{3/2}$ for an ideal photoemissive or photovoltaic detector and $2^{5/2}$ for a photoconductor. This difference in the constant arises from the differing assumptions as to the manner in which the detector is employed and the minimum detectable signal-to-noise ratio.

It is interesting to determine the composite signal fluctuation and background fluctuation limits. Figure 4 illustrates the spectral NEP over the wavelength range from 0.1 to 20 μm assuming a background temperature of 290 K detector areas of 1 cm^2 and 1 mm^2 (applicable only to the background fluctuation limit), a 2π steradian field of view (FOV) [applicable only to the background fluctuation limit], and bandwidths of 1 and 10^4 Hz. These additional values of parameters are specified because of different dependencies of NEP (upon area and bandwidth) for signal fluctuation and background fluctuation limits. Note that the intersections of three pairs of curves, for which the bandwidths of the signal and background fluctuation limits are equal, lie between 1.0 and 1.5 μm. To illustrate the composite, a detector with an area of 1 cm^2 (applicable to the background fluctuation limit) and a bandwidth of 1 Hz has been scored. For this pair, at wavelengths below 1.2 μm the SFL dominates; the converse is true above 1.2 μm. The minimum detectable monochromatic radiant power at 1.2 μm is 1.5×10^{-18} W in a 1 Hz bandwidth. Below 1.2 μm the wavelength dependence is small. Above 1.2 μm it is very large, due to steep dependence upon wavelength of the short wavelength end of the 290 K background spectral distribution.

The basic equations for dc analysis of detector performance are well known: two current-density equations for electrons I_e and holes J_b two continuity equations for electrons and holes, and Poisson's equation which are collectively referred to as the Van Roosbroeck model[27]

$$J_e = qD_e \frac{dn}{dx} - q\mu_e n \frac{d\Psi}{dx} \quad \text{current density for electrons,} \tag{10}$$

$$J_h = qD_h \frac{dp}{dx} - q\mu_h p \frac{d\Psi}{dx} \quad \text{current density for holes,} \tag{11}$$

$$\frac{1}{q}\frac{dJ_e}{dx} + (G-R) = 0 \quad \text{continuity equation for electrons,} \tag{12}$$

$$\frac{1}{q}\frac{dJ_h}{dx} - (G-R) = 0 \quad \text{continuity equation for holes,} \tag{13}$$

$$\frac{d^2\Psi}{dx^2} = -\frac{q}{\varepsilon_0\varepsilon_r}(N_d - N_a + p - n), \quad \text{Poisson's equation,} \tag{14}$$

where Ψ is the electrostatic potential, N_d is the concentration of donors, N_a is the concentration of acceptors, D_e and D_h are the electron and hole diffusion coefficients, n and p are the electron and hole densities, and $\varepsilon_0\varepsilon_r$ is the permittivity of the semiconductor. A self-consistent iterative procedure for the solution of this mathematical model is well documented in the literature.[28] The method reformulates the model in terms of integral equations which incorporate the boundary conditions and eliminate J_e and J_h as intermediate variables. This allows the carrier densities to be computed from the potential distribution.

The generation–recombination term $(G+R)$ is associated with the predominant recombination mechanisms. There are three important generation and recombination mechanisms: Shockley–Read, radiative, and Auger mechanisms. The Shockley–Read mechanism occurs via lattice defect and impurity energy levels within the forbidden energy gap and is the dominant mechanism in wide band-gap materials.

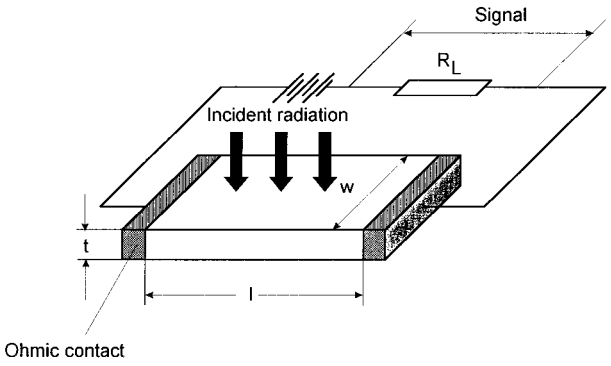

FIG. 5. Geometry and bias of a photoconductor.

B. Photoconductive detectors

The photoconductive detector (also named as the photoconductor) is essentially a radiation-sensitive resistor. The operation of a photoconductor is shown in Fig. 5. A photon of energy $h\nu$ greater than the band-gap energy E_g is absorbed to produce an electron-hole pair, thereby changing the electrical conductivity of the semiconductor.

In almost all cases the change in conductivity is measured by means of electrodes attached to the sample. For low resistance material, the photoconductor is usually operated in a constant current circuit as shown in Fig. 5. The series load resistance is large compared to the sample resistance, and the signal is detected as a change in voltage developed across the sample. For high resistance photoconductors, a constant voltage circuit is preferred and the signal is detected as a change in current in the bias circuit.

1. Current and voltage responsivity

We assume that the signal photon flux density $\Phi_s(\lambda)$ is incident on the detector area $A = wl$ and that the detector is operated under constant current conditions, i.e., $R_L \gg R$. We suppose further that the illumination and the bias field are weak, and the excess carrier lifetime, τ, is the same for majority and minority carriers. To derive an expression for voltage responsivity, we take a one-dimensional approach for simplicity. This is justified for a detector thickness, t, that is small with respect to the minority carrier diffusion length. We also neglect the effect of recombination at frontal and rear surfaces.

The basic expression describing photoconductivity in semiconductors under equilibrium excitation (i.e., steady state) is

$$I_{\text{ph}} = q\eta A\Phi_s g, \tag{15}$$

where I_{ph} is the short circuit photocurrent at zero frequency (dc), i.e., the increase in current above the dark current accompanying irradiation. The photoconductive gain is deter-

mined by the properties of the detector, i.e., by which detection effect is used and the material and configuration of the detector.

In general, photoconductivity is a two-carrier phenomenon and the total photocurrent of electrons and holes is

$$I_{\rm ph}=\frac{wtq(\Delta n\mu_e+\Delta p\mu_h)V_b}{l}, \tag{16}$$

where μ_e is the electron mobility, μ_h is the hole mobility, V_b is the bias voltage and

$$n=n_0+\Delta n, \quad p=p_0+\Delta p. \tag{17}$$

The terms n_0 and p_0 are the average thermal equilibrium carrier densities, and Δn and Δp are the excess carrier concentrations.

Taking the conductivity to be dominated by electrons (in all known high sensitivity photoconductors this is found to be the case) and assuming uniform and complete absorption of the light in the detector, the rate equation for the excess electron concentration in the sample is[29]

$$\frac{d\Delta n}{dt}=\frac{\Phi_s\eta}{t}-\frac{\Delta n}{\tau}, \tag{18}$$

where τ is the excess carrier lifetime. In the steady condition, the excess carrier lifetime is given by the equation

$$\tau=\frac{\Delta nt}{\eta\Phi_s}. \tag{19}$$

Equating (15) to (16) gives

$$g=\frac{tV_h\mu_e\Delta n}{l\,\eta\Phi_s} \tag{20}$$

and invoking Eq. (19) we get for the photoconductive gain

$$g=\frac{\tau\mu_eV_b}{l^2}=\frac{\tau}{l^2/\mu_eV_b}. \tag{21}$$

So, the photoconductive gain can be defined as

$$g=\frac{\tau}{t_t}, \tag{22}$$

where t_t is the transit time of electrons between ohmic contacts. This means that the photoconductive gain is given by the ratio of free carrier lifetime, τ, to transit time, t_t between the sample electrodes. The photoconductive gain can be less than or greater than unity depending upon whether the drift length, $L_d=v_d\tau$, is less than or greater than interelectrode spacing, 1. The value of $L_d>1$ implies that a free charge carrier swept out at one electrode is immediately replaced by injection of an equivalent free charge carrier at the opposite electrode. Thus, a free charge carrier will continue to circulate until recombination takes place.

When $R_L\gg R$, a signal voltage across the load resistor is essentially the open circuit voltage

$$V_s=I_{\rm ph}R_d=I_{\rm ph}\frac{l}{qwtn\mu_e}, \tag{23}$$

where R_d is the detector resistance. Assuming that the change in conductivity upon irradiation is small compared to the dark conductivity, the voltage responsivity is expressed as

$$R_v=\frac{V_s}{P_\lambda}=\frac{\eta}{Iwt}\frac{\lambda\tau}{hc}\frac{V_b}{n_0}, \tag{24}$$

where the absorbed monochromatic power $P_\lambda=\Phi_sAh\nu$.

This expression shows clearly the basic requirements for high photoconductive responsivity at a given wavelength λ: one must have high quantum efficiency η, long excess carrier lifetime τ, the smallest possible piece of crystal, low thermal equilibrium carrier concentrations n_0, and the highest possible bias voltage V_b.

The frequency dependent responsivity can be determined by the equation

$$R_v=\frac{\eta}{lwt}\frac{\lambda\tau_{\rm ef}}{hc}\frac{V_b}{n_0}\frac{l}{(l+\omega^2\tau_{\rm ef}^2)^{1/2}}, \tag{25}$$

where $\tau_{\rm el}$ is the effective carrier lifetime. Usually, the photoconductive detectors fabricated from wide band-gap materials reveal strongly sub-linear responses and excitation-dependent response time is observed even at relatively low excitation levels. This can be attributed to the redistribution of the charge carriers with increased excitation level.

The above simple model takes no account of additional limitations related to the practical conditions of photoconductor operation such as sweep-out effects or surface recombination. These are specified below.

2. Sweep-out effects

Equation (25) shows that voltage responsivity increases monotonically with the increase of bias voltage. However, there are two limits on applied bias voltage, namely: thermal conditions (joule heating of the detector element) and sweep out of minority carriers. The thermal conductance of the detector depends on the device fabrication procedure. If the excess carrier lifetime is long, we cannot ignore the effects of contacts and of drift and diffusion on the device performance. Present-day material technology is such that at moderate bias fields minority carriers can drift to the ohmic contacts in a short time compared to the recombination time in the material. Removal of carriers at an ohmic contact in this way is referred to as ''sweep out.''[30,31] Minority carrier sweep out limits the maximum applied voltage of V_b. The effective carrier lifetime can be reduced considerably in detectors where the minority carrier diffusion length exceeds the detector length (even at very low bias voltages). At low bias the average drift length of the minority carriers is very much less than the detector length, I, and the minority carrier lifetime is determined by the bulk recombination modified by diffusion to surface and contacts. The carrier densities are uniform along the length of the detector. At higher values of the applied field, the drift length of the minority carriers is comparable to or greater than 1. Some of the excess minority carriers are lost at an electrode, and to maintain space-charge equilibrium, a drop in excess majority carrier density is necessary. This way the majority carrier lifetime is reduced. It should be pointed out that the loss of the majority carriers at one ohmic contact is replenished by injection at the other, but the minority carriers are not replaced. At high bias the excess carrier density is nonuniformly distributed along the length of the sample.

To achieve high photoelectric gain, low resistance and low surface recombination velocity contacts are required. The metallic contacts are usually far from expectation. The contacts are characterized by a recombination velocity which can be varied from infinity (ohmic contacts) to zero (perfectly blocking contacts). In the latter case, a more intensely doped region at the contact (e.g., n^+ for n-type devices or heterojunction contact) causes a built-in electric field that repels minority carriers, thereby reducing recombination and increasing the effective lifetime and the responsivity. Practical realization of the device would require double epitaxial growth and the subsequent removal of the heavy doped material from the active area of the device.

3. Noise mechanisms in photoconductors

All detectors are limited in the minimum radiant power which they can detect by some form of noise which may arise in the detector itself, in the radiant energy to which the detector responds, or in the electronic system following the detector. Careful electronic design, including low noise amplification, can reduce the system noise below that in the output of the detector. This topic will not be treated here.

We can distinguish two groups of noise; the radiation noise and the noise internal to the detector. The radiation noise includes signal fluctuation noise and background fluctuation noise. Under most operating conditions the signal fluctuation limit is operative for ultraviolet and visible detectors.

The random processes occurring in semiconductors give rise to internal noise in detectors even in the absence of illumination. There are two fundamental processes responsible for the noise: fluctuations in the velocities of free carriers due to their random thermal motion, and fluctuations in the densities of free carriers due to randomness in the rates of thermal generation and recombination.[32]

Johnson–Nyquist noise is associated with the finite resistance R of the device. This type of noise is due to the random thermal motion of charge carriers in the crystal and not due to fluctuations in the total number of these charge carriers. It occurs in the absence of external bias as a fluctuating voltage or current depending upon the method of measurement. Small changes in the voltage or current at the terminals of the device are due to the random arrival of charge at the terminals. The root mean square of the Johnson–Nyquist noise voltage in the bandwidth Δf is given by

$$V_j=(4kTR\Delta f)^{1/2}, \tag{26}$$

where k is the Boltzmann constant and T is the temperature. This type of noise has a ''white'' frequency distribution.

At finite bias currents, the carrier density fluctuations cause resistance variations, which are observed as noise exceeding Johnson–Nyquist noise. This type of excess noise in photoconductive detectors is referred to as generation–recombination (g–r) noise. G–r noise is due to the random generation of free charge carriers by the crystal vibrations and their subsequent random recombination. Because of the randomness of the generation and recombination processes, it is unlikely that there will be exactly the same number of charge carriers in the free state at succeeding instances of time. This leads to conductivity changes that will be reflected as fluctuations in current flow through the crystal. Many forms of g–r noise expression exist, depending upon the internal properties of the semiconductors.

The rms g–r noise current for an extrinsic n-type photoconductor with carrier lifetime τ can be written[32]

$$I_{\mathrm{g-r}}^2=\frac{4I^2\overline{\Delta N^2}\tau\Delta f}{N^2(1+\omega^2\tau^2)}, \tag{27}$$

where N is the number of carriers in the detector. Usually, in an extrinsic semiconductor there will be some counterdoping, i.e., electrons trapped at deep lying levels. If the number of deep traps is small compared to the number of electrons (electrons being the majority carriers), then the variance ΔN^2 is equal to N[32]. The current flowing in the device is $I=Nqg/\tau$, hence

$$I_{\mathrm{g-r}}^2=\frac{4qIg\Delta f}{1+\omega^2\tau^2}. \tag{28}$$

Generation–recombination noise usually dominates the noise spectrum of photoconductors at intermediate frequencies.

An additional type of noise, referred to as $1/f$ noise, because it exhibits an approximately $1/f$ power law spectrum, is always observed. It is less understood than the more fundamental noise sources and is not generally amenable to mathematical analysis. The general expression for the $1/f$ noise current is

$$I_{1/f}=\left(\frac{KI_b^\alpha\Delta f}{f^\beta}\right)^{1/2}, \tag{29}$$

where K is a proportionality factor, I_b is the bias current, α is a constant whose value is about 2, and β is a constant whose value is about unity.

In general, $1/f$ noise appears to be associated with the presence of potential barriers at the contacts, surface trapping phenomena, and surface leakage currents. Reduction of $1/f$ noise to an acceptable level is an art which depends greatly on the processes employed in preparing the contacts and surfaces. Up until now, no fully satisfactory general theory has been formulated. The two most current models for the explanation of $1/f$ noise were considered: Hooge's model,[33] which assumes fluctuations in the mobility of free charge carriers, and McWhortel's model,[32] based on the idea that the free carrier density fluctuates.

The UV semiconductor detectors usually exhibit $1/f$ noise at low frequency. At higher frequencies the amplitude drops below that of one of the other types of noise.

4. Quantum efficiency

In most photoconductor materials the internal quantum efficiency η_0 is nearly unity; that is, almost all photons absorbed contribute to the photoconductive phenomenon. For a detector, as a slab of material, shown in Fig. 5, with surface reflection coefficients r_1 and r_2 (on the top and bottom sur-

faces, respectively), and absorption coefficient α, the internal photogenerated charge profile in the y direction is[34]

$$S(y)=\frac{\eta_0(1-r_1)\alpha}{1-r_1r_2\ \exp(-2\alpha t)}\ [\exp(-\alpha y)$$

$$+r_2\ \exp(-2\alpha t)\exp(-\alpha y)]. \tag{30}$$

The external quantum efficiency is simply the integral of this function over the detector thickness

$$\eta=\int_0^t S(y)dy$$

$$=\frac{\eta_0(1-r_1)[1+r_2\ \exp(-\alpha t)][1-\exp(\alpha t)]}{1-r_1r_2\ \exp(-2\alpha t)}. \tag{31}$$

When r_1 and $r_2=r$, the quantum efficiency is reduced to

$$\eta=\frac{\eta_0(1-r)[1-\exp(\alpha t)]}{1-r\ \exp(-\alpha t)}. \tag{32}$$

Intrinsic detector materials tend to be highly absorptive; so in a practical well-designed detector assembly only the top surface reflection term is significant, and then

$$\eta\approx\eta_0(1-r)\approx 1-r. \tag{33}$$

By anti-reflection coating the front surface of the detector, this quantity can be made greater than 0.9.

5. Influence of surface recombination

The photoconductive lifetime in general provides a lower limit to the bulk lifetime, due to the possibility of enhanced recombination at the surface. Surface recombination reduces the total number of steady-state excess carriers by reducing the recombination time. It can be shown that τ_{ef} is related to the bulk lifetime by the expression[35]

$$\frac{\tau_{\text{ef}}}{\tau}=\frac{A_1}{\alpha^2L_D^2-1}, \tag{34}$$

where

$$A_1=L_D\alpha\left[\frac{(\alpha D_D+s_1)\{s_2[\text{ch}(t/L_D)-1]+(D_D/L_D)\text{sh}(t/L_D)\}}{(D_D/L_D)(s_1+s_2)\text{ch}(t/L_D)+(D_D^2/L_D^2+s_1s_2)\text{sh}(t/L_D)}\right.$$

$$\left.\times\frac{(\alpha D_D-s_2)\{s_1[\text{ch}(t/L_D)-1]+(D_D/L_D)\text{sh}(t/L_D)\}e^{\alpha t}}{(D_D/L_D)(s_1+s_2)\text{ch}(t/L_D)+(D_D^2/L_D^2+s_1s_2)\text{sh}(t/L_D)}-(1-e^{-\alpha t})\right]$$

and

$$D_D=\frac{D_ep_0\mu_h+D_hn_0\mu_e}{n_0\mu_e+p_0\mu_h}$$

is the ambipolar diffusion coefficient, s_1 and s_2 are the surface recombination velocities at the front and back surfaces of the photoconductor, and $L_D=(D_D\tau)^{1/2}$. Other marks have their usual meanings, $D_{e,h}=(kT/q)\mu_{e,h}$ are the respective carrier diffusion coefficients for electrons and holes.

If the absorption coefficient α is large $e^{-\alpha t}\approx 0$ and $s_1\ll\alpha D_D$, Eq. (34) is simplified to the well-known expression[30]

$$\frac{\tau_{\text{ef}}}{\tau}=\frac{D_D}{L_D}\frac{s_2[\text{ch}(t/L_D)-1]+(D_D/L_D)\text{sh}(t/L_D)}{L_D(D_D/L_D)(s_1+s_2)\text{ch}(t/L_D)+(D_D^2/L_D^2+s_1+s_2)\text{sh}(t/L_D)}. \tag{35}$$

Further simplification for $s_1=s_2=s$ leads to

$$\frac{1}{\tau_{\text{ef}}}=\frac{1}{\tau}+\frac{2s}{t}. \tag{36}$$

C. p-n junction photodiodes

Photoeffects which occur in structures with built-in potential barriers are essentially photovoltaic and result when excess carriers are injected optically into the vicinity of such barriers. The role of the built-in electric field is to cause the charge carriers of opposite sign to move in opposite directions depending upon the external circuit. Several structures are possible to observe the photovoltaic effect. These include p-n junctions, heterojunctions, Schottky barriers, and metal-insulator-semiconductor (MIS) photocapacitors. Each of these different types of devices has certain advantages for UV detection, depending on the particular applications.

The most common example of a photovoltaic detector is the abrupt p-n junction prepared in the semiconductor, which is often referred to simply as a photodiode. The operation of the p-n junction photodiode is illustrated in Fig. 6. Photons with energy greater than the energy gap, incident on the front surface of the device, create electron-hole pairs in the material on both sides of the junction. By diffusion, the electrons and holes generated within a diffusion length from the junction reach the space-charge region. Then electron-hole pairs are separated by the strong electric field; minority carriers are readily accelerated to become majority carriers

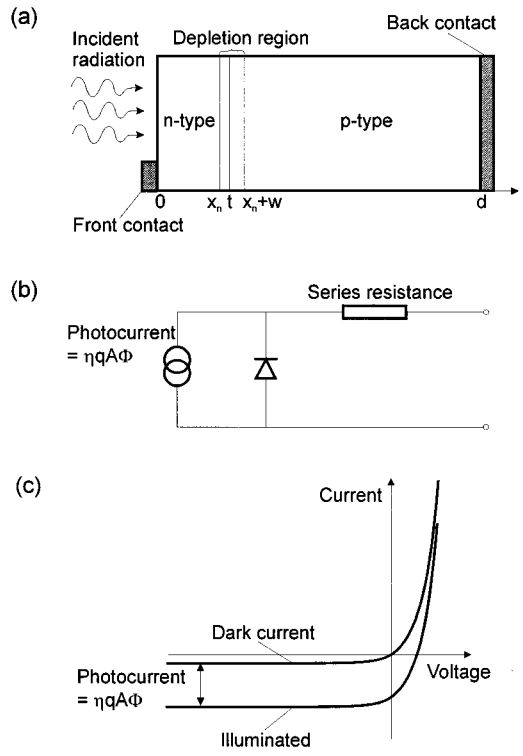

FIG. 6. Schematic representation of the operation of a p-n junction photodiode: (a) geometrical model of the structure, (b) equivalent circuit of an illuminated photodiode (the series resistance includes the contact resistance as well as the bulk p- and n-regions), (c) current–voltage characteristics for the illuminated and nonilluminated photodiode.

on the other side. This way a photocurrent is generated which shifts the current–voltage characteristic in the direction of negative or reverse current, as shown in Fig. 6(c). The equivalent circuit of a photodiode is shown in Fig. 6(b).

The total current density in the p-n junction is usually written as

$$J(V,\Phi)=J_d(V)-J_{\rm ph}(\Phi), \tag{37}$$

where the dark current density, J_d, depends only on V and the photocurrent depends only on the photon flux density Φ.

Generally, the current gain in a simple photovoltaic detector (e.g., not an avalanche photodiode) is equal to 1, and then, according to Eq. (14), the magnitude of photocurrent is equal

$$I_{\rm ph}=\eta qA\Phi. \tag{38}$$

The dark current and photocurrent are linearly independent (which occurs even when these currents are significant) and the quantum efficiency can be calculated in a straightforward manner.[36]

If the p-n diode is open circuited, the accumulation of electrons and holes on the two sides of the junction produces an open-circuit voltage [Fig. 6(c)]. If a load is connected to the diode, a current will conduct in the circuit. The maximum current is realized when an electrical short is placed across the diode terminals, and this is called the short-circuit current.

The open-circuit voltage can be obtained by multiplying the short-circuit current by the incremental diode resistance $R=(\partial I/\partial V)^{-1}$ at $V=V_b$:

$$V_{\rm ph}=\eta qA\Phi R, \tag{39}$$

where V_b is the bias voltage and $I=f(V)$ is the current–voltage characteristic of the diode.

In many direct applications the photodiode is operated at zero-bias voltage

$$R_0=\left(\frac{\partial I}{\partial V}\right)^{-1}_{|V_s=0}. \tag{40}$$

A frequently encountered figure of merit for a photodiode is the R_0A product

$$R_0A=\left(\frac{\partial J}{\partial V}\right)^{-1}_{|V_s=0}, \tag{41}$$

where $J=1/A$ is the current density.

In the detection of radiation, the photodiode is operated at any point of the $I-V$ characteristic. Reverse bias operation is usually used for very high frequency applications to reduce the RC time constant of the devices.

1. Ideal diffusion-limited p-n junctions

a. Diffusion current. Diffusion current is the fundamental current mechanism in a p-n junction photodiode. Figure 6(a) shows a one-dimensional photodiode model with an abrupt junction where the spatial charge of width w surrounds the metalographic junction boundary $x=t$, and two quasineutral regions $(0,x_n)$ and $(x_n+w,t+d)$ are homogeneously doped. The dark current density consists of electrons injected from the n side over the potential barrier into the p side and an analogous current due to holes injected from the p side into the n side. The current–voltage characteristic for an ideal diffusion-limited diode is given by

$$I_D=AJ_g\left[\exp\left(\frac{qV}{kT}\right)-1\right]. \tag{42}$$

For a junction with thick quasineutral regions the saturation current density is equal to

$$J_s=\frac{qD_hp_{n0}}{L_h}+\frac{qD_en_{p0}}{L_s}, \tag{43}$$

where[36,37]

$$J_s=\frac{qD_hp_{n0}}{L_h}\,\frac{\gamma_1{\rm ch}(x_n/L_h)+{\rm sh}(x_n/L_n)}{\gamma_1{\rm sh}(x_h/L_h)+{\rm ch}(x_h/L_h)}+\frac{qD_en_{\rm p0}}{L_e}\,\frac{\gamma_2{\rm ch}[(t+d-x_n-w)/L_e]+{\rm sh}[(t+d-x_n-w)/L_e]}{\gamma_2{\rm sh}[(t+d-x_n-w)/L_e]+{\rm ch}[(t+d-x_n-w)/L_e]} \tag{44}$$

in which case $\gamma_1=s_1L_h/D_h$, $\gamma_2=s_2L_e/D_e$, p_{n0}, and n_{p0} are the concentrations of minority carriers on both sides of the junction, s_1 and s_2 are the surface recombination velocities at the illuminated (for holes in n-type material) and back photodiode surface (for electrons in p-type material), respectively. The value of the saturation current density, J_s, depends on minority carrier diffusion lengths (L_e,L_h), minority carrier diffusion coefficients (D_e,D_h), surface recombination velocities (s_1,s_2), minority carrier concentrations (p_{n0}, n_{p0}) and junction design (x_n,t,w,d).

For nondegenerated statistics, $n_{n0}p_{n0}=n_i^2$, $D=(kT/q)\mu$ and $L=(D\tau)^{1/2}$ and then

$$J_s=(kT)^{1/2}n_i^2q^{1/2}\left[\frac{1}{p_{p0}}\left(\frac{\mu_e}{\tau_e}\right)^{1/2}+\frac{1}{n_{n0}}\left(\frac{\mu_h}{\tau_h}\right)^{1/2}\right]^{-1}, \tag{45}$$

where n_i is the intrinsic carrier concentration, p_{p0} and n_{n0} are the hole and electron majority carrier concentrations, and τ_e and τ_h the electron and hole lifetimes in the p- and n-type regions, respectively. Diffusion current varies with temperature as n_i^2.

The resistance at zero bias can be obtained from Eq. (40) by differentiation of $I-V$ characteristic

$$R_0=\frac{kT}{qI_n} \tag{46}$$

and then the R_0A product determined by diffusion current is

$$(R_0A)_D=\left(\frac{dJ_D}{dV}\right)^{-1}_{|V_s=0}=\frac{kT}{qJ_s}. \tag{47}$$

b. Quantum efficiency. Three regions contribute to photodiode quantum efficiency: two neutral regions of different types of conductivity and the spatial charge region (see Fig. 6). Thus[36,37]

$$\eta=\eta_n+\eta_{\mathrm{DR}}+\eta_p, \tag{48}$$

$$\eta_n=\frac{(1-r)\alpha L_h}{\alpha^2L_h^2-1}\left\{\frac{\alpha L_h+\gamma_1-e^{-\alpha x_n}[\gamma_1\mathrm{ch}(x_n/L_h)+\mathrm{sh}(x_n/L_h)]}{\gamma_1\mathrm{sh}(x_n/L_h)+\mathrm{ch}(x_n/L_h)}-\alpha L_he^{-\alpha x_n}\right\}, \tag{49}$$

$$\eta_p=\frac{(1-r)\alpha L_e}{\alpha^2L_e^2-1}e^{-\alpha(x_n+w)}\left\{\frac{(\gamma_2-\alpha L_e)e^{-\alpha(t+d-x_n-w)}-\mathrm{sh}[(t+d-x_n-w)/L_e]-\gamma_2\mathrm{ch}[(t+d-x_n-w)/L_e]}{\mathrm{ch}[(t+d-x_n-w)/L_e]-\gamma_2\mathrm{sh}[(t+d-x_n-w)/L_e]}+\alpha L_e\right\}, \tag{50}$$

$$\eta_{\mathrm{DR}}=(1-r)[e^{-\alpha x_n}-e^{-\alpha(x_n+w)}]. \tag{51}$$

In the following we shall consider the internal quantum efficiency, neglecting the losses due to reflection of the radiation from the illuminated photodiode surface. Obtaining high photodiode quantum efficiency requires that the illuminated region of the junction be sufficiently thin so that the generated carriers may reach the junction potential barrier by diffusion.

Normally, the photodiode is designed so that most of the radiation is absorbed in one side of the junction, e.g., in the p-type side in Fig. 6(a). This could be achieved in practice either by making the n-type region very thin or by using a heterojunction in which the band gap in the n region is larger than the photon energy so that most of the incident radiation can reach the junction without being absorbed. If the back contact is several minority carrier diffusion lengths, L_e away from the junction, the quantum efficiency is given by

$$\eta(\lambda)=(1-r)\frac{\alpha(\lambda)L_e}{1+\alpha(\lambda)L_e}. \tag{52}$$

If the back contact is less than a diffusion length away from the junction, the quantum efficiency tends to

$$\eta(\lambda)=(1-r)[1-e^{-\alpha(\lambda)d}], \tag{53}$$

where d is the thickness of the p-type region. It has been assumed that the back contact has zero surface recombination velocity and that no radiation is reflected from the back surface. Thus, if the above conditions hold, a high quantum efficiency can be achieved using an anti-reflection coating to minimize the reflectance of the front surface and ensuring that the device is thicker than the absorption length.

c. Noise. In comparison with photoconductive detectors, the two fundamental processes responsible for thermal noise mechanisms (fluctuations in the velocities of free carriers due to their random motion, and due to randomness in the rates of thermal generation and recombination) are less readily distinguishable in the case of junction devices, giving rise jointly to shot noise on the minority carrier components, which make up the net junction current. The random thermal motion is responsible for fluctuations in the diffusion rates in the neutral regions of junction devices and generation–recombination fluctuations both in the neutral regions and in the depletion region. We will show later that for a junction device at zero bias, i.e., when the net junction current is zero, the resulting noise is identical to Johnson noise associated with the incremental slope of the device.

A general theory of noise in photodiodes, which is applicable at arbitrary bias and to all sources of leakage current, has not been developed.[38] The intrinsic noise mechanism of a photodiode is shot noise in the current passing through the diode. It is generally accepted that the noise in an ideal diode is given by

$$I_n^2=[2q(I_D+2I_s)+4kT(G_j-G_0)]\Delta f, \tag{54}$$

where $I_D=I_s[\exp(qV/kT)-1]$, G_J is the conductance of the junction and G_0 is the low-frequency value of G_J. In the low-frequency region, the second term on the right-hand side is zero. For a diode in thermal equilibrium (i.e., without ap-

plied bias voltage and external photon flux) the mean-square noise current is just the Johnson–Nyquist noise of the photodiode zero bias resistance ($R_0^{-1}=qL_s/kT$)

$$I_n^2=\frac{4kT}{R_0}\,\Delta f \tag{55}$$

and

$$V_n^2=4kTR_0\Delta f. \tag{56}$$

Note that the mean-square shot noise in reverse bias is half the mean-square Johnson–Nyquist noise at zero bias. However, this predicted improvement in the diode noise in reverse bias is not normally observed in practice due to increased $1/f$ noise.

d. Detectivity. In the case of the photodiode, the photoelectric gain is usually equal to 1 so, according to Eq. (1), the current responsitivity is

$$R_i=\frac{q\lambda}{hc}\,\eta \tag{57}$$

and detectivity [see Eq. (3)] can be determined as

$$D^*=\frac{\eta\lambda q}{hc}\left[\frac{A}{2q(I_D+2I_s)}\right]^{1/2}. \tag{58}$$

In reverse biases, I_d tends to $-I_s$ and the expression in brackets tends to I_s.

From the discussion it is shown that the performance of an ideal diffusion-limited photodiode can be optimized by maximizing the quantum efficiency and minimizing the reverse saturation current, I_s. For a diffusion-limited photodiode, the general expression for the saturation current of electron from the p-type side is [see Eq. (44)]

$$I_s^p=A\,\frac{qD_en_{p0}}{L_e}\,\frac{\mathrm{sh}(d/L_e)+(s_2L_e/D_e)\mathrm{ch}(d/L_e)}{\mathrm{ch}(d/L_e)+(s_2L_e/D_e)\mathrm{sh}(d/L_e)}. \tag{59}$$

It is normally possible to minimize the leakage current from the side which does not contribute to the photosignal. The minority carrier generation rate and hence the diffusion current can be greatly reduced, in theory at least, by increasing doping or the band gap on the inactive side of the junction.

If the back contact is several diffusion lengths away from the junction, then Eq. (59) tends to

$$I_s=\frac{qD_en_{p0}}{L_s}\,A. \tag{60}$$

As the back contact is brought closer to the junction, the leakage current can either increase or decrease, depending on whether the surface recombination velocity is greater than the diffusion velocity D_e/L_e. In the limiting case where $d\ll L_e$, the saturation current is reduced by a factor d/L_e relative to Eq. (60) for $s=0$ and increased by a factor of L_e/d for $s=\infty$. If the surface recombination velocity is small then Eq. (59) can usually be written in the form

$$I_s=qGV_{\mathrm{diff}}, \tag{61}$$

where G is the bulk minority carrier generation rate per unit volume and V_{diff} is the effective volume of material from which the minority carriers diffuse to the junction. The effective volume is AL_e for $L_e\ll d$ and tends to Ad for $L_e\gg d$. For p-type material, the generation rate is given by

$$G=\frac{n_{p0}}{\tau_e}=\frac{n_i^2}{N_d\tau}. \tag{62}$$

The discussion indicates that the performance of the device is strongly dependent on the properties of the back contact. The most common solution to this problem is to move the back contact many diffusion lengths away to one side and to ensure that all the surfaces are properly passivated. Alternatively, the back contact itself can sometimes be designed to have a low surface recombination velocity by introducing a barrier for minority carriers between the metal contact and the rest of the device. This barrier can be made by increasing the doping or the band gap near the contact, which effectively isolates the minority carriers from the high recombination rate at the contact.

2. Other current mechanisms

In the previous section, photodiodes were analyzed in which the dark current was limited by diffusion. However, this behavior is not always observed in practice, especially for wide-gap semiconductor p-n junctions. Several additional excess mechanisms are involved in determining the dark current–voltage characteristics of the photodiode. The dark current is the superposition of current contributions from three diode regions: bulk, depletion region, and surface. Between them we can distinguish:

1. Thermally generated current in the bulk and depletion region

(a) diffusion current in the bulk p and n regions,
(b) generation–recombination current in the depletion region,
(c) band-to-band tunneling,
(d) intertrap and trap-to-band tunneling,
(e) anomalous avalanche current,
(f) ohmic leakage across the depletion region,

2. Surface leakage current

(a) surface generation current from surface states,
(b) generation current in a field-induced surface depletion region,
(c) tunneling induced near the surface,
(d) ohmic or nonohmic shunt leakage,
(e) avalanche multiplication in a field-induced surface region.

3. Space-charge limited current.

Figure 7 illustrates schematically some of these mechanisms. Each of the components has its own individual relationship to voltage and temperature. On account of this, many researchers analyzing the $I-V$ characteristics assume that only one mechanism dominates in a specific region of the diode bias voltage. This method of analysis of the diode's $I-V$ curves is not always valid. A better solution is to numerically fit the sum of the current components to experimental data over a range of both applied voltage and temperature.

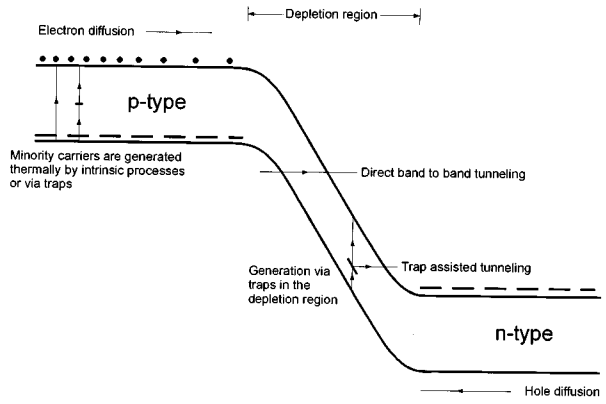

FIG. 7. Schematic representation of some of the mechanisms by which dark current is generated in a reverse-biased p-n junction (after Ref. 31).

Below, we will be concerned with the current contribution of high quality photodiodes with high R_0A products limited by:

(1) generation–recombination within the depletion region,
(2) tunneling through the depletion region,
(3) surface effects,
(4) impact ionization,
(5) space-charge limited current.

a. Generation–recombination current. The importance of this current mechanism was first pointed out by Sah *et al.*,[39] and was later extended by Choo.[40] It appears that one space-charge region generation–recombination current could be more important than its diffusion current, especially at low temperatures, although the width of the space-charge region is much less than the minority carrier diffusion length. The generation rate in the depletion region can be very much greater than in the bulk of the material. In reverse bias, the current can be given by an equation similar to Eq. (61),

$$I=qG_{\mathrm{dep}}V_{\mathrm{dep}}, \tag{63}$$

where g_{dep} is the generation rate and V_{dep} is the volume of the depletion region. In particular, the generation rate from traps in the depletion region is given by the Shockley-Read–Hall formula

$$G_{\mathrm{dep}}=\frac{n_i^2}{n_1\tau_{e0}+p_1\tau_{n0}}, \tag{64}$$

where n_1 and p_1 are the electron and hole concentrations which would be obtained if the Fermi energy was at the trap energy and τ_{e0} and τ_{h0} are the lifetimes in strongly n-type and p-type material. Normally, one of the terms in the denominator of Eq. (64) will dominate and for the case of a trap at the intrinsic level holds n_i and $p_i=n_i$, giving

$$G_{\mathrm{dep}}=\frac{n_i}{\tau_0} \tag{65}$$

and then the generation–recombination current of the depletion region is equal

$$J_{\mathrm{GR}}=\frac{qwn_i}{\tau_0}. \tag{66}$$

The comparison of Eqs. (62) and (65) indicates that the generation rate in the bulk of the material is proportional to n_i^2, whereas the generation rate in the depletion region is proportional to n_i for a midgap state. The generation–recombination current varies roughly as the square root of the applied voltage ($w\sim V^{1/2}$) for the case of an abrupt junction, or as the cube root ($w\sim V^{1/2}$) for a linearly graded junction. This behavior, in which the current increases with reverse bias, can be contrasted with a diffusion-limited diode, where the reverse current is independent of voltage above a few kT/q.

Space-charge region generation–recombination current varies with temperature as n_i, i.e., less rapidly than diffusion current which varies as n_i^2.

The zero bias resistance can be found by differentiating Eq. (66) and setting $V=0$

$$(R_0A)_{\mathrm{GR}}=\left(\frac{dJ_{\mathrm{GR}}}{dV}\right)^{-1}_{|V=0}=\frac{2V_b\tau_0}{qn_iw}, \tag{67}$$

where $V_b=kT\ln(N_aN_d/n_i^2)$. In evaluating Eq. (67), the term of greatest uncertainty is τ_0.

b. Tunneling current. The third type of dark current component that can exist is a tunneling current caused by electrons directly tunneling across the junction from the valence band to the conduction band (direct tunneling) or by electrons indirectly tunneling across the junction by way of intermediate trap sites in the junction region [indirect tunneling or trap-assisted tunneling (see Fig. 7)].

The usual direct tunneling calculations assume a particle of constant effective mass incident on a triangular or parabolic potential barrier.[41] For the triangular potential barrier

$$J_T=\frac{q^2EV_b}{4\pi^2\hbar^2}\left(\frac{2m^*}{E_g}\right)^{1/2}\exp\left[-\frac{4(2m^*)^{\frac{1}{2}}E_g^{3/2}}{3q\hbar E}\right]. \tag{68}$$

For an abrupt p-n junction the electric field can be approximated by

$$E=\left[\frac{2q}{\varepsilon_0\varepsilon_s}\left(\frac{E_g}{q}\pm V_b\right)\frac{np}{n+p}\right]^{1/2}. \tag{69}$$

The tunnel current is seen to have an extremely strong dependence on energy gap, applied voltage, and an effective doping concentration $N_{\mathrm{ef}}=np/(n+p)$. It is relatively insensitive to temperature variation and the shape of the junction barrier. For the parabolic barrier[41]

$$J_T\propto\exp\left[-\frac{(\pi m^*)^{1/2}E_g^{3/2}}{2^{3/2}q\hbar E}\right]. \tag{70}$$

Apart from direct band-to-band tunneling, tunneling is possible by means of indirect transitions in which impurities or defects within the space-charge region act as intermediate states. This is a two-step process in which one step is a thermal transition between one of the bands and the trap and the other is tunneling between the trap and the other band. The tunneling process occurs at lower fields than direct band-to-band tunneling because the electrons have a shorter distance to tunnel (see Fig. 7).

c. Surface leakage current. In a real p-n junction, particularly in wide gap semiconductors and at low tempera-

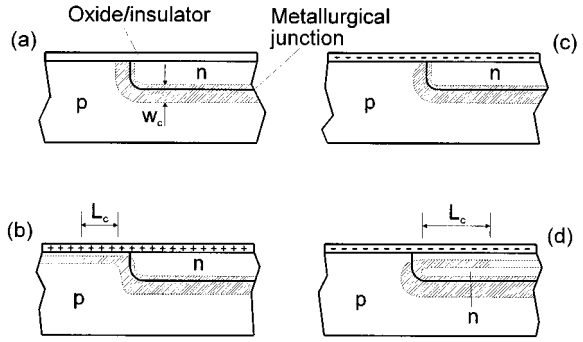

FIG. 8. Effect of fixed insulator charge on the effective junction space-charge region: (a) flatband condition; (b) positive fixed charge (inversion of the p side, formation of an n-type surface channel); (c) negative fixed channel (accumulation of the p side, field induced junction at the surface); (d) large negative fixed charge (inversion of the n side, formation of p-type surface channel).

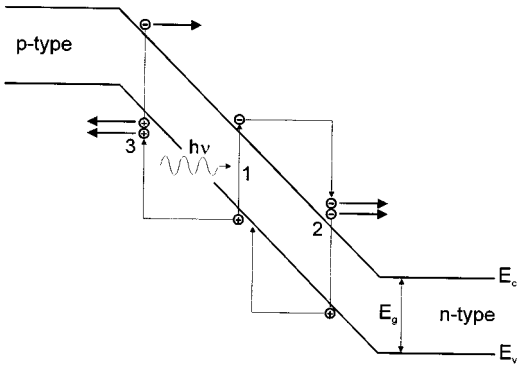

FIG. 9. Schematic representation of the multiplication process in an APD.

tures, additional dark current related to the surface occurs. Surface phenomena play an important part in determining photovoltaic detector performance. The surface provides a discontinuity which can result in a large density of interface states. These generate minority carriers by the Shockley–Read–Hall (SRH) mechanism, and can increase both the diffusion and depletion region generated currents. The surface can also have a net charge, which affects the position of the depletion region at the surface.

The surface of actual devices is passivated in order to stabilize the surface against chemical and heat-induced changes as well as to control surface recombination, leakage, and related noise. Native oxides and overlying insulators are commonly employed in p-n junction fabrication which introduce fixed charge states which then induce accumulation or depletion at the semiconductor-insulator surface. We can distinguish three main types of states on the semiconductor-insulator interface, namely, fixed insulator charge, low surface states, and fast surface states. The fixed charge in the insulator modifies the surface potential of the junction. A positively charged surface pushes the depletion region further into the p-type side and a negatively charged surface pushes the depletion region towards the n-type side. If the depletion region is moved towards the more highly doped side, the field will increase, and tunneling becomes more likely. If it is moved towards the more lightly doped side, the depletion region can extend along the surface, greatly increasing the depletion region generated currents. When sufficient fixed charge is present, accumulated and inverted regions as well as n-type and p-type surface channels are formed (see Fig. 8). An ideal surface would be electrically neutral and would have a very low density of surface states. The ideal passivation would be a wide gap insulator grown with no fixed charge at the interface.

Fast interface states, which act as generation–recombination centers, and fixed charge in the insulator cause a variety of surface-related current mechanisms. The kinetics of generation–recombination through fast surface states is identical to that through bulk SRH centers. The current in a surface channel is given by [see Eq. (66)]

$$I_{\mathrm{GRS}}=\frac{qn_i w_c A_c}{\tau_0}, \tag{71}$$

where w_c is the channel width and A_c is the channel area.

Apart from generation–recombination processes occurring at the surface and within surface channels, there are other surface-related current mechanisms, termed surface leakage, with ohmic or breakdownlike current–voltage characteristics. They are nearly temperature independent. Surface breakdown occurs in a region of high electric field [Fig. 8(c), where the depletion layer intersects the surface; Fig. 8(d), very narrow depletion layer].

Band bending at the p-n junction surface can be controlled by a gate electrode overlaid around the junction perimeter on an insulating film.

The dark current as a sum of several independent contributions can also be written as follows:

$$I=I_s\left[\exp\frac{q(V-IR_s)}{\beta kT}-1\right]+\frac{V-IR_s}{R_{\mathrm{sh}}}+I_T, \tag{72}$$

where R_s is the series resistance and R_{sh} is the shunt resistance of the diode. In the case of predominant diffusion current the β coefficient approaches unity; but when the generation–recombination current is mainly responsible for carrier transport, β equals 2.

d. Impact ionization, avalanche photodiode. When the electric field in a semiconductor is increased above a certain value, the carriers gain enough energy (greater than the band gap) so that they can excite electron–hole pairs by impact ionization. An avalanche photodiode (APD) operates by converting each detected photon into a cascade of moving carrier pairs. The device is a strongly reverse-biased photodiode in which the junction electric field is large; the charge carriers therefore accelerate, acquiring enough energy to excite new carriers by the process of impact ionization.

The avalanche multiplication process is illustrated in Fig. 9. A photon absorbed at point 1 creates an electron-hole pair. The electron accelerates under the effect of the strong electric field. The acceleration process is constantly interrupted by random collisions with the lattice in which the electron loses some of its acquired energy. These competing processes cause the electron to reach an average saturation velocity. The electron can gain enough kinetic energy that, upon collision with an atom, it can break the lattice bonds,

creating a second electron-hole pair. This is called impact ionization (at point 2). The newly created electron and hole both acquire kinetic energy from the field and create additional electron-hole pairs (e.g., at point 3). These in turn continue the process, creating other electron-hole pairs. This process is therefore called avalanche multiplication.

The abilities of electrons and holes to impact ionize are characterized by the ionization coefficients α_e and α_h. These quantities represent ionization probabilities per unit length. The ionization coefficients increase with the depletion layer electric field and decrease with increasing device temperature.

An important parameter for characterizing the performance of an APD is the ionization ratio $k=\alpha_h/\alpha_e$. When holes do not ionize appreciably (i.e., $\alpha_h \ll \alpha_e$, $k \ll 1$), most of the ionization is achieved by electrons. The avalanching process then proceeds principally from left to right (i.e., from the p side to n side) in Fig. 9. It terminates some time later when all the electrons arrive at the n side of the depletion layer. If electrons and holes both ionize appreciably ($k \approx 1$), on the other hand, those holes moving to the left create electrons that move to the right, which, in turn, generate further holes moving to the left, in a possibly unending circulation. Although this feedback process increases the gain of the device (i.e., the total generated charge in the circuit per photocarrier pair), it is nevertheless undesirable for several reasons: it is time consuming and therefore reduces the device bandwidth, it is random and therefore increases the device noise, and it can be unstable, thereby causing avalanche breakdown. It is therefore desirable to fabricate APDs from materials that permit only one type of carrier (either electrons or holes) to impact ionize. If electrons have the higher ionization coefficient, for example, optimal behavior is achieved by injecting the electron of a photocarrier pair at the p edge of the depletion layer and by using a material whose value of k is as low as possible. If holes are injected, the hole of a photocarrier pair should be injected at the n edge of the depletion layer and k should be as large as possible. The ideal case of single-carrier multiplication is achieved when $k=0$ or ∞.

In an optimally designed photodiode, the geometry of the APD should maximize photon absorption (for example, by assuming the form of a p-i-n structure) and the multiplication region should be thin to minimize the possibility of localized uncontrolled avalanches (instabilities or microplasmas) being produced by strong electric field. Greater electric-field uniformity can be achieved in a thin region. These two conflicting requirements call for an APD design in which the absorption and multiplication regions are separate. For example, Fig. 10 shows a reach-through p^+-π-p-n^+ APD structure which accomplishes this. Photon absorption occurs in the wide π region (very lightly doped p region). Electrons drift through the π region into a thin p-n^+ junction, where they experience a sufficiently strong electric field to cause avalanching. The reverse bias applied across the device is large enough for the depletion layer to reach through the p and π regions into the p^+ contact layer.

A comprehensive theory of avalanche noise in APDs

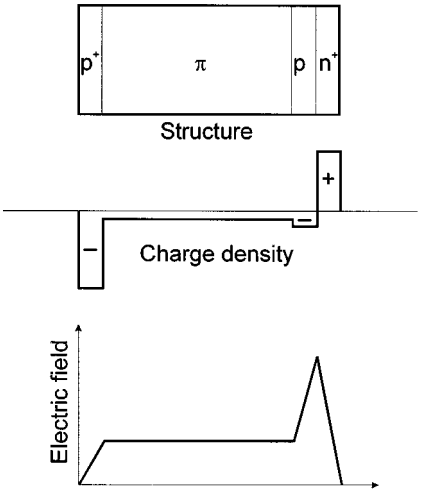

FIG. 10. Reach-through p^+-π-p-n^+ APD structure.

was developed by McIntyre.[42] The noise of an APD per unit bandwidth can be described by the formula

$$\langle I_n^2 \rangle = 2qI_{\rm ph}\langle M \rangle^2 F, \tag{73}$$

where $I_{\rm ph}$ is unmultiplied photocurrent (signal), $\langle M \rangle$ is the average avalanche gain and F is the excess noise factor which turns out to be related to the mean gain and the ionization ratio by

$$F = k\langle M \rangle + (1-k)\left(1 - \frac{1}{\langle M \rangle}\right). \tag{74}$$

In p-n and p-i-n reverse-biased photodiodes without gain, $\langle M \rangle = 1$, $F=1$ and the well-known shot noise formula will indicate the device's noise performance. In the avalanche process, if every injected photocarrier underwent the same gain M, the factor would be unity, and the resulting noise power would only be the input shot noise due to the random arrival of signal photons, multiplied by the gain squared. The avalanche process is, instead, intrinsically statistical, so that individual carriers generally have different avalanche gains characterized by a distribution with an average $\langle M \rangle$. This causes additional noise called avalanche excess noise, which is conveniently expressed by the F factor in Eq. (74). As was mentioned above, to achieve a low F, not only must α_e and α_h be as different as possible, but also the avalanche process must be initiated by carriers with the higher ionization coefficient. According to McIntyre's rule, the noise performance of ADP can be improved by more than a factor of 10 when the ionization ratio is increased to 5.

e. Space-charge limited current. In the case of wide band-gap p-n junctions, the forward current–voltage characteristics are often described by equation

$$J \propto \exp\left(\frac{qV}{\beta kT}\right), \tag{75}$$

where the diode ideality factor $\beta > 2$. This value of β does not fall within the range that results when diffusion current ($\beta=1$) or depletion layer current ($\beta=2$) dominate the

forward-bias current conduction. This behavior is typical for an insulator with shallow and/or deep traps and thermally generated carriers.

Space-charge limited (SCL) current flow in solids has been considered in detail by Rose,[43] Lampert, and Mark[44,45] They loosely defined materials with $E_g \leqslant 2$ eV as semiconductors and those with $E_g \geqslant 2$ eV as insulators. It means, e.g., that GaN could be considered as an insulator.

When a sufficiently large field is applied to an insulator with ohmic contacts, electrons will be injected into the bulk of the material to form a current which is limited by space-charge effects. When trapping centers are present, they capture many of the injected carriers, thus reducing the density of free carriers.

At low voltages where the injection of carriers into the semiinsulating material is negligible, Ohm's law is obeyed and the slope of the $J-V$ characteristics defines the resistivity ρ of the material. At some applied voltage V_{TH} the current begins to increase more rapidly than linearly with applied voltages. Here V_{TH} is given by

$$V_{\mathrm{TH}} = 4\pi \times 10^{12} q p_t \frac{t^2}{\varepsilon}, \tag{76}$$

where t is the thickness of the semiinsulating material, and p_t is the density of trapped holes, if one carrier (holes) space-charge limited current is considered. As the voltage is continuously increased beyond V_{TH} additional excess holes are injected into the material and the current density is given by

$$J = 10^{-13} \mu_h \varepsilon \theta \frac{V^2}{t^2}, \tag{77}$$

where θ is the probability of trap occupation determined as a ratio of the densities of free to trapped holes. Here θ is given by

$$\theta = \frac{p}{p_t} = \frac{N_v}{N_t} \exp\left(-\frac{E_t}{kT}\right), \tag{78}$$

where N_v is the effective density of states in the valence band, N_t is the density of traps, and E_t is the depth of traps from the top of the valence band. When the applied voltage further increases, the square-law region of Eq. (77) will terminate in a steeply rising current which increases until it becomes the trap-free SCL currents given by

$$J = 10^{-13} \mu_h \varepsilon \frac{V^2}{t^2}. \tag{79}$$

The density of traps N_t can be determined from the voltage V_{TFL} at which the traps are filled and the currents rise sharply

$$V_{\mathrm{TFL}} = 4\pi \times 10^{12} q N_t \frac{t^2}{\varepsilon}. \tag{80}$$

The trap depth E_t can also be calculated from the Eq. (80) using the value of N_t. But if Eq. (77) is measured as the function of temperature and a plot of $\ln(\theta T^{3/2})$ vs $1/T$ is possible, E_t and N_t can be obtained directly from these data without referring to Eq. (80).

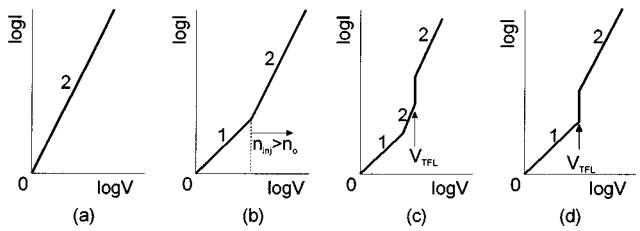

FIG. 11. Schematic drawings of the logarithmic dependence of current vs voltage for (a) an ideal insulator, (b) a trap-free insulator with thermally generated free carriers, (c) an insulator with shallow traps and thermal free carriers, and (d) an insulator with deep traps and thermal-free carriers (after Ref. 46).

For the purpose of illustration of the above phenomenon in semiinsulating materials, consider the four log J vs log V graphs in Fig. 11. Figure 11(a) represents an ideal insulator where $I \propto V^2$, indicating SCL current flow. In other words, there are no thermally generated carriers resulting from impurity-band or band-to-band transitions; the conduction is only within the conduction band as a result of carrier injection. As shown in Fig. 11(b), ohmic conduction is obtained in trap-free insulators in the presence of thermally generated free carriers, n_0. When the injected carrier density n_{inj} exceeds $n_0 (n_{\mathrm{inj}} > n_0)$, ideal insulator characteristics are observed ($I \propto V^2$). Shallow traps contribute to an $I \propto V^2$ regime at a lower voltage followed by a sharp transition to an ideal insulator, square-law regime as shown in Fig. 11(c). The sharp transition corresponds to an applied voltage. V_{TFL} required to fill a discrete set of traps which are initially unoccupied. Figure 11(d) illustrates the case of a material with deep traps which have become filled when n_{inj} becomes comparable to n_o. The voltage at which this occurs is V_{TFL}. Therefore, at $V < V_{\mathrm{TFL}}$ ohmic conduction is observed and at $V > V_{\mathrm{TFL}}$ SCL current flow dominates.

3. Response time

The upper-frequency response of a photodiode may be determined by basically three effects: the time of carrier diffusion to the junction depletion region, τ_0; the transit time of carrier drift across the depletion region, τ_s; and the RC time constant associated with circuit parameters including the junction capacitance C and the parallel combination of diode resistance and external load (the series resistance is neglected).

Photodiodes designed for fast response are generally constructed so that the absorption of radiation occurs in the p-type region. This ensures that most of the photocurrent is carried by electrons which are more mobile than holes (whether by diffusion or drift). The frequency response for the diffusion process in a backside illuminated diode has been calculated by Sawyer *et al.*[47] as a function of diode thickness, diffusion constant, absorption depth, minority carrier lifetime, and surface-recombination velocity. Assuming that the diffusion length is greater than both the diode thickness and the absorption depth, the cutoff frequency where the response drops by $\sqrt{2}$, is given by[31]

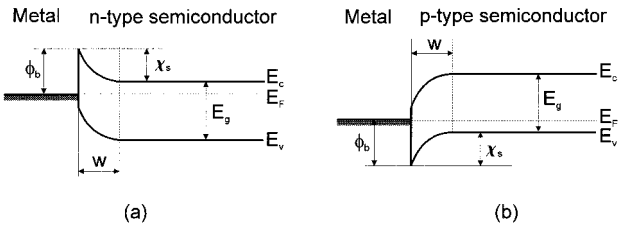

FIG. 12. Equilibrium energy band diagram of Schottky barrier junctions: (a) metal-(n-type) semiconductor, (b) metal-(p-type) semiconductor.

$$f_{\text{diff}}=\frac{2.43D}{2\pi t^2}, \tag{81}$$

where D is the diffusion constant and t is the diode thickness.

The depletion region transit time is equal to

$$\tau_t=\frac{w_{\text{dep}}}{v_s}, \tag{82}$$

where w_{dep} is the depletion region width and v_s is the carrier saturation drift velocity in the junction field, which has a value of about 10^7 cm/s. The frequency response of a transit time limited diode has been derived by Gartner.[48]

In practice the most serious limitation arises from the RC time constant, which for an abrupt junction is given by

$$\tau_{RC}=\frac{AR_T}{2}\left(\frac{q\varepsilon_0\varepsilon_s N}{V}\right)^{1/2}. \tag{83}$$

$R_T=R_d(R_s+R_L)/(R_s+R_d+R_L)$ where R_s, R_d, and R_L are the series, diode, and load resistances. To reduce the RC time constant, we can decrease the majority carrier concentration adjacent to the junction, increase V by means of a reverse bias, decrease the junction area, or lower either the diode resistance or the load resistance. Except for the application of a reverse bias, all of these changes reduce the detectivity. The trade-off between response time and detectivity is then apparent.

D. Schottky barrier photodiodes

Schottky barrier photodiodes have been studied quite extensively[41] and have also found application as ultraviolet detectors. These devices reveal some advantages over p-n junction photodiodes: fabrication simplicity, absence of high-temperature diffusion processes, and high speed of response.

1. Schottky–Mott theory and its modifications

According to a simple Schottky–Mott model, the rectifying property of the metal-semiconductor contact arises from the presence of an electrostatic barrier between the metal and the semiconductor which is due to the difference in work functions ϕ_m and ϕ_s of the metal and semiconductor, respectively. For example, for a metal contact with an n-type semiconductor, ϕ_m should be greater, while for a p-type semiconductor it should be less than ϕ_s. The barrier heights in both these cases, shown in Figs. 12(a) and 12(b), are given by

$$\phi_{\text{bn}}=\phi_m-\chi_s \tag{84}$$

and

$$\phi_{\text{bp}}=\chi_s+E_g-\phi_m, \tag{85}$$

respectively, where χ_s is the electron affinity of the semiconductor. The potential barrier between the interior of the semiconductor and the interface, known as band bending, is given by

$$\psi_s=\phi_m-\phi_s \tag{86}$$

in both cases. If $\phi_b>E_g$, the layer of the p-type semiconductor adjacent to the surface is inverted in type and we have a p-n junction within the material. However, in practice the built-in barrier does not follow such a simple relationship with ϕ_m and is effectively reduced due to interface states originating either from surface states or from metal-induced gap states and/or due to interface chemical reactions of metal and semiconductor atoms.

In the literature, there are numerous and considerable variations among experimental data on ϕ_m.[49] Their analysis indicates an empirical relationship of the type[60]

$$\phi_b=\gamma_1\phi_m+\gamma_2, \tag{87}$$

where γ_1 and γ_2 are constants characteristic of the semiconductors. Two limit cases, namely $\gamma_1=0$ and $\gamma_1=1$ indicative of Bardeen barrier (when influence of localized surface states is decisive) and ideal Schottky barrier, respectively, can be visualized from such an empirical relation. It has also been pointed out by various workers that the slope parameter $\gamma_1=\partial\phi_b/\partial\phi_m$ can be used for describing the extent of Fermi level stabilization or pinning for a given semiconductor. The parameters γ_1 and γ_2 have been used by some workers for estimating the interface state density.

It was shown by Cowley and Sze[50] that, according to the Bardeen model, the barrier height in the case of an n-type semiconductor is given approximately by

$$\phi_{\text{on}}=\gamma(\phi_m-\chi_s)+(1-\gamma)(E_g-\phi_0)-\Delta\phi, \tag{88}$$

where $\gamma=\varepsilon_i(\varepsilon_i+q\delta D_g)$. The term ϕ_0 is the position of the neutral level of the interface states measured from the top of the valence band, $\Delta\phi$ is the barrier lowering due to image forces, δ is the thickness of the interfacial layer, and ε_i its total permittivity. The surface states are assumed to be uniformly distributed in energy within the band gap, with a density D_g per electron volt per unit area. If there are not surface states, $D_g=0$, and neglecting $\Delta\phi$, Eq. (88) reduces to Eq. (84). If the density of states is very high, γ becomes very small and ϕ_{bn} approaches the value $E_g-\phi_0$. This is because a very small deviation of the Fermi level from the neutral level can produce a large dipole moment, which stabilizes the barrier height by a sort of negative feedback effect. The Fermi level is pinned relative to the band edges by the surface states.

A similar analysis for the case of a p-type semiconductor shows that ϕ_{bp} is approximately given by

$$\phi_{\text{bp}}=\gamma(E_g-\phi_m+\chi_s)+(1-\gamma)\phi_0. \tag{89}$$

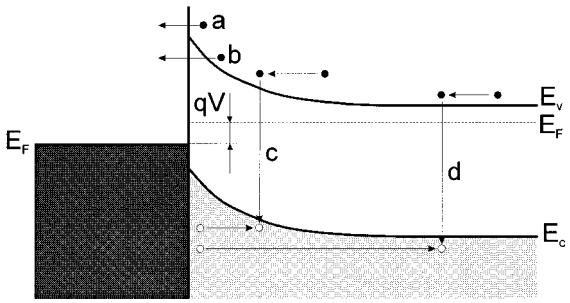

FIG. 13. Four basic transport processes in forward-biased Schottky barrier on an *n*-type semiconductor (after Ref. 49).

Hence if ϕ_{bn} and ϕ_{bp} refer to the same metal on *n*- and *p*-type specimens of the same semiconductor, we should have

$$\phi_{bn}=\phi_{bp}\cong E_g \tag{90}$$

if the semiconductor surface is prepared in the same way in both cases, so that δ, ε_i, D_g, and ϕ_0 are the same. This relationship holds quite well in practice. It is usually true that $\phi_{bn}>E_g/2$, and $\phi_{bn}>\phi_{bp}$.

2. Current transport processes

The current transport in metal-semiconductor contacts is due mainly to majority carriers, in contrast to *p*-*n* junctions, where current transport is due mainly to minority carriers. The current can be transported in various ways under forward bias conditions as shown in Fig. 13. The four processes are:[49]

(a) emission of electrons from the semiconductor over the top of the barrier into the metal,
(b) quantum mechanical tunneling through the barrier,
(c) recombination in the space-charge region,
(d) recombination in the neutral region (equivalent hole injection from the metal to the semiconductor).

The inverse processes occur under reverse bias. In addition, we may have edge leakage current due to a high electric field at the contact periphery or interface current due to traps at the metal-semiconductor interface.

The transport of electrons over the potential barrier have been described by various theories, namely: diffusion,[51,52] thermionic emission,[53] and unified thermionic emission diffusion.[50] It is now widely accepted that, for high-mobility semiconductors with impurity concentrations of practical interest, the thermionic emission theory appears to explain qualitatively the experimentally observed $I-V$ characteristics.[54] Some workers[55] have also included in the simple thermionic theory the quantum effects (i.e., quantum-mechanical reflection and tunneling of carriers through the barrier) and have tried to obtain modified analytical expressions for the current–voltage relation. This, however, has essentially led to a lowering of the barrier height and a rounding off of the top.

The thermionic emission theory by Bethe[53] is derived from the assumptions that the barrier height is much larger than kT, thermal equilibrium is established at the plane that determines emission, and the existence of a net current flow does not affect this equilibrium. Bethe's criterion for the slope of the barrier is that the barrier must decrease by more than kT over a distance equal to the scattering length. The resulting current flow will depend only on the barrier height and not on the width, and the saturation current is not dependent on the applied bias. Then the current density of majority carriers from the semiconductor over the potential barrier into the metal is expressed as

$$J_{MSt}=J_{st}\left[\exp\left(\frac{qV}{\beta kT}\right)-1\right], \tag{91}$$

where saturation current density

$$J_{st}=A^*T^2\exp\left(-\frac{\phi_b}{kT}\right) \tag{92}$$

and $A^*=4\pi qk^2m^*/h^3$ equal $120(m^*/m)$ A cm^{-2} K^{-2} is the Richardson constant, m^* is the effective electron mass, and β is an empirical constant close to unity. Equation (91) is similar to the transport equation for *p*-*n* junctions. However, the expression for the saturation current densities are quite different.

It appears that the diffusion theory is applicable to low-mobility semiconductors and the current density expressions of the diffusion and thermionic emission theories are basically very similar. However, the saturation current density for the diffusion theory

$$J_{sd}=\frac{q^2D_eN_c}{kT}\left[\frac{q(V_{bi}-V)2N_d}{\varepsilon_0\varepsilon_s}\right] \tag{93}$$

varies more rapidly with the voltage but is less sensitive to temperature compared with the saturation current density J_{st} of the thermionic emission theory.

A synthesis of the thermionic emission and diffusion approaches described above has been proposed by Crowell and Sze.[50] They assumed Bethe's criterion for the validity of the thermionic emission (the mean free path should exceed the distance within which the barrier falls by kT/q from its maximum value) and also took into account the effects of optical phonon scattering in the region between the top of the barrier and the metal and of the quantum mechanical reflection of electrons which have sufficient energy to surmount the barrier. Their combined effect is to replace the Richardson constant A^* with $A^{**}=f_pf_qA^*$, where f_p is the probability of an electron reaching the metal without being scattered by an optical phonon after having passed the top of the barrier, and f_q is the average transmission coefficient. The terms f_p and f_q depend on the maximum electric field in the barrier, the temperature, and the effective mass. Generally speaking, the product f_pf_q is on the order of 0.5.

3. R_0A product and responsivity

Knowing J_{st} with Eq. (92), R_0A can be calculated from

$$(R_0A)_{MS}=\left(\frac{dJ_{MSt}}{dV}\right)^{-1}_{|V=0}=\frac{kT}{qJ_{st}}=\frac{k}{qA^*T}\exp\left(\frac{\phi_b}{kT}\right). \tag{94}$$

According to Eq. (1), the current responsivity may be written in the form

$$R_i = \frac{q\lambda}{hc}\,\eta \tag{95}$$

and the voltage responsivity

$$R_v = \frac{q\lambda}{hc}\,\eta R, \tag{96}$$

where $R = (dI/dV)^{-1}$ is the differential resistance of the photodiode.

E. Comparison of different types of semiconductor photodetectors

At this point it is important to discuss some important differences between photoconductive, *p-n* junction and Schottky barrier detectors.

The photoconductive detectors exhibit the important advantage of the internal photoelectric gain, which relaxes requirements to a low noise preamplifier. The advantages of *p-n* junction detectors relative to photoconductors are: low or zero bias currents; high impedance, which aids coupling to read-out circuits in focal plane arrays; capability for high-frequency operation and the compatibility of the fabrication technology with planar-processing techniques. In comparison with Schottky barriers, the *p-n* junction photodiodes also indicate some important advantages. The thermionic emission process in Schottky barrier is much more efficient than the diffusion process and, therefore, for a given built-in voltage, the saturation current in a Schottky diode is several orders of magnitude higher than in the *p-n* junction. In addition, the built-in voltage of a Schottky diode is smaller than that of a *p-n* junction with the same semiconductor. However, high-frequency operation of *p-n* junction photodiodes is limited by the minority-carrier storage problem. In other words, the minimum time required to dissipate the carriers injected by the forward bias is dictated by the recombination lifetime. In a Schottky barrier, electrons are injected from the semiconductor into the metal under forward bias if the semiconductor is *n* type. Next they thermalize very rapidly ($\approx 10^{14}$ s) by carrier–carrier collisions, and this time is negligible compared to the minority-carrier recombination lifetime.

F. Semiconductor materials used for ultraviolet detectors

Different semiconductor compounds have been used to fabricate photodetectors with spectral responses in the UV region. Figure 14 shows the spectral detectivity of optical detectors responding in the 0.1–1.2 μm region. Note that detectivity is not D^*, but rather reciprocal of NEP for a 1 Hz bandwidth. This figure of merit is employed to include photomultipliers whose noise does not in all cases depend upon the square root of the photocathode area. Table II lists the areas which Seib and Aukerman[30] state are proper to the various detectors illustrated. The reader can convert to the D^* values appropriate to the photoconductive and photovoltaic detectors by multiplying the detectivity value illustrated by the square root of the detector area. The signal fluctuation limit shown in Table II is independent of area (see Sec. III A).

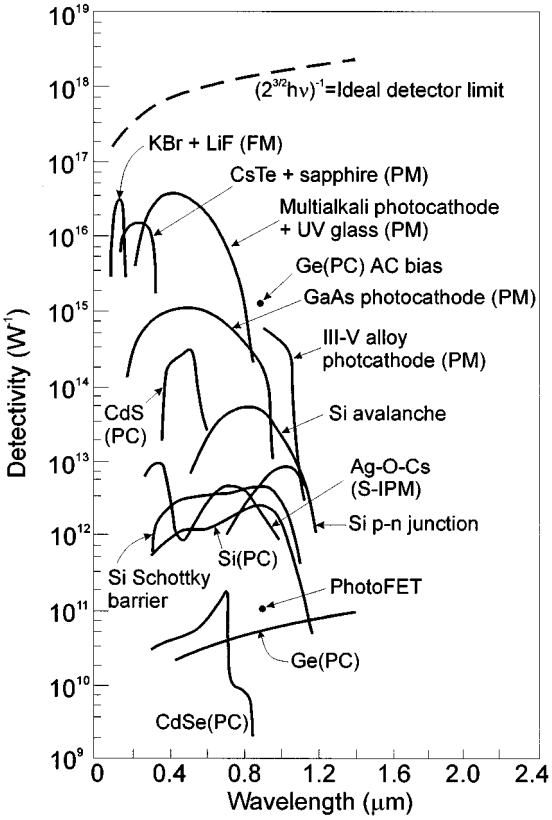

FIG. 14. Detectivity vs wavelength values of 0.1–1.2 μm photodetectors. PC indicates a photoconductive detector and PM indicates a photomultiplier. Detector areas are given in Table II (after Ref. 26).

Historically, the development of a high quantum efficiency semiconductor detectors in the whole UV range has been hampered by the extremely strong absorption and strong radiation induced aging effects in most of the semiconductor materials. It is especially visible in the case of silicon which, due to mature technology, is the most popular semiconductor material used for fabrication of UV detectors. For this semiconductor the photon penetration depth ranged from less than 10 nm in the NUV and MUV to 100 μm for 10 keV x rays [see Fig. 15(a)].[8] The absorption lengths for three semiconductor materials, Si, GaAs, and GaP as well as for SiO_2 and Au (photoemissive gold diode is the most com-

TABLE II. Areas of detectors illustrated in Fig. 14.

Detector	Area (cm^2)
CdS photoconductor (PC)	1
CdSe photoconductor (PC)	1
Si Schottky barrier photodiode	0.03
Si *p-n* junction photodiode	0.25
Si photoconductor	0.25
Si avalanche photodiode	0.07
Ge photoconductor (PC)	0.20
Ge ac bias photoconductor (PC)	2.4×10^{-5}
Photomultiplier (PM)	1.0

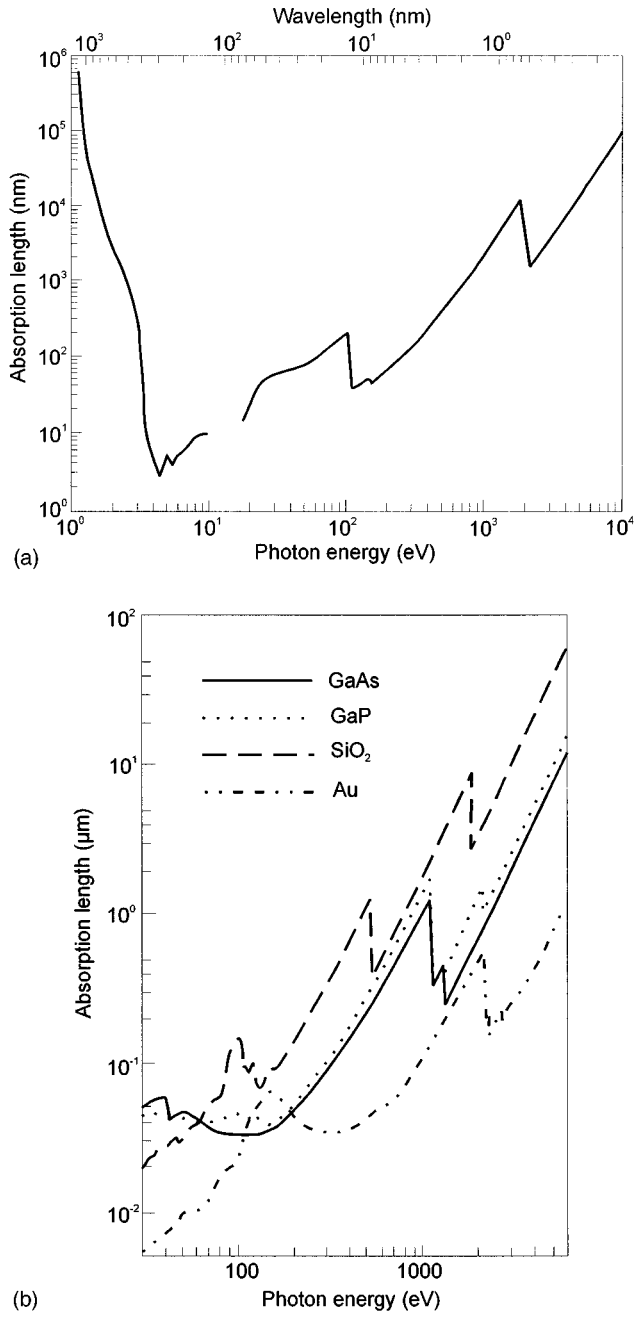

FIG. 15. Absorption lengths of silicon (a) and various materials (b) in the UV spectral region (after Refs. 8 and 56).

mon transfer detector in the spectral range above 250 eV) are shown in Fig. 15(b) for photon energies between 30 eV and 6 keV, corresponding to wavelengths between 40 and 0.2 nm. Especially for photon energies below about 700 eV, a great part of the incident radiation is absorbed in the first several hundred nanometers of a semiconductor detector. Regarding the absorption lengths at higher photon energies, the sensitive depth of a semiconductor detector should be of the order of at least 10 μm to avoid the penetration of photons through this sensitive volume. For high-energy detection, usually the depletion layer is taken as sensitive volume.

Figure 14 shows that different semiconductors cover the UV spectral range. However, the modern semiconductor UV

TABLE III. Johnson (Ref. 60) and Keyes (Ref. 61) figures of merit for electronic devices fabrication in the Si, Ge, GaAs, 6H and 3C SiC, and GaN systems (after Ref. 58).[a]

Material	$Ev_s/2\pi$ (V/s) Johnson	$\sigma_t(cv_s/4\pi\varepsilon)^{1/2}$ (W/deg) Keyes	Breakdown field (V/cm)
Si	2×10^{11}	6.7×10^{7}	4×10^{5}
Ge	1×10^{11}	1.5×10^{7}	2.5×10^{5}
GaAs	7×10^{11}	2.7×10^{7}	5×10^{5}
6H–SiC	1.3×10^{13}	35×10^{7}	4×10^{6}
3C–SiC	1.2×10^{13}	39×10^{7}	3×10^{6}
GaN	1.6×10^{13}	12×10^{7} on GaN $30–40\times10^{7}$ on SiC	4×10^{6}

[a]E_0 breakdown field, v_s saturation electron drift velocity, σ_t thermal conductivity, ε dielectric constant.

detectors are mainly fabricated using Si. Many of the applications for UV detection involve hostile environments such as *in situ* combustion monitoring and satellite-based missile plume detection, where the ruggedness of active UV detector material is an important advantage. Other applications capitalize on the sensitivity of wide band-gap semiconductor detectors, such as air quality monitoring, gas sensing, and personal UV exposure dosimetry. Industries such as the aerospace, automotive, petroleum, and others have continuously provided the impetus pushing the development of fringe technologies which are tolerant of increasingly high temperatures and hostile environments. In the field of optical devices, several trends are pushing research into new materials. Considering the relatively advanced stage of SiC development, it appears that most high-temperature, high-power electronic devices will be fabricated from that material. The wide band-gap energy also permits fabrication of SiC UV detectors. A technological progress in fabrication of materials based on the III–V nitrides together with their inherent favorable properties, make III–V nitrides the most promising semiconductor materials for application in the UV wavelength range.[57–59] III–V nitride devices will be capable of improved high power and temperature operation due to their large band gaps.

GaN has many advantages over SiC for applications, but lags in development. While its thermal conductivity, thermal stability, chemical inertness, breakdown fields, and band gap are all roughly comparable to SiC, its optoelectronic properties will be superior. GaN has a direct band gap, so momentum-conserving transitions connect states having the same k values. Therefore, GaN is one of the most promising materials for light-emitting devices in the blue, violet, and ultraviolet spectral regions. Table III compares SiC and GaN to the conventional semiconductors for power electronic applications. The Johnson[60] and Keyes[61] figure of merit provides an estimate of the suitability of a material for power electronics. Because of the wide band gap of GaN (E_g=3.4 eV) there is no responsivity to infrared radiation (long wavelength cutoff occurs at 365 nm) which is important in many applications whenever it is desirable to detect UV in a visible and infrared background. It should be expected that GaN radiation resistance is superior to SiC. Initial results indicate that ohmic contacts to GaN will be superior to those possible with SiC. Finally, the ease with which heterostructures can

TABLE IV. Comparison of important semiconductor properties for high-temperature electronics (after Refs. 57 and 58).

Parameter	Si	GaAs	GaP	3C–SiC (6H–SiC)	GaN	Diamond
Lattice parameters (Å)	$a=5.4301$	$a=5.6533$		$a=4.36$ ($a=3.08$) ($c=15.12$)	$a=3.189$ $c=5.185$	
Band gap (eV) at 300 K	1.1	1.4	2.3	2.2 (2.9)	3.39	5.5
Coefficient of thermal expansion (10^4 K^{-1})	3.59	6.0		(4.2) (4.68)	5.59 3.17	
Maximum operating temperature (K)	600?	760?	1250?	1200 (1580)		1400?
Melting point (K)	1690	1510	1740	Sublimes >2100		Phase changes
Physical stability	Good	Fair	Fair	Excellent	Good	Very good
Electron mobility (cm^2/V s) at 300 K	1400	8500	350	1000 (600)	900	2200
Hole mobility (cm^2/V s) at 300 K	600	400	100	40	150?	1600
Breakdown voltage (10^6 V/cm)	0.3	0.4	⋯	4	5?	10
Thermal conductivity (W/cm)	1.5	0.5	0.8	5	1.3	20
Saturation electron drift velocity (10^7 cm/s)	1	2	⋯	2	2.7	2
Static dielectric constant	11.8	12.8	11.1	9.7	9	5.5

be formed with AlN and lnN alloys is a great advantage for more complex device structures.

The wurtzite polytypes of GaN, AlN, and lnN form continuous alloy systems whose direct band gaps range from 1.9 eV for InN, to 3.4 eV for GaN, to 6.2 eV for AlN. Thus, the III–V nitrides could potentially be fabricated into optical devices which are active at wavelengths ranging from the red well into the UV. Table IV compares relevant material properties of SiC and GaN with Si and GaAs, the two most popular semiconductor device technologies, and GaP and diamond, two other contenders for high-temperature operations. Diamond has long been recognized as a promising material for fabricating robust, solar-blind radiation detectors. However, due to technological limitation, diamond is still potential material for future technologies.[13,62] The device maximum operating temperature parameter given in Table IV is calculated as the temperature at which the intrinsic carrier concentration equals 5×10^{15} cm^{-3} and is intended as a rough estimate of the band gap limitation on device operation. More important for the maximum operating temperature is the physical stability of the material.

IV. Si ULTRAVIOLET DETECTORS

Silicon photodiodes, originally designed for the visible spectral range, can be also used in the UV region. Arrays of silicon photodiodes are fabricated by a number of manufacturers, e.g., the most commonly used arrays for astronomical spectroscopy are fabricated by EG and Reticon.[63] Building a silicon photodiode with a high ultraviolet quantum efficiency has not been the problem. The problem has been to maintain that high quantum efficiency under ultraviolet irradiation and over a period of years.

Two types of silicon UV detectors are fabricated:

(1) diffused photodiode,
(2) Schottky barrier photodiode.

In the diffusion photodiode a depletion layer is formed between the *p*- and *n*-doped layers, in a Schottky diode it is formed at the semiconductor-metal interface.

A. Diffused photodiodes

Figure 16 shows a typical spectral dependence of quantum efficiency of the older types of silicon photodiodes. The quantum efficiency of this device is considerably lower than the theoretical value between 1400 and 2000 Å. Addition-

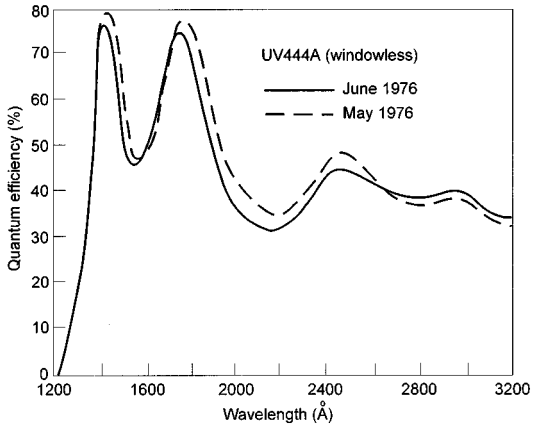

FIG. 16. Quantum efficiency of older design silicon photodiode (after Ref. 64).

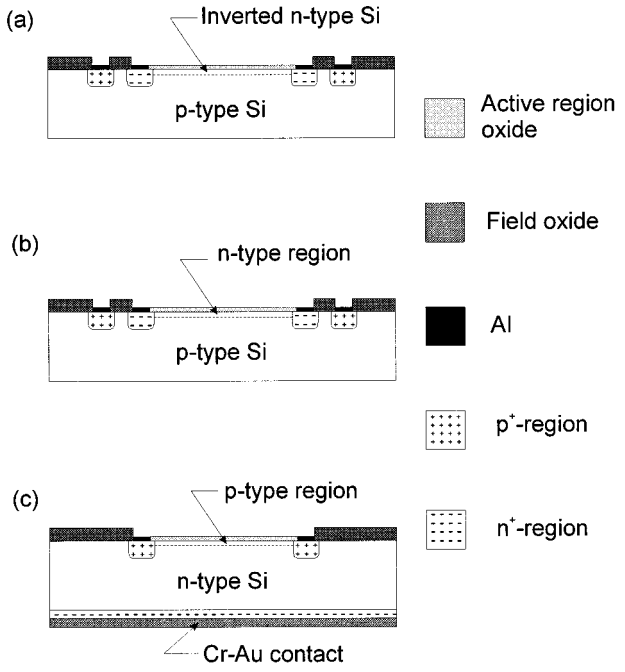

FIG. 17. Schematic diagram of the silicon UV photodiodes: (a) inversion layer type; (b) phosphorus diffused type (n on p); and (c) boron-diffused type (p on n) (after Ref. 67).

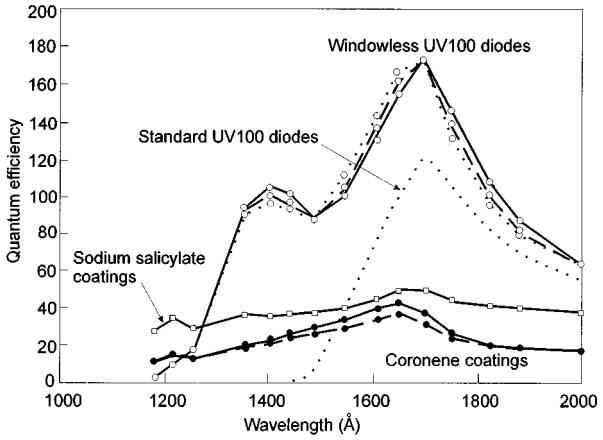

FIG. 18. Quantum efficiency of inversion layer silicon photodiodes (UDT standard UV 100 photodiodes) compared to the efficiency of typical fluorescing coatings (after Ref. 64).

ally, this photodiode is almost dead to UV photons of wavelengths shorter than 1200 Å, presumably because of a thick anti-reflecting silicon dioxide layer on the front surface. The majority of the oldest types of silicon photodiodes had a dead region at their surface, so carriers generated by UV photons were lost in this region before they could be collected by the p-n junction, leading to a loss of quantum efficiency. The susceptibility of the oxide–silicon interface to high levels of UV radiation has been known about at least since 1966.[65] Even if a photodiode had 100% internal quantum efficiency, a thick silicon dioxide layer on the diode surface would reduce the quantum efficiency in the 400 to 1200 Å region drastically.

To overcome the above-mentioned difficulties, it has been proposed and demonstrated that natural inversion layer photodiodes[66] should have an internal short-wavelength quantum efficiency of 100% due to the nature of the built-in field associated with a strongly inverted layer at the oxide–silicon interface. Figure 17(a) shows a schematic diagram of this photodiode. The inversion layer is contacted via the n^+ diffusion by means of the inner metal ring. The outer metal ring contacts the p^+ guarding and thereby the p substrate. The substrate can also be connected via the p^+ diffusion on the backside. Hansen[66] has fabricated the photodiodes on 100 Ω cm substrates, which corresponds to an acceptor concentration of 1.4×10^{17} cm^{-3}. The substrates were oriented along the ⟨111⟩-direction. The oxide, which also serves as an anti-reflection layer, was grown in dry oxygen. The intrinsic fixed positive charge within the SiO_2 causes the p-type substrate to undergo inversion, and thus induces a very thin n-type region adjacent to the SiO_2Si interface, and forms the required p-n junction. Such devices have an oxide n^+ p structure and are available commercially, e.g., UDT-UV50.[68]

Since the junction creation process results in a built-in field which is optimum for removing minority carriers from the oxide–silicon interface, these devices are less prone to recombination and trapping effects, and thus higher UV quantum efficiency can be achieved than in the case of diffused junction photodiodes.

Figure 18 shows spectral dependence of quantum efficiency of UDT standard UV 100 inversion layer photodiodes which had 1200 Å anti-reflection layers of oxide. The absence of any dead region at the front surface of these diodes has been verified by internal quantum efficiency measurements in the 250–500 nm spectral range. These diodes are also almost dead below 1200 Å because of the thick silicon oxide anti-reflecting coating on the front surface. Because the inversion layer charge which causes the semiconductors surface inversion is situated within the first 100 Å of silicon oxide from the semiconductor surface, any efforts to extend the diodes response below 1200 Å by reducing the silicon oxide coating to a few tens of angstroms is undesirable.

Instabilities were also encountered with this type of photodiode. Inversion layer diodes have a low linearity range (the range over which the diode current is proportional to input irradiance) due to the inherently high sheet resistance of an inverted semiconductor layer. Moreover, it appears that the fixed oxide charge that induces the inversion layer in the diode was neutralized as a result of UV irradiation.[67] Since the inversion layer charge decreases with decreasing oxide charge, the diode inversion layer resistance, which is in series with the diode, would increase. Thus the threshold value of forward bias needed to cause a nonlinearity could be dropped across the increased series resistance by a small value of photocurrent, resulting in a loss of linearity range.

The best quality Si photodiodes for UV applications have been developed by Korde and co-workers.[64,67,69,70] They used different methods of junction fabrication, but the better results have been obtained using defect-free arsenic[69] and phosphorus[67,70] diffusions.

Figure 17(b) is a schematic diagram of diffused type Si photodiode. The starting material was a float-zone, ⟨111⟩ oriented, p-type, 100 Ω cm, one side mirror polished, silicon

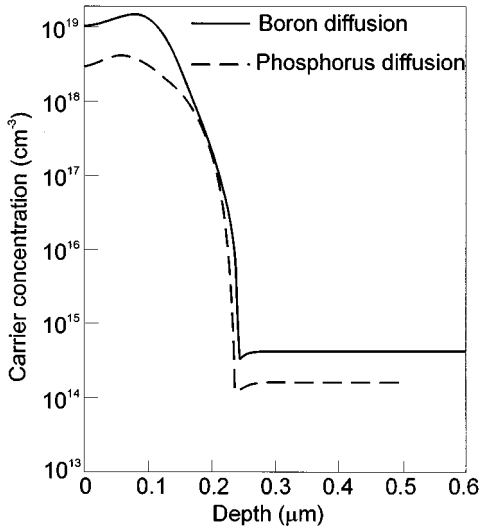

FIG. 19. Carrier concentration profiles of boron diffusion in p-on-n photodiodes, and of phosphorus diffusion in n-on-p photodiode (after Ref. 67).

wafer having 1 cm^2 active area. After the p^+ channel stop and n^+ guard ring were formed by selective boron and phosphorus diffusions, respectively, arsenic was predeposited in the active area of the device using a planar arsenic source. The arsenosilicate glass formed during the predeposition was etched in 10% hydrofluoric acid and the final passivating Si_2O anti-reflection coating with a thickness of about 600 Å was grown in dry oxygen. A standard photolithographic process was used to open windows at the desired locations in the diffused regions, and aluminum was vacuum evaporated on these windows for ohmic contacts.

Since UV radiation is absorbed in the first few hundred nanometers of silicon, the doped diffusions were kept shallow to minimize the possibility of recombination between the oxide–silicon interface and the junction. Low-temperature dopant deposition and drive in were adopted to get a shallow junction, about 0.2 μm. The carrier concentration profiles of diffused photodiodes are shown in Fig. 19.

It appears that n-type impurities such as phosphorus and arsenic tend to pile up in the silicon during the oxide growth, creating a built-in electric field near the oxide–silicon interface, which eliminates interface recombination.[71,72] So a high minority carrier lifetime in the diffused region results in 100% internal quantum efficiency, which is shown in Fig. 20. The increase in internal quantum efficiency below 350 nm is caused by impact ionization involving energetic photogenerated carriers, while the decrease in internal quantum efficiency above 600 nm is caused by the recombination of some of the minority carriers created in the p-type silicon beyond the depletion region.

As possible causes of instability of quantum efficiency of silicon UV photodiodes, we can distinguish:[67] unsatisfactory silicon–oxide interfaces, latent recombination centers in the diffused layers, and moisture absorption by the device. Meticulous care as described in Ref. 67 is necessary during the fabrication of devices. A dry, clean oxide process during the growth of the final anti-reflection coating is essential to achieve stability against UV exposure. According to Korde

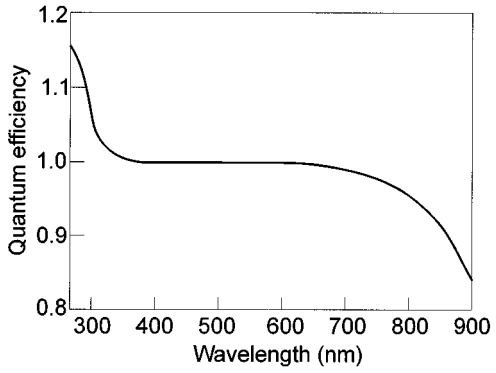

FIG. 20. Internal quantum efficiency as a function of wavelength for phosphorus-diffused photodiode (after Ref. 67).

and Geist the most important steps in obtaining a UV-enhanced photodiode are:[67]

(1) extremely high-purity chemicals for wafer cleaning,
(2) a clean oxide process, such as described by Botchek,[73]
(3) special annealing procedure[74] to prevent UV-induced charge neutralization in the oxide, as well as to render the oxide–silicon interface less susceptible to UV radiation,
(4) careful procedure of deposition of ohmic contacts (by electron-beam evaporation).

N on p photodiodes are inherently more stable than the commonly used boron-diffused devices based on n-type silicon. Boron migrates from the silicon surface into the oxide during the final thermal oxidation step. The resulting acceptor profile, which is depleted in the vicinity of the oxide–silicon interface, creates a built-in electric field perpendicular to the interface, directed toward the bulk. The resulting electric field attracts the photogenerated minority carriers (electrons) created in the diffused region towards the oxide–silicon interface, greatly enhancing the carrier loss due to interface recombination. The results of a long-term stability test (baking for several months at 110 °C) shown in Fig. 21

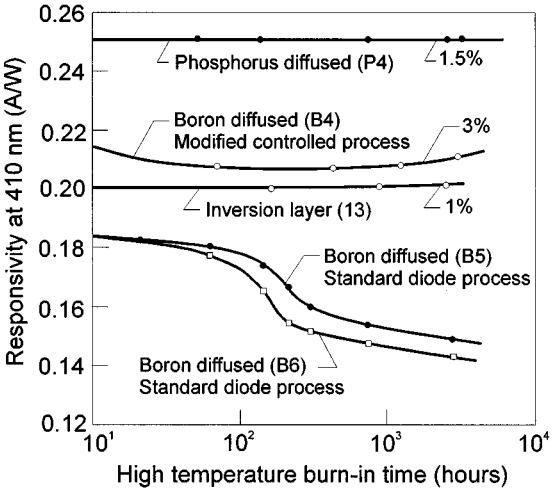

FIG. 21. Change in spectral responsivity at 400 nm as a function of duration of exposure to 110 °C (after Ref. 67).

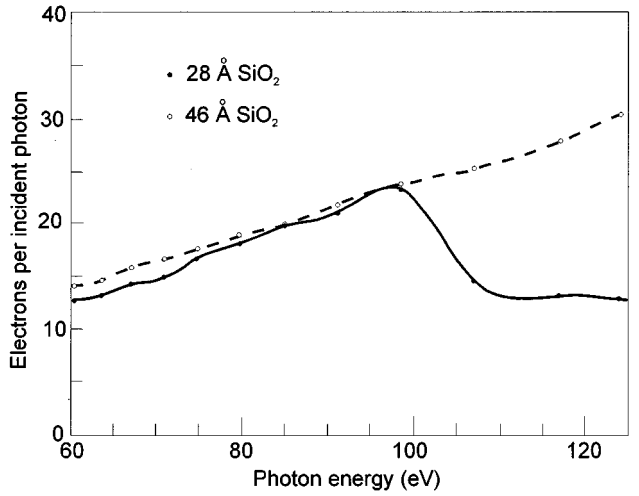

FIG. 22. Measured quantum efficiency of Si photodiodes with 46 and 28 Å of oxide (after Ref. 70).

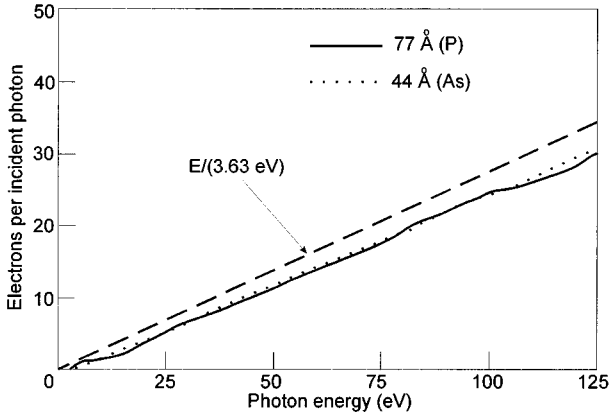

FIG. 23. Quantum efficiency of As- and P-doped photodiodes with oxide thickness as indicated. The straight line represents the quantum efficiency of Si based on a value of 3.63 eV per electron-hole pair, not including reflection losses (after Ref. 70).

indicate little or no change in responsivity of the phosphorous diffused and inversion layer devices, while the boron-diffused devices fabricated using the standard process exhibited a monotonic decrease in responsivity during the prolonged baking.

Further improvement in the fabrication of Si UV photodiodes has been achieved by reduction of the silicon dioxide layer to a thickness between 40 and 80 Å.[64,70] The thinner oxide should lead to photodiodes with higher quantum efficiency stability because of the smaller volume available for generation of electron-hole traps which are invariably caused by the diode exposure to humidity and UV radiation. Production of the electron-hole traps in the passivating silicon dioxide layer is one of the major causes for quantum efficiency changes in silicon photodiodes. Figure 22 shows considerable improvement of quantum efficiency in a short wavelength region for photodiodes with 46 Å of oxide layer. Reduction of the oxide thickness is limited by a critical thickness below which device behavior is unacceptable.[70] The performance of the 28 Å sample is seriously degraded. Not only is the efficiency of the 28 Å sample reduced, but its exposure stability is quite poor.

Improvements in the performance of Si UV photodiodes still require improved oxide formation techniques. Novel Si UV photodetector structures are continuously designed and fabricated.[75,76] Also the amorphous Si UV p-i-n photodiodes have been fabricated successfully.[77,78] Enhancement UV response of amorphous SiC/Si heterojunctions in the 200–400 nm wavelength region has been achieved by using high optical gap a-SiC:H as the front layer, by the reduction of the front-layer thickness, and by using low-level phosphorus doping in the i-a-Si:H layer.[78]

B. Si photodiodes for vacuum ultraviolet applications

Detectors for the vacuum ultraviolet (VUV) region must usually be operated in a clean, ultrahigh vacuum environment, and must be free from interactive degradation in the presence of radiation. Further, they should possess a low background noise level to assist in the detection of a relatively weak source. Si photodiodes for VUV technology are typically made with a very thin passivating silicon dioxide surface layer, as described previously.

The mean energy, w, required for electron-hole pair creation depends on the band gap of a semiconductor.[79] For example, experimental values for w are 3.61 for Si,[80] 4.2 for GaAs,[80] and 6.54 for GaP.[81] If these pairs are created in the depletion layer or if they diffuse into the space-charge region, they are separated by the internal electric field giving rise to an external photocurrent. Figure 23 shows that the quantum efficiency of Si photodiodes nearly approaches the predicted slope of 3.63 eV per electron hole created. These types of photodiodes can also be optimized for the soft x-ray region.[82]

One significant shortcoming of Si photodiodes for certain VUV applications is the inherent broadband response extending from x rays to the near infrared. This broadband characteristic is often undesirable in many applications. The addition of a thin film of a suitable filtering material to the source of such a photodiode can accomplish the restriction of the sensitivity of the silicon to a much narrower band, or bands, in the VUV.[83]

A schematic of the optically filtered photodiode is shown in Fig. 24. The photodiodes were fabricated on 100-nm-diam p silicon wafers that have a p-type epitaxial layer about 5 μm thick. Before the active area formation, a deep p-n junction, a p^+ channel stop, and an n^+ guard ring were created by diffusion. The purpose of the side junction is to improve the degree of discrimination against unfiltered radiation by isolating carriers resulting from radiation entering the sides of the structure from the main detection circuit. The active area of 1 cm^2 was produced by phosphorous/arsenic doping, followed by the thermal growth of a 15-nm-passivating surface oxide layer. The front surface of the photodiode was coated with the filter materials. Useful bandpasses in the VUV were selected: Al/C, Al/C/Sc, Ti, Sn, and Ag. The filters have bandpasses ranging from 10 to 50 nm and are commonly used in the region 0.1–80 nm.

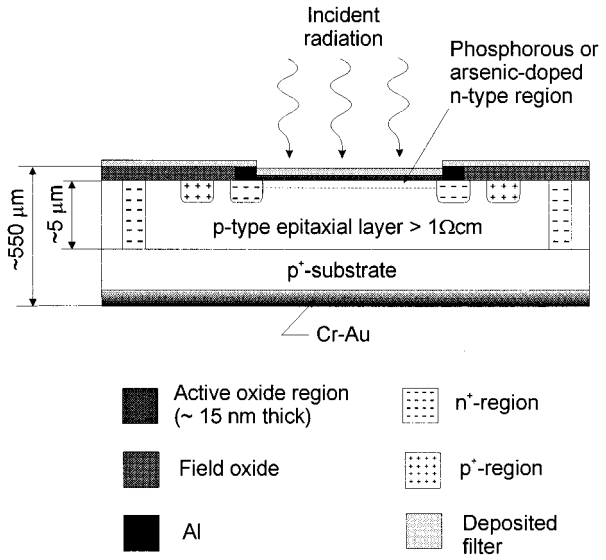

FIG. 24. Schematic of optically filtered VUV photodiode (after Ref. 83).

The spectral efficiency of the coated photodiodes is shown in Fig. 25. Also shown are the calculated photodiode efficiencies based on the conversion efficiency of silicon and the transmittance of the thin-film coatings, including the 15-nm-thick passivating silicon oxide layer. It can be seen that there is reasonable agreement between the resulting calculated values and the measured device efficiencies. Typical dark current values measured before and after coatings were about 100 fA. Noise variations of this current were about an order of magnitude less.

The photodiodes coated with appropriate filtering materials may find applications in diverse VUV and EUV disciplines, such as plasma diagnostics, solar physics, x-ray lithography, x-ray microscopy, and materials science, and can reduce the dependence on relatively fragile unsupported metallic filters for spectral discrimination.

V. SCHOTTKY BARRIER ULTRAVIOLET PHOTODIODES

In a Schottky barrier photodiode, a thin metal layer is deposited onto a semiconductor. The transmission through the thin metal contact is relatively high, and thus a large fraction of the UV radiation is absorbed close to the metal/semiconductor interface where photogenerated carriers are efficiently collected by the depletion layer field. This gives the device an acceptable quantum efficiency, albeit lower than for the best photodiodes. Usually at shorter wavelengths the collection efficiency of the generated carriers decreases for Schottky barriers. The responsivity also decreases.[84]

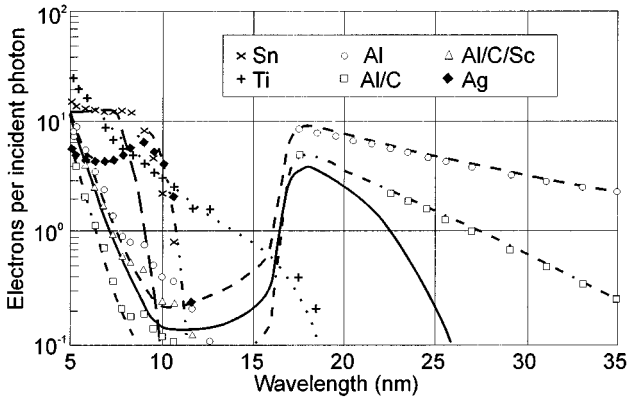

FIG. 25. Measured (points) and calculated (curves) efficiencies of silicon photodiodes coated with several VUV filtering materials (after Ref. 83).

For many applications Schottky barrier photodiodes are superior to other detectors. They are particularly promising as calibrated standard detectors, because they are relatively insensitive to surface contaminations, show a higher stability in intense UV radiation, and posses a quantum efficiency up to four orders of magnitude higher than that of photoemissive detectors in the VUV spectral range.

Schottky barrier UV detectors have been fabricated using different semiconductors.[85–91] A straightforward way to make a highly selective (blindless) UV detector is to use a wide band-gap semiconductor, e.g., ZnO[86] or diamond.[90,91] Semiconductor diamond is of considerable interest from a basic physics, as well as an engineering, point of view. The high thermal conductivity, small dielectric constant ($\varepsilon \approx 5.5$), and large band-gap energy ($E_g = 5.4$ eV) combine to make diamond an ideal candidate for many electronic and optoelectronic applications, particularly for high-temperature operation. Unfortunately, these wide band-gap materials of a good enough quality are not readily available, and the appropriate technology is far from being mature. However, recent progress in diamond thin-film technology is very promising for future applications.

Recently Zhao *et al.*[91] have reported photoresponse characteristics of boron doped hot-filament chemical vapor deposition (HF-CVD) diamond based Schottky diodes using semitransparent Al contacts. The polycrystalline 7-8-μm-thick diamond films were deposited on p-type (100) silicon substrates using hydrogen and methane as the reaction gases and acetone vapor as the carrier gas for the boron dopant (trimethyl borate). The acetone was also an additional carbon source. After surface chemical cleaning of samples, the circular Schottky contacts (with an area of 4.5 mm^2) were fabricated by thermal evaporation of semitransparent aluminum contacts. However, these Schottky diodes were not solar-blind detectors. Figure 26 shows the spectral dependence of the quantum efficiency of the photodiode. The photoresponse of these diodes to visible and near UV radiation is attributed to several mechanisms including photoelectronic emission between metal and semiconductor, extrinsic photoexcitation of impurities, as well as crystal defects. Without correction for surface reflection, the quantum efficiencies were between 5% and 10% for unbiased diodes. When a reverse bias of over 1 V was applied, the quantum efficiency of 30% was obtained at 500 nm. The increase of quantum efficiency is caused by a broadening of the junction depletion region and more efficient collection of photocarriers. The Schottky barrier height between Al and p-type polycrystalline diamond was determined to be 1.15 eV. It appears that the barrier height of HF-CVD diamond Schottky diodes is controlled by a high density of defect states, and hence is independent of the metal work function. The Schottky barrier is pinned ap-

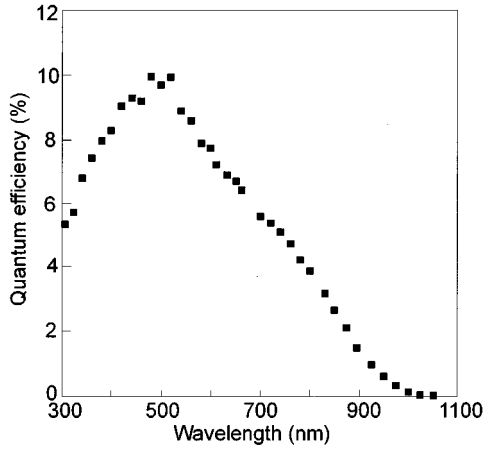

FIG. 26. Quantum efficiency vs wavelength for AJ-HFCVD diamond Schottky diodes without the correction of reflection (after Ref. 91).

proximately 0.2 E_g from the top of the valence band. The origin of the pinning has not been identified, but is likely to be due to damage introduced during growth.[92]

The conventional method to make a selective UV detector is to combine a conventional broadband UV-enhanced photodiode with a UV filter. An example of this kind of combination is a Ag–GaAs Schottky photodiode with a thin silver contact.[85] The UV selectivity of this detector is a result of the narrow transmission ''window'' of silver films near the wavelength of 322 nm. A disadvantage of this approach is a deterioration of the responsivity also in the UV region.

Schottky barrier photodiodes have been mainly fabricated for VUV applications. Investigations carried out by Krumrey *et al.*[87,88] indicate that GaAsP and GaP Schottky photodiodes show remarkable stability and high quantum efficiency. The stability measurements of the efficiency were conducted with a monochromatic photon flux of $\sim 10^{10}$ photons/s into an area of 1 mm^2 at a photon energy of 124 eV. Typical behavior of a silicon and GaAsP Schottky photodiode is shown in Fig. 27. In the case of silicon photodiode, the quantum efficiency decreases from the initial value of 27% by 0.25%/s. The decrease of efficiency shows saturation behavior, but even at 8% a further decrease of the order of 0.01% is observed. In contradiction, the quantum efficiency of GaAsP and GaP Schottky diodes (Hamamatsu G1127-02 and G1963) is stable at least within 0.05% (which is the uncertainty of the measurement) during an exposure of more than 1 h. The electrical and optical properties of GaAsP Schottky diodes in the spectral range below 6 eV have been investigated in detail by Wilson and Lyall.[89] The GaAsP photodiodes can be used in the hole spectral region from 2 eV up to at least 3.5 keV (Fig. 28). Near the visible region the efficiency is comparable to that of photoemissive diodes, but it is higher by three to four orders of magnitude in the region above 1 keV.

VI. SiC ULTRAVIOLET DETECTORS

The inherent material properties of the 6H polytype of SiC are very attractive for UV applications. In comparison with Si (see Table IV), SiC is characterized by a higher

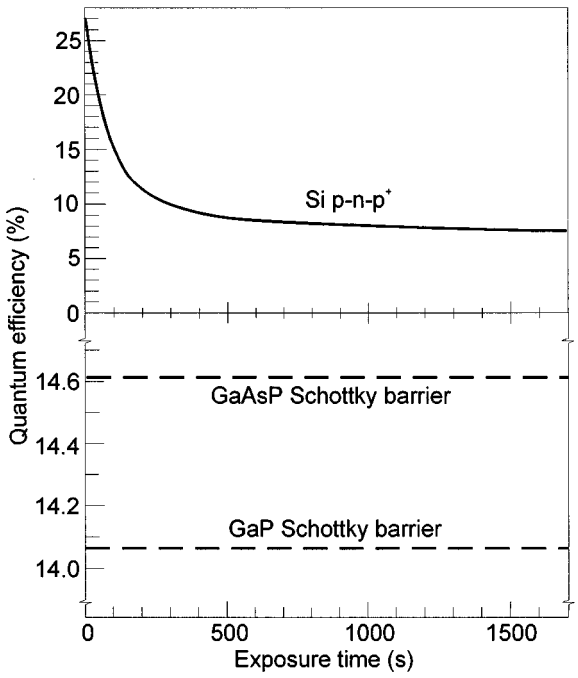

FIG. 27. Stability of three different semiconductor photodiodes when irradiated with 10^{10} photons/(s mm^2) at 124 eV (after Ref. 87).

breakdown field that permits much smaller drift regions (i.e., much lower drift region resistances), a higher thermal conductivity that enables superior heat dissipation, and a wide band-gap energy (2.9 eV) that permits higher junction operating temperature. Due to the fact that reproducible silicon carbide wafers and epilayers were unavailable before 1989. SiC carbide device fabrication technology is relatively immature compared to silicon device fabrication technology.

A. *P-n* junction photodiodes

The earlier published research on 6H–SiC UV photodiodes utilized diffusion of Al into *n*-type substrates.[93] The diffusion process at temperatures of about 2000 °C led to a

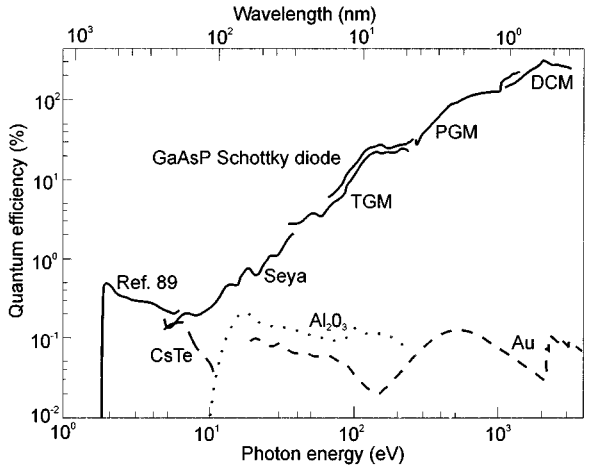

FIG. 28. Quantum efficiency of a GaAsP Schottky diode, determined on different monochromators by comparison with photoemissive detectors. The quantum efficiency of the photoemissive reference diodes are also shown (after Ref. 87).

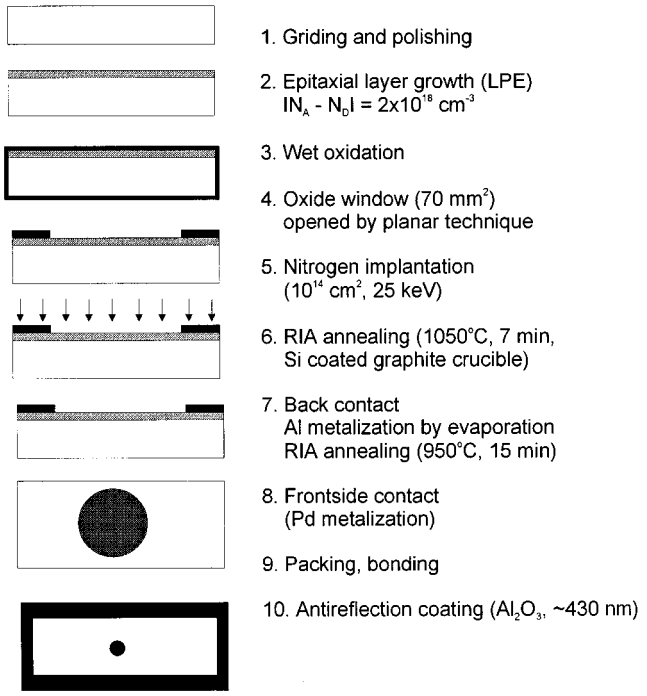

FIG. 29. SiC UV photodiode processing steps (after Ref. 94).

structural decomposition of surface layers. This process resulted in high-leakage devices with low quantum efficiency.

Glassow *et al.*[94] improved upon this initial design by utilizing N implantation to form a very shallow (0.05 μm) n^+-p junction in a 5-μm-p-type epitaxial layer grown on a p-type substrate. The successive steps of the manufacturing process of a planar photodiode are shown in Fig. 29. Furnace annealing and rapid isothermal annealing (RIA) were employed to activate the implanted nitrogen. $I-V$ characteristics and spectral quantum efficiency were investigated in the temperature range from 296 to 826 K and 295 to 676 K, respectively. This study resulted in devices with a maximum quantum efficiency of 75% (with an anti-reflection coating) at a peak wavelength of 280 nm at room temperature. The scatter of the maximum value of the quantum efficiency was explained by differing surface recombination velocities which were caused by differing surface qualities. The reverse-bias dark-current density was excessive, on the order of 10^{-5} A/cm^2 at -10 V and room temperature. Probably, contact sintering at high temperatures could induce diffusion of the contact metal through crystalline defects in thin n^+ layer and thereby increase diode leakage current.

Figure 30 shows a mesa SiC photodiode structure fabricated from commercial 6H–SiC wafers, 1 in. in diameter, on which a p-n junction was grown epitaxially.[95] A heavily N-doped n-type epitaxial layer of 0.2 or 0.3 μm thick was utilized to form an n^+-p junction. The concentrations of impurities was $5–8\times10^{17}$ cm^{-3} in p-type epitaxial layers, and $5–10\times10^{18}$ cm^{-3} in n^+ cap layer. The device mesa was patterned and etched using reactive ion etching (RIE) and an NF_2O_2 gas mixture. Device passivation was accomplished by growing a thin (0.05 μm) layer of SiO_2. The contact to the top n^+ layer was Ni sintered in Ar at temperatures between 900 and 1000 °C. Optical responsivity with a peak at about

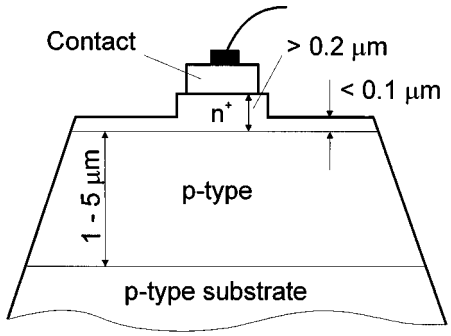

FIG. 30. SiC photodiode cross section (after Ref. 95).

270 nm between 150 and 175 mA/W with a quantum efficiency of about 70%–85% was measured. As the detection wavelength is decreased, a larger proportion of the absorption occurs near the semiconductor surface and surface recombination becomes more important. By thinning the top n^+ layer outside of the mesa contact (see Fig. 30), a responsivity of 50 mA/W was achieved at 200 nm. The diffusion length of electrons in the p-type layer was varied between 1.4 and 2.2 μm, and was smaller than the estimate of 3 μm given in Ref. 94. This diffusion length determination does not depend on any assumptions about carrier lifetime and mobility as was made by Glassow *et al.*[94]

Edmond and co-workers[96] have demonstrated a considerable improvement of 6H–SiC UV photodiode quality over previous efforts.[93–95] Wafers of n- and p-type 6H–SiC having a diameter of 25.4 mm with typical resistivities in the range of 0.02–0.04 and 1–10 Ω cm, respectively, were used as substrates for epitaxial growth. An epitaxial junction was produced by first growing a predominantly Al-doped p-type layer followed by a predominantly N-doped n-type layer on a p-type substrate. The doping in the background layer was controlled between $(1–5)\times10^{16}$ cm^{-3} with a thickness of ~3 μm. The n-type layer was heavily doped to $\sim10^{19}$ cm^{-3}. All devices were fabricated using a mesa geometry. The junctions were passivated with thermally grown SiO_2. Ohmic contact materials for the p-type side and n-type side were sintered Al and Ni, respectively.

Figure 31(a) shows the reverse-bias dark current versus voltage as a function of temperature for a UV photodiode with square active junction with an area of 0.04 cm^2. The photodiode has demonstrated extremely small dark currents, as little as 10^{-11} A at -1 V at 473 K. At the highest voltage measured, -10 V, the dark current density increased from $\sim10^{-9}$ to $\sim3\times10^{-8}$ A/cm^2 when increasing the temperatures from 473 to 623 K. Figure 31(b) shows the dark current density at -10 V as a function of temperature together with previously reported data for comparison purposes. As shown, the devices reported by Edmond and co-workers[96] exhibit orders of magnitude lower leakage current than any other published data in 6H–SiC. The forward $I-V$ characteristics correspond to the β values ranging from 1.5 to 2 which indicate both diffusion and generation–recombination processes.

The same devices exhibited near unity peak responsivities between 268 and 299 nm in temperature range between

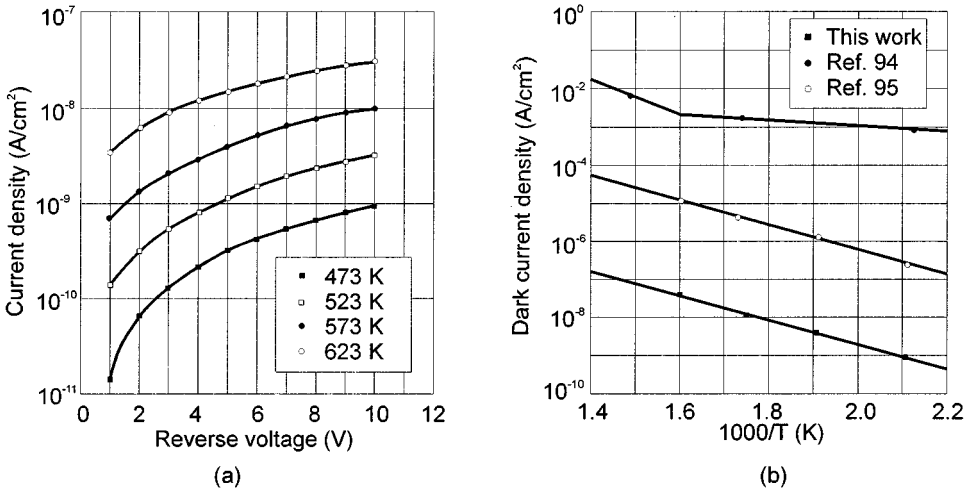

FIG. 31. Dark current density vs (a) reverse voltage and (b) inverse temperature for 6H–SiC photodiodes (after Ref. 96).

223 and 623 K (see Fig. 32). The responsivity of the photodiode at a higher temperature shifts to longer wavelengths because of band gap narrowing. The indirect band gap decreases from ~3.03 eV at 223 K to ~2.88 eV at 623 K, corresponding to a rate of 3.8×10^{-4} eV/K.[94]

Recently, Hirabayashi *et al.*[97] have fabricated *p-n* junction 3C–SiC photodiodes by atmospheric chemical vapor deposition. However, these photodiodes were inferior in comparison with those previously described. The maximum value of responsivity was 72 mA/W at 250 nm and the quantum efficiency was 36% (cubic SiC energy gap is 2.2 eV at room temperature).

Finally, it should be noticed that to produce large area and low-cost UV detectors an innovative family of devices fabricated of hydrogenated amorphous SiC/Si heterojunctions have been described.[98,99]

B. Schottky barrier photodiodes

Schottky barrier 6H–SiC photodiodes are of interest for many applications because of their relatively simple fabrication process compared to *p-n* photodiodes. Frojdh *et al.*[100,101] have fabricated finger shaped Schottky photodiodes by evaporating Ti on substrates with different *n*-type and *p*-type doping levels. The starting material was 6H–SiC wafers with an epitaxial layer. The doping of the epitaxial layers is specified in Table V. Prior to processing the wafers were degreased by subsequent dipping in trichloroethylene, acetone, and 2-propanol and finally dipped in hydrogen fluoride (HF). Next, a pattern with a number of shaped openings was formed on the wafer with finger widths in the range 1–2 μm. Each diode is surrounded by an opening with a width of 10 μm (see Fig. 33.) Four different photodiode areas were used: 100×100 μm, 75×75 μm, 50×50 μm, and 25×25 μm.

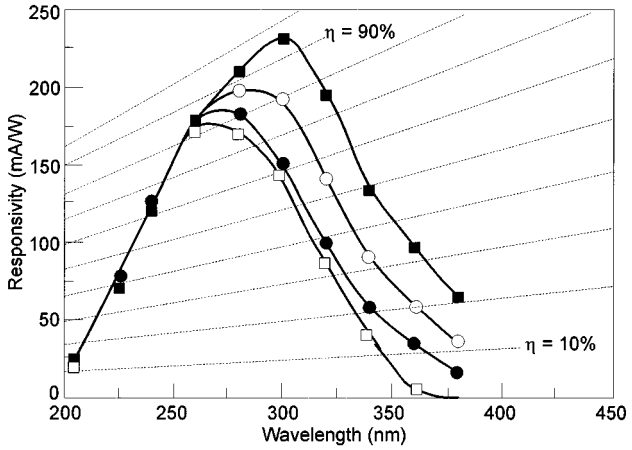

FIG. 32. Temperature-dependent responsivity of a SiC photodiode. The temperatures tested were: (□) 223 K. (♦) 300 K, (○) 498 K, and (■) 623 K (after Ref. 96).

As a barrier, titanium with resulting layer thickness 200 nm was evaporated on the wafers using an electron gun evaporator. A standard lift-off procedure was used to remove excess metal. A back contact was made by evaporation of 500 nm of Al on the backside of the wafer (see Fig. 34.)

Most of the Schottky barriers showed good rectifying behavior with an ideality factor generally below 1.2. The best results were obtained for diodes on the *p*-type material for which the reverse leakage current at −10 V was below 1 pA and for a reverse voltage of up to −70 V the leakage current remained below 500 pA. Also, results of spectral responsivity measurements indicate that the *p*-type material has the highest sensitivity (see Fig. 33). Sample N1 shows very low responsivity which can be explained by the shallow epitaxial layer. The low response at short wavelengths can be explained by the influence of surface recombination.

Generally, the *p*-type material shows a much higher photoresponse than the *n*-type material. This can be explained by two effects:

(1) the built-in voltage in the *p*-type material is much higher (about factor of 2) than the built-in voltage in the *n*-type material,
(2) the diffusion length for electrons is much larger than the diffusion length for holes.

TABLE V. Characteristics of 6H–SiC Schottky barrier photodiodes fabricated with different materials (after Ref. 100).

Sample	Sample characterization	N_d, N_a (cm^{-3})	Φ_b (eV) $C-V$	Φ_b (eV) $I-V$	β	I_{rev} at -10 V
N1	n-type, $t=1.6$ μm, no visible defects	7.5×10^{15}	0.98	0.97	1.08	<10 pA
N2	n-type, $t\approx10$ μm	2.9×10^{16}	0.89	0.92	1.14	0.4 nA
N3	n-type, $t\approx5$ μm	2.7×10^{12}	0.94	0.79	1.23	0.5 mA
N4	n-type, $t\approx5$ μm, high density of pinholes	1.0×10^{17}	0.94	0.84	1.17	18 μA
P1	p-type, $t\approx10$ μm	1.6×10^{15}	2.43	1.94	1.03	<1 pA

The second reason also explains the larger photoresponse of p-type material at long wavelengths (see Fig. 35).

The better results for n-type 6H–SiC Schottky barriers have been obtained by Anikin *et al.*[102] The Au–SiC Schottky barriers were formed on the surface of n-type epitaxial layers with uncompensated donor concentration $(5–10)\times10^{16}$ cm^{-3}, grown by an open sublimation method on n-type 6H–SiC substrates oriented along the (0001) Si plane. Front semitransparent contacts were made by vacuum deposition of a thin Au layer. Before evaporation of the barrier contact a crystal of SiC was etched in molten KOH, washed in deionized water and in organic solvents, and finally annealing in a vacuum at 500 °C.[103] The height of the potential barrier was 1.4–1.63 eV, depending on the structure. The structures with an area 3×10^{-3} cm^2 showed low leakage currents, $\sim10^{-10}$ A, up to a breakdown voltage of 100–170 V at room temperature, and could be operated up to 573 K where the leakage current rose to $\sim10^{-8}$ A. The monochromatic responsivity in the best samples at wavelength of 215 nm, reached 0.15 A/W, which corresponds to the quantum efficiency of 80%.

It is expected that the best quality 6H–SiC UV detectors should be fabricated using p-n junctions.[104,105] A considerably good progress in fabrication of p-n junction using chemical vapor deposition has been recently observed. The devices displayed excellent rectification characteristics at elevated temperatures as well as avalanche breakdown voltages of 2000 V at room temperature.

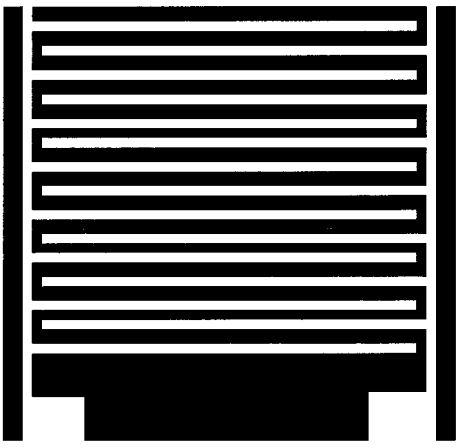

FIG. 33. The finger area of a photodiode.

VII. III–V NITRIDES AS A MATERIALS FOR ULTRAVIOLET DETECTORS

The III–V nitrides are the next group of wide gap semiconductors which are very promising for device applications in the UV wavelengths in much the same manner that their highly successful As-based and P-based cousins have been exploited in the infrared, red, and green wavelengths. Until now, efforts to develop semiconductor device technology in the UV spectral region have been far unsuccessful. The III–V nitrides are excellent materials to cover important technologically band, which occurs in the 240–280 nm range ($\sim$4.75 eV), where absorption by ozone makes the earth's atmosphere nearly opaque. Space communications in this band would be secure from earth, although vulnerable to satellite surveillance. On the earth, shielded by the sun's radiation, imaging arrays operating in this band would provide extremely sensitive surveillance of objects coming up out of the atmosphere. Due to their wide band gap, the III–V nitrides are expected to exhibit superior radiation hardness characteristics compared to Si. GaN is by far the best-studied III–V nitride semiconductor.

The main obstacle in the development of the nitride UV photodetectors was significant difficulties in obtaining high-quality material. GaN has high n-type background carrier concentration resulting from native defects commonly thought to be nitrogen vacancies. In films having relatively small background electron concentrations, p-type doping is difficult to achieve. In the past several years much progress was made in developing modern epitaxial growth techniques and in understanding the properties of this material. The room temperature background electron concentration of GaN films has been considerably reduced and p-type material has

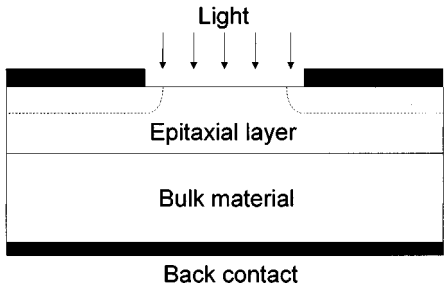

FIG. 34. Cross section of 6H–SiC Schottky barrier photodiode (after Ref. 100).

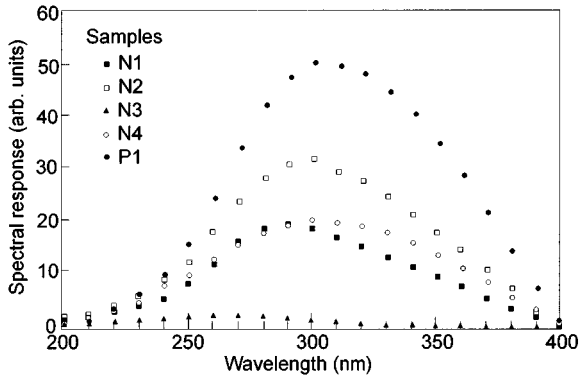

FIG. 35. Spectral responsivity of 6H–SiC Schottky barrier photodiodes (after Ref. 100).

been reported.[106,107] At present the metal-organic chemical vapor deposition (MOCVD) grown GaN layers with the AlN buffer layer have *n*-type conductivity with an electron concentration of about 10^{15} cm^{-3} at room temperature and the electron mobility of about 500 cm^2/V s Mg-doped *p*-type layers have hole concentrations above 10^{12} cm^{-3} and hole mobilities of 10–50 cm^2 V s at room temperature.[108,109]

A number of reviews concerning III–V nitrides have been published. Morkoc *et al.*[57–59,110] and Davis[111] recently published several reviews which present a comprehensive history of the developments in the III–V nitrides, growth techniques, structural, optical, and electrical properties. Also the present-day achievements and future prospects in different devices structures are described.

In this chapter, after a brief review of the physical properties of mainly GaN, we focus on the achievements and future prospects of III–V nitrides as the materials for fabrication of different types of UV detectors.

A. Physical properties

GaN normally crystallizes in the wurtzite crystal structure, although researchers have known for some time that GaN also has a zinc blende polytype. Table VI lists the known properties of wurtzite GaN.

Control of the electrical properties is still one of the greatest challenges facing nitride researchers. Using improved crystal-growth techniques, researchers in several leading laboratories have succeeded in reducing the background electron concentration to 10^{15} cm^{-3}. Nakamura *et al.*[112] have reported the highest GaN bulk electron mobility of 600 and 1500 cm^2/V s at 300 and 77 K, respectively, in an unintentionally doped sample having carrier concentration 4×10^{16} cm^{-3}. Theoretical modeling of Chin *et al.*[113] carried out for $T=77$ and 300 K demonstrates that the carrier concentration dependence of Hall and drift mobilities (important for device modeling) is a significant function of the compensation ratios. These calculated results [see Fig. 36(a)] agree well with available experiments only for high compensation ratio. Piezoelectric acoustic phonon scattering and ionized impurity scattering are the two dominant scattering mechanisms at temperatures $T\leqslant200$ K, and the polar optical phonon scattering is the most significant scattering at temperatures $T\geqslant200$ K. It has also been found that electron mobilities in GaN correlated well with those calculated by Monte Carlo stimulations. Joshii[114] using this method has

TABLE VI. Properties of wurtzite GaN, AlN, and InN (after Ref. 57).

Parameter	GaN	AlN	InN
Band-gap energy (eV)	3.39 (300 K) 3.50 (1.6 K)	6.2 (300 K) 6.28 (5 K)	1.89 (300 K)
Band-gap temperature coefficient (eV/K) (for $T>180$ K)	-6.0×10^{14}		-1.8×10^{-4}
Band-gap pressure coefficient (eV/kbar) ($T=300$ K)	4.2×10^{-3}		
Lattice constant (nm) ($T=300$ K)	$a=0.3189$ $c=0.5185$	$a=0.3112$ $c=0.4982$	$a=0.3548$ $c=0.5760$
Coefficient of thermal expansion (K^{-1}) ($T=300$ K)	$\Delta a/a=5.59\times10^{-6}$ $\Delta c/c=3.17\times10^{-6}$	$\Delta a/a=4.2\times10^{-6}$ $\Delta c/c=5.3\times10^{-6}$	
Thermal conductivity (W/cmK)	1.3	2	
Electron mobility (cm^2/V s) ($T=300$ K)	900		
Hole mobility cm^2/V s ($T=300$ K)	150?		
Index of refraction	2.33 (1 eV) 2.67 (3.38 eV)	2.15	2.85–3.05
Dielectric constant	$\epsilon_0=9.5$ $\epsilon_\infty=5.35$	$\epsilon_0=8.5$ $\epsilon_\infty=4.68$	
Saturation electron drift velocity (10^7 cm/s)	2.7	2	
Electron effective mass	0.20		0.11
Phonon modes (cm^{-1}) ($T=300$ K)	A_1(TO)=532 E_1(TO)=560 E_2=144, 569 A_1(LO)=710 E_1(TO)=741	TO=667 E_2=665 LO=910	TO=478 LO=694

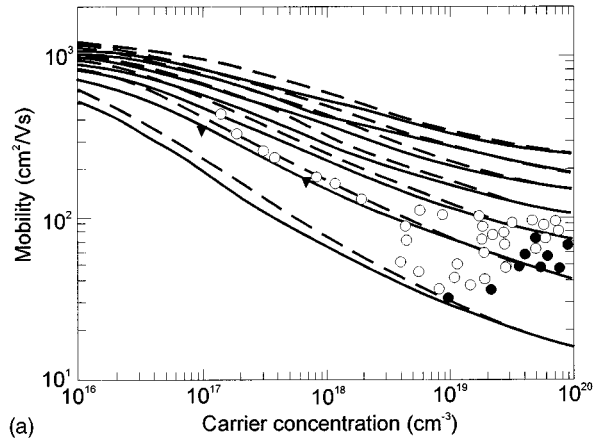

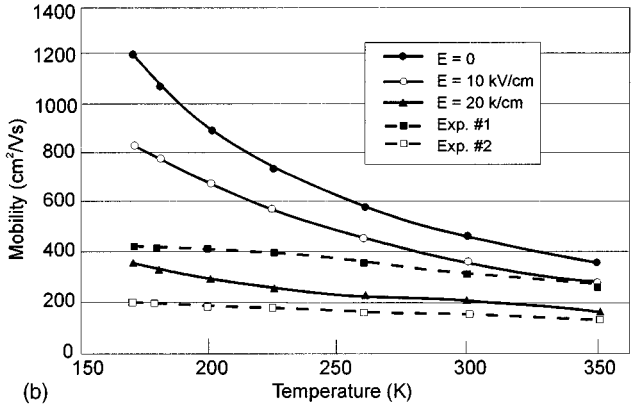

FIG. 36. The electron mobility in GaN: (a) the electron drift (solid curves) and Hall (dashed curves) mobility at 300 K as a function of carrier concentration with compensation ratios 0.00, 0.15, 0.30, 0.45, 0.60, 0.75, and 0.90, the experimental data are taken from different articles (after Ref. 113); (b) comparison of Monte Carlo results with experimental mobility data for bulk *n*-type GaN. Ref. 115. The solid curves were obtained by-using three different internal potential variations (after Ref. 114).

obtained good agreement with experimental data[115] when space-charge scattering was taken into account [see Fig. 36(b)].

One of the long-standing problems in GaN research has been the search for a shallow *p*-type dopant. Most potential dopants have been observed to compensate GaN, producing highly resistive material. *P*-type conduction in Mg-doped GaN has been realized for the first time by low-energy electron beam irradiation (LEEBI) treatment[116] of metal-organic vapor phase epitaxy (MOVPE)-grown Mg-doped films. Later on, Nakamura *et al.*[117] achieved the *p*-type conduction in GaN by thermal annealing of the MOCVD-grown Mg-doped films, more recently; *p*-type GaN has been obtained by plasma-enhanced molecular beam epitaxy (MBE) without the need for a postannealing procedure.[118,119] These results support the findings and suggestions of Nakamura *et al.*[106] that acceptor H neutral complexes are formed in the Mg-doped GaN during CVD as a result of the H_2 carrier gas and diluent during the growth. These complexes, in turn, effectively reduce the number of acceptor states which could be occupied by electrons from the valence band and result in a compensated material. A decrease of H-atom concentration was observed after the thermal treatment in Ar gas, supporting the hypothesis that H-atom extraction plays an important role in obtaining low-resistivity *p*-type conduction.[107] The use of gas source MBE, in which the only H is derived from the background, permits the direct deposition of *p*-type material without the need for postdeposition processing. Figure 37 shows the relationship between room-temperature hole concentration and mobility in GaN films grown by various groups using both MOVPE and MBE. The circles correspond to the Mg-doped samples, and the squares to what is perceived to be unintentionally doped C samples. While the Mg-doped layers needed activation by the N_2 heat treatment, or by a low-energy beam irradiation, the C-doped layers needed none. A statistical averaging suggests that the hole mobility decreases in general with increasing carrier concentration.

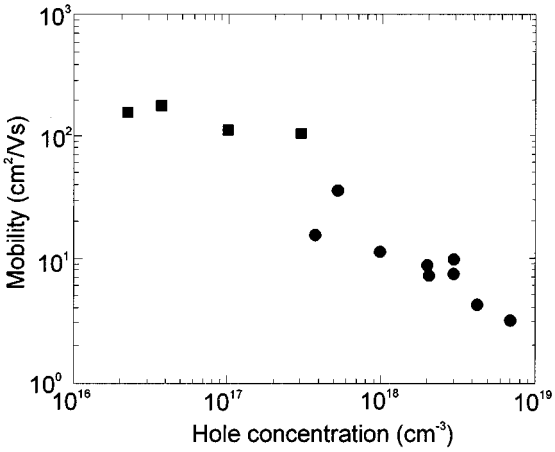

FIG. 37. The 300 K Hall mobility vs hole concentration for GaN from various groups using both QMVPE and MBE, the solid squares are for C-doped samples and the solid circles are for Mg-doped samples (after Ref. 120),

Recently, Rubin and co-workers[121] have succeeded in making *p*-type GaN using MBE assisted by a direct nitrogen ion beam together with a variety of doping techniques used in conventional integrated circuit processing (ion implantation, diffusion, and coevaporation of Mg). The undoped films had hole concentrations of 5×10^{11} cm^{-3} and hole mobilities of over 400 cm^2/V s at 250 K. From the slope of the carrier concentration versus temperature shown in Fig. 38(a), an activation energy of 0.29 eV is obtained. The strong temperature dependence of the mobility [see Fig. 38(b)] indicates the dominant contribution of a phonon scattering mechanism.

A conversion of unintentionally doped *n*-type GaN layers to *p*-type material was performed by the diffusion process of Mg in a sealed ampoule for 80 h at atmospheric N_2 pressures at 800 °C. After this, Hall measurements indicated a hole concentration of 2×10^{16} cm^{-3} and a mobility of 12 cm^2/V s.

P-type inversion conductivity has also been obtained after Mg implantation with large doses (2×10^{14} cm^2). However, high-energy implants (80–100 keV) introduced strain and defects into GaN films, and even after annealing at 800 °C for 30 min in N_2, the x-ray peaks did not return to their initial positions. Films implanted with Mg ions at lower energies (40–60 keV) recovered their original lattice param-

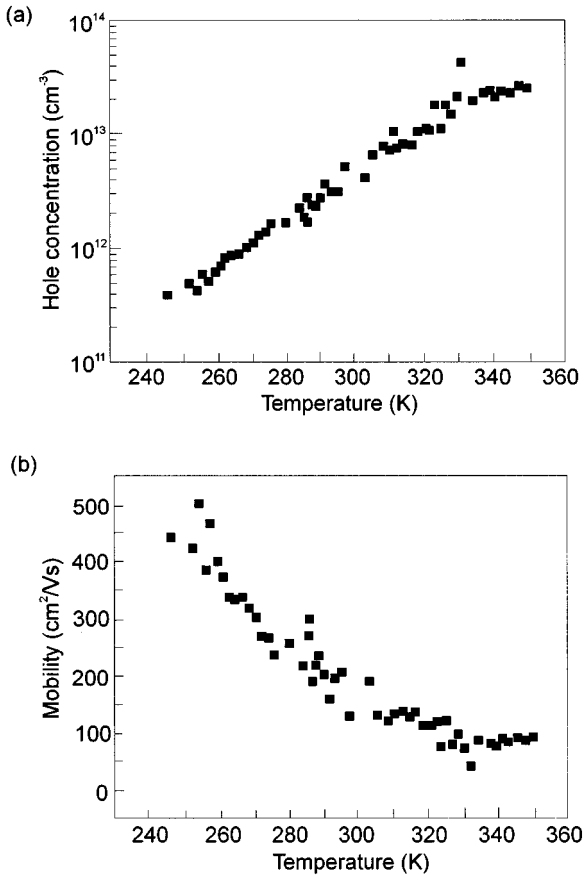

FIG. 38. Hall carrier concentration (a) and Hall mobility (b) vs temperature for undoped p-type GaN (after Ref. 121).

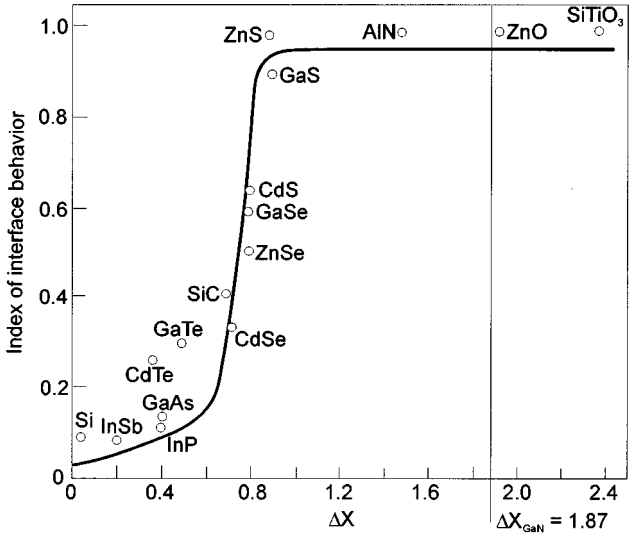

FIG. 39. Dependence of $S=d\Phi_b/\chi_m$ (change in barrier height over the change in metal work function) on the electronegativity difference between the components of the compound (after Ref. 126).

eter after annealing at 800 °C and hot-point probe tests confirmed that these lower energy implants produced p-type conduction.

For selective area doping or isolation of GaN samples the use of ion implantation is a critical requirement for advancement of device technology. Pearton *et al.*[122] have reported achievement of both n- and p-type GaN using Si^+ and $Mg^+ + P^+$ implantation, respectively, and also the creation of semi-insulating ($\geqslant 5\times 10^9\ \Omega/\square$) regions in initially n- and p-type material using multiple energy N^+ implantation and subsequent annealing.

Recently Wilson *et al.*[123] have reported results of measurements of depth profiles and stability against redistribution with annealing up to 800 or 900 °C, for implanted Be, Cl, Mg, Si, S, Zn, Ge, and Se as dopants in GaN. They found excellent thermal stability for acceptors (Be, Mg, Zn, and C) and for group IV donors (Si and Ge) for temperatures up to 900 °C. In the case of the group VI donors, S redistributes at 600 °C, and Se at 800 °C. It means also that diffusion of most elements into GaN from an external source does not appear to be a feasible approach for doping GaN samples.

In spite of achievements in the fabrication of GaN material, this material is still far from ideal. p-type and n-type samples exhibit photoconductivity responses at photon energies far below the band-gap energy.[124] It may be largely related to the deep tail states created by the high growth temperature, the large stress arising from the lattice mismatch to the substrate, impurity incorporation, and impurity compensation. Understanding their origin in order to eliminate the defect states will be an important endeavor in the near future for device development based on GaN films.

B. Ohmic contacts to GaN

Early results for GaN indicate that ohmic contacts can easily be formed to both n- and p-type material. The most popular contacts for many years for Hall measurements are soldered ln contacts. The first investigation of GaN contacts was carried out by Foresi and Moustakas.[125] The Au and Al contacts were deposited on the n-type GaN layers by thermal evaporation and patterned using photolithography and liftoff techniques. Current–voltage characteristics show that the as-deposited Al contacts are ohmic while the as-deposited Au contacts are rectifying and form Schottky barriers. These Schottky barriers are leaky due to tunneling effects arising from the high carrier concentration of the films and the possible existence of an interfacial native oxide layer. The Au contacts become ohmic after annealing at 575 °C for 10 min, a result attributed to gold diffusion in GaN. Measurements of the contact resistivities of Al and Au annealed contacts gave values in the range of 10^{-7} –$10^{-8}\ \Omega\,\mathrm{m}^2$.

For most of the important semiconductors, including Si and GaAs, the dependence of the metal barrier height on the work function difference has not been observed due to the existence of surface states which pin the Fermi level at the interface. Figure 39 shows the dependence of the barrier height on the work function difference correlated to the ionicity of the semiconductor by Kurtin *et al.*[126] In this Fig. 39, the vertical axis is a parameter S which is defined as the change in barrier height over the change in metal work function ($S=d\Phi_b/\chi_m$) and the horizontal axis is the electronegativity difference between the components of a compound which is a measure of the compound's ionicity. The electronegativity difference for GaN is 1.87 eV.[127] This puts

GaN above the knee of the curve in Fig. 39 implying that Schottky barriers on GaN should have barrier heights which depend directly on the work function difference between the metal and GaN. It indicates that the surface Fermi energy is unpinned which greatly reduces the complication of creating ohmic contacts to GaN as it is only necessary to determine metals with appropriate work functions.

The work function of GaN has been measured to be 4.1 eV.[128] Therefore, any metal with a work function equal or lower than that of GaN should form an ohmic contact to *n*-type material, and any metal with a higher work function should form a rectifying contact to *n*-type GaN. The work function of Al is 4.08 eV[129] putting Al in the ohmic category. In the case of Au, the work function is 4.82 eV which puts Au in the rectifying category. The above theoretical predictions have been confirmed by the experimental results of Foresi and Moustakas.[125]

Theoretical predictions indicate that Al can form ohmic contacts to *n*-type and Au can form ohmic contacts to *p*-type GaN. Au as a contact to GaN requires a thin interlayer (Ti or Cr) to prevent a diffusion of Au in the GaN.

Lin *et al.*[130] have reported the results of an ohmic contact to *n*-GaN ($\sim 10^{17}$ cm^{-3}) study of four separate metallization schemes: Au, Al, Ti/Au, and Ti/Al. The metal layers were deposited via e-beam evaporation. Bilayer contacts consisted of a 20 nm Ti layer deposited directly on GaN, followed by a 100 nm capping layer of Au or Al. Prior to annealing only the Ti/Al contact exhibited near linear I–V characteristics. The other contacts exhibited nonlinear I–V characteristics even for small currents. It is probably due to the formation of rectifying Schottky contacts. Then different annealing procedures were used to improve contact characteristics: annealing at 500 °C in N_2 ambient; further annealing using the rapid thermal annealing (RTA) method at 700 °C for 20 s. Two samples, Al/Ti and Au/Ti were further annealed to 900 °C for 30 s. Device quality ohmic contacts with contact resistivity values of 8×10^{-6} Ω cm^2 have been obtained when Ti/Al contacts were annealed at 900 °C for 30 s. The nature of reactions responsible for the low resistance contacts has not been well clarified. The most likely mechanism for the low contact resistance is solid-phase epitaxy of TiN_2 via N outdiffusion. In this case the surface GaN would be highly *n*-type due to the preponderance of N vacancies and effective tunneling through a surface layer is possible.

A novel scheme of nonalloyed ohmic contacts on GaN using a short-period superlattice composed of GaN and narrow band-gap InN, sandwiched between the GaN channel and an InN cap layer, has been demonstrated by Lin *et al.*[131] A contact resistance as low as 6×10^{-5} Ω cm^2 with GaN doped at about 5×10^{18} cm^{-3} has been obtained without any postannealing.

C. Etching of III–V nitrides

GaN is characterized by its exceptional stability at high temperatures and under chemical attack. GaN is insoluble in H_2O acids or bases at room temperature, but dissolves in hot alkali solutions at very low rate.[57] Low quality material has been observed to etch at reasonably high rates in NaOH, H_2SO_4, and H_3PO_4. These etches are useful for identifying defects and estimating their densities in GaN layers. A recently published article stated that good quality GaN films etch slowly in 30%–50% NaOH/H_2O solutions (rate of $\sim$2 nm/min) while HF, H_3PO_4, and HNO_3/HCl mixtures are ineffective in producing any etching.[132] This chemical stability provides a challenge of GaN processing when conventional integrated circuit processing techniques are used. Smooth, controlled dry etching is necessary for fabrication of small geometry devices in a reproducible fashion. It means that etch rates must be achieved at a low dc bias where ion-induced damage is minimized.

In the last two years considerable progress in the exploration of different methods for RIE of III–V nitrides has been observed.[132–143] An attractive approach to this is the use of electron cyclotron resonance (ECR) discharges which produce high ion densities ($\geqslant 5\times10^{11}$ cm^{-3}) at low pressure with ion energies below the displacement damage threshold for III–V materials (i.e., $\leqslant$25 eV).[136]

Adesida *et al.*[134] reported a RIE of GaN in silicon tetrachloride plasmas ($SiCl_4$, 1:1 SiCl4:Ar, and 1:1/$SiCl_4$ SiE_4) in the pressure range between 20 and 80 m Torr. For all gas mixtures, each rate increased monotically with increasing plasma self-bias voltage exceeding 50 nm/min at 400 V. The slight overcut in the profiles was attributed to the significant physical component in the etching process. A wet etch in dilute HF was needed to clear the Si (in the form of SiO_4) embedded in the surface of GaN.

Based on an analogy to other III–V semiconductors, one would expect Cl-biased discharge chemistries to be useful for GaN and AlN because the III chlorides are volatile, and the addition of H_2 should remove the nitrogen as NH_3 Cl-based etches have worked well on GaN using ECR discharges of CH_4/H_2, Cl_2/H_2 and BCl_3/Ar, while the addition of F to the discharges dramatically reduces the etch rate of AlN, what can be used for selecting etching of AlN. Films $\sim$200 nm thick were lithographically patterned with Hunt 1182 photoresist to give openings of 1–100 μm in various shapes. Controlled rates of $\sim$20 nm/min were obtained at moderate dc biases ($\leqslant -200$ V), low pressure (1 mm Torr), and low microwave power (200 W). Higher etch rates of $\sim$70 nm/min at -150 V and 1 m Torr for high microwave powers (1000 W) have been obtained by Pearton *et al.*[136] with the Cl_2/H_2 chemistry. In this case a lithographic mask, AZ 1350J photoresist, was spun onto the samples. The surface of III–V nitrides remain stoichiometric without requiring a wet-etch cleanup. A success in RIE of GaN has also been achieved with BCl_3-etch rate 8.6 A/s which was obtained for a plasma power of 200 W and pressure of 10 m Torr.[135]

Alternative chemistries which have been proven advantageous in improving etch rates or selectivities in various applications include those based the group III etch products in iodine plasmas. A comparison of etch rates of GaN, AlN, and InN in HI/H_2 high ion density ($\sim 5\times10^{11}$ cm^{-3}) plasma with results obtained from chlorine-based chemistries indicates that a HI/H_2/Ar plasma chemistry produces slightly faster etch rates for GaN and AlN than comparable Cl_2-based mixtures, while the rates for InN are significantly improved.[139] By contrast, HBr/H_2/Ar yields slower etch rates

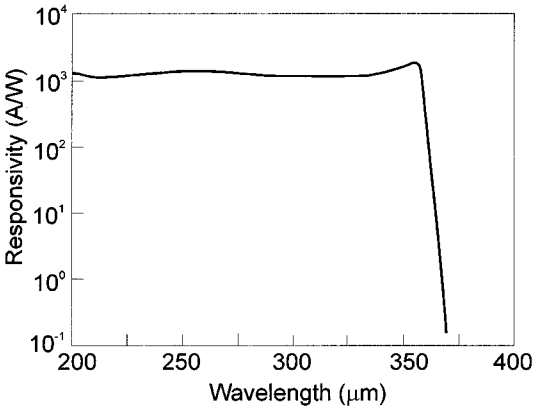

FIG. 40. Normalized spectral responsivity for a GaN photoconductive detectorn (after Ref. 144),

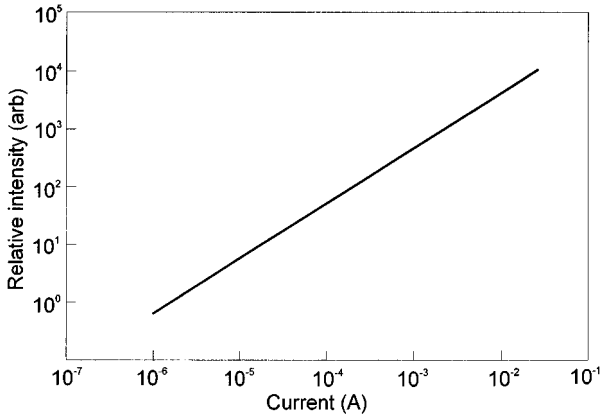

FIG. 41. GaN photoconductive detector responsivity as a function of incident power under 254 nm excitation (after Ref. 144),

than the chlorine chemistries for all three binary band gap nitrides. Both types of chemistries produce smooth but highly anisotropic etched features. RIE of GaN using CHF_3/Ar and C_2ClF_5/Ar chemistries has also been reported.[143] The etch rates which varied between 60 and 470 Å/min, were found to increase linearly with rf plasma power and to decrease with chamber pressure.

Recently, Pearton *et al.*[138,140,141] have studied the Ar^+-ion milling characteristics of III–V nitrides. It appears that the surface morphologies of all nitrides (GaN, InN, AlN, and InGaN) remain smooth after ion milling at 500 eV and there is no preferential sputtering of the nitrogen. The ion milling rate for the nitrides are less than those of masking materials such as SiO_2, SiN_x, and photoresist, so this technique is useful only for shallow-mesa applications. Dry etching methods involving an additional chemical component are more practical alternatives for device patterning, e.g., the use of an Ar ion beam and HCl gas in the chemically assisted ion beam etching of GaN may be suitable for the fabrication of laser facets and mirrors.[142]

D. AlGaN ultraviolet detectors

1. Photoconductive detectors

Development of high quality III–V nitride semiconductor layers in the last several years has resulted in the fabrication of a new generation of UV detectors. Due to this early stage of development only a few articles concerning UV detectors have been published.[109,144–153]

The first high quality GaN photoconductive detectors (using insulating material) were fabricated by Khan *et al.*[144] The active region of detector was a 0.8-μm-thick epitaxial layer of insulating GaN deposited over a 0.1-μm-thick AlN buffer layer using metal-organic chemical vapor deposition over basal-plane sapphire substrates. Interdigitated, electrical, 5000-Å-thick gold contacts were fabricated on the epilayers for the photoconductive response measurements. The interdigitated electrodes were 3 μm wide, 1 mm long, and had a 10 μm spacing. To define the electrode pattern, a standard photolithographic procedure and a lift-off technique were used.

Figure 40 shows the spectral responsivity of GaN photoconductive detectors. It reaches its maximum value at 365 nm and then remains nearly constant down to 200 nm. The peak responsivity is about 1000 A/W, and the estimated gain/quantum efficiency product for the detectors is 4.8×10^3. The response of GaN detectors is linear over five orders of incident radiation power, which is shown in Fig. 41. The detector response time is about 1 ms.

The performance of *n*-type GaN photoconductive detectors made from films grown by molecular beam epitaxy is inferior.[151] The following parameters have been measured for interdigitated device with Ti/Al ohmic contacts and 20 μm inter-electrode spacing: the gain/quantum efficiency product of 600 at 254 nm and at a bias of 25 V, the mobility/lifetime product of 9.5×10^{-5} cm^2/V and current responsivity of 125 A/W at 254 nm.

The responsivity of *p*-type GaN:Mg layers on Si substrate is lower in comparison with insulating layers, and achieved a maximum value of 30 A/W at 14 V bias.[149] The responsivity increases nearly linearly with applied voltage up to 8 V, then the increase slows toward saturation. Photocurrent decay for a pulsed input shows a hyperbolic type response. It is hypothesized that holes are captured at either compensated Mg deep acceptor sites or Mg-related trap/recombination centers, resulting in a greatly prolonged electron free carrier lifetime.

Recently Kung *et al.*[150] have studied the kinetics of the photoconductivity of *n*-type GaN photoconductive detectors by the measurements of the frequency dependent photoresponse and photoconductivity decay. Strongly sub-linear response and excitation-dependent response time have been observed even at relatively low excitation levels. This can be attributed to the redistribution of the charge carriers with increased excitation level.

Figure 42 shows the voltage responsivity of the GaN detector as a function of the modulation frequency for three different excitation power densities. From Fig. 42 we can see that the responsivity remains frequency dependent over the whole range of frequencies applied. This dependence is less pronounced for higher excitation levels. At high frequencies when the period of radiation power oscillations exceeds the lifetime, the frequency response curves for different excita-

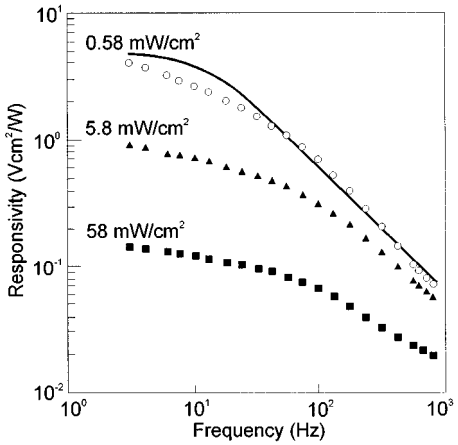

FIG. 42. GaN detector responsivity as a function of chopping frequency for three different excitation power densities of the He–Cd laser light (325 nm). The solid line shows the fit to conventional dependence of $R_v = R_{vo}(1+4\pi^2 f^2 t^2)^{1/2}$ (after Ref. 150).

tion level tends to have the same frequency dependence. This is because at high frequencies the photogenerated excess concentration becomes dependent only on the excitation period rather than the lifetime of the majority carrier lifetime. A consequence of the redistribution of the charge carriers with increased excitation level is the decreasing of the photoconductive gain with increasing in UV intensity, which has been recently observed by Goldenberg *et al.*[153] (see Fig. 43).

The observed kinetics of photoresponse have important consequences for practical applications. The measured lifetimes are too long for many applications resulting in the frequency dependent responsivity and nonlinear response. This can be changed in a number of ways including deliberate introduction of recombination centers to stabilize response time at a required level and by reducing the lifetime in short photoconductors using contact phenomena. Further work is necessary to understand the origin and properties of the deep centers in GaN.

2. Photovoltaic detectors

The first Schottky GaN barriers were reported over 20 years ago.[154] However, due to a fabrication procedure that

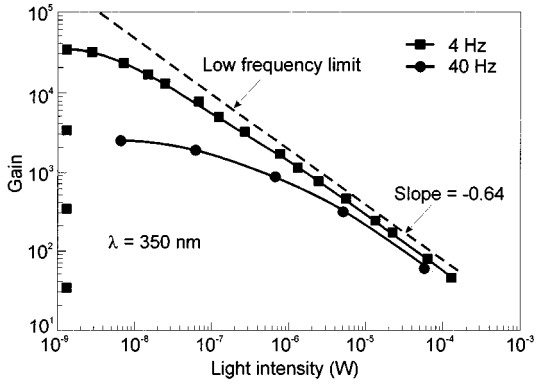

FIG. 43. The variation of photoconductive gain of GaN detector with intensity of light at 350 nm (after Ref. 153).

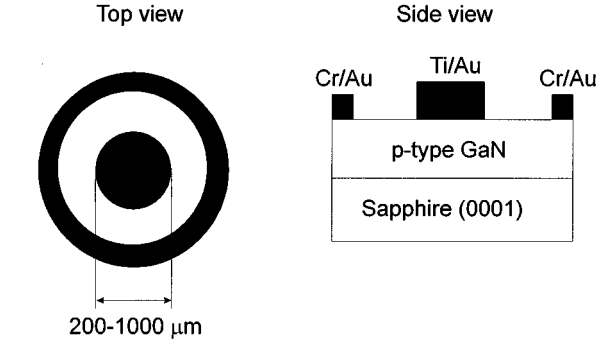

FIG. 44. Schematic device configuration of GaN Schottky barrier photodiode (after Ref. 145).

was not well controlled, an anomalous behavior of electrical properties of these Zn/GaN Schottky barriers has been observed.

More recently, Khan *et al.*[145] have reported the fabrication and characterization of Schottky barrier photodiodes on *p*-type GaN layers. As-grown 2-μm-thick material (grown over basal plane sapphire using MOCVD) was an *n*-type conductivity with residual carrier concentration of 10^{17} cm^{-3} and a room-temperature mobility of about 400 cm^2/V s. Post-growth, *p*-type conductivity was enhanced using a 20 min 650 °C N_2 ambient anneal. After this process, the hole concentration was about 7×10^{17} cm^{-3}. Subsequent to growth, doughnut-shaped Cr/Au (2000 Å thick) ohmic contacts were deposited using standard photolithographic techniques. Figure 44 shows the resulting device configuration. The inside diameters for the doughnuts were ranged from 200 μm to 1 mm. For improving the contact resistivities, the ohmic contacts were annealed in flowing forming gas at 350 Å for 1 min. As a Schottky barrier 1500-Å-thick Ti/Au metals were deposited. The estimated responsivity of these Schottky barriers was 0.13 A/W at wavelength 320 nm for a normalized area of 1 mm^2. The spectral responsivity is shown in Fig. 45. The response time of detectors is limited by the resistance capacitance (RC) time constant of the measured circuit and was around 1 μs. Other geometry of detectors with a Ti/Al Schottky barrier is shown in Fig. 46(a).

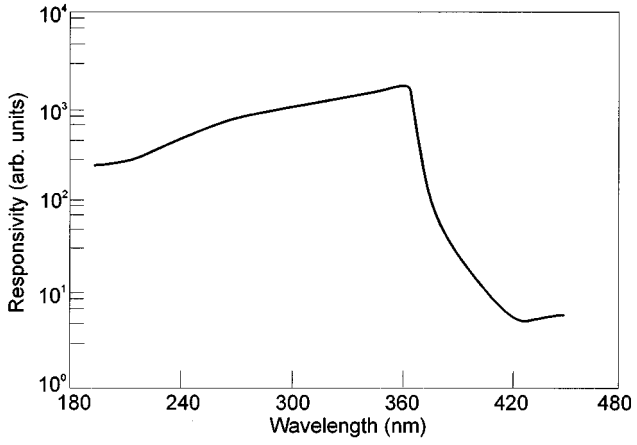

FIG. 45. Spectral responsivity of GaN Schottky barrier photodiode (after Ref. 145).

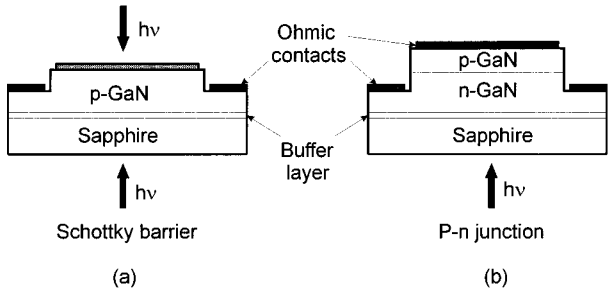

FIG. 46. GaN photovoltaic detector structures: (a) Schottky barrier and (b) p-n junction (after Ref. 109).

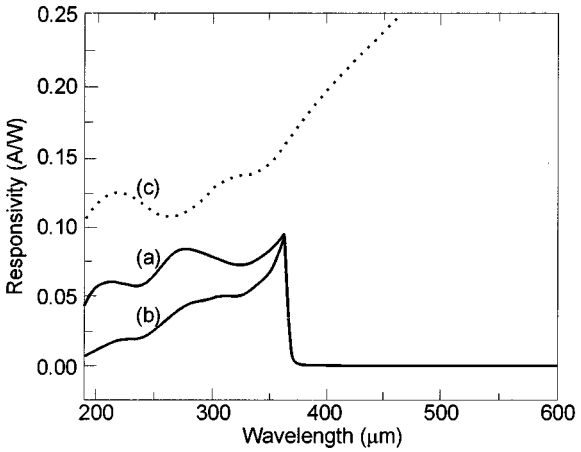

FIG. 47. Spectral responsivity of GaN p-n detectors: (a) light from the n side; (b) light from the p side; (c) spectral responsivity of UV-enhanced Si p-n junction (after Ref. 152).

It should be noticed that much information concerning GaN Schottky barriers is under discussion. The barrier height depends on a procedure used for diode fabrication. For example, Lin *et al.*[130] used Ti/Al and Ti/Au metallization and subsequent annealing to receive ohmic contacts to n-type GaN. Instead, Binari *et al.*[155] have fabricated Schottky barriers using a Ti layer and a Au overlayer deposited by electron-beam evaporation. The barrier height of Ti on n-type GaN has been measured to be 0.58 and 0.59 eV by capacitance–voltage ($C-V$) and current–voltage ($I-V$) techniques, respectively. The barrier height of Au on n-type GaN was determined to be 1.19 and 1.15 eV from $I-V$ and $C-V$ measurements[155] which is somewhat lower than reported previously by Hacke *et al.*[156] (0.84 eV by $I-V$ and 0.94 eV by $C-V$). Also, results presented by Guo *et al.*[157] for Pt and Pd barriers confirm that the metal work function should not be the only factor affecting the Schottky characteristics.

The first information about p-n junction GaN photovoltaic detectors is included in Ref. 109. Zhang *et al.*[158] have estimated by theoretical modeling of the spectral response shape of p-n junction that the diffusion length of holes in the n-type GaN region is about 0.1 μm. Next, Chen *et al.*[152] have studied two detector structures grown by low-pressure MOCVD, one n-on-p and the other p-on-n. The p-on-n sample consisted of the deposition over basal plane sapphire of a 1-μm-thick unintentionally doped n-GaN layer followed by a 0.5-μm-thick Mg-doped p-GaN layer. Similarly, the n-on-p structure consisted of a 1 μm p-GaN layer followed by a 0.5 μm n-GaN layer. Large area mesa structures were defined using reactive ion etching [Fig. 46(b)]. Ohmic contacts were formed using sputtered W for n- and e-beam evaporated Ni/Au bilayer for the p contacts. These electrode patterns were formed by standard lift-off processes. The spectral responsivity data are plotted in Fig. 47. The maximum responsivity (0.09 A/W) is comparable to that of a UV-enhanced Si detector. The rise and fall times of the photoresponse were measured to be $\sim$0.4 ms for a detector area of 16 mm^2. However, these times are significantly greater than the value of 1 μs for the estimated RC time constant. More work is needed to identify the factors responsible for the decrease in the photodiode speed.

More sophisticated structures are also used for the detection of UV radiation. Recently, Khan *et al.*[147,148] have reported the GaN/AlGaN heterostructure field-effect transistors (HFETs) as gated visible blind photodetectors. These 0.2 μm gate HFETs operated as microwave amplifiers to a temperature of 300 °C with maximum oscillation frequency and cutoff frequency of $\approx$70 MHz and $\approx$22 GHz, respectively, at room temperature. Figure 48 shows the schematic diagram of the short gate GaN/AlGaN HFET. The thickness of the AlGaN barrier layer is approximately 25 nm, and its doping is on the order of 4×10^{18} cm^{-3}. The GaN layer is unintentionally doped. The gated photodetectors are backside illuminated. The electron-hole pairs are generated in the semi-insulating i-GaN buffer layer and in the active n-GaN region. The photogenerated holes move towards the i-GaN/sapphire interface, and the photogenerated electrons move towards the channel where they are quickly driven into the drain by the high channel field. The measured and calculated responsivity of a backside illuminated GaN/AlGaN HFET photodetector is shown in Fig. 49. The maximum responsivity of 3000 A/W was achieved at a gate voltage of about 1 V. The spectral responsivity (see Fig. 50) falls sharply by two orders of magnitude for wavelengths larger than 365 nm, which demonstrates the visible blind operation of gated photodetector.

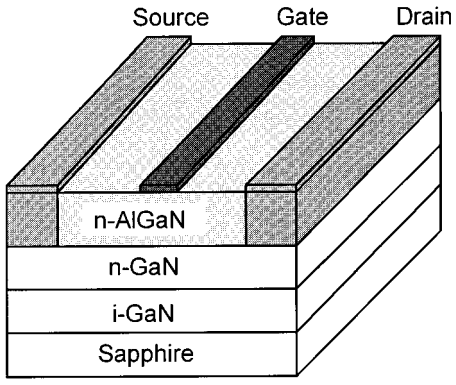

FIG. 48. Schematic diagram of the GaN/AlGaN HFET (after Ref. 159).

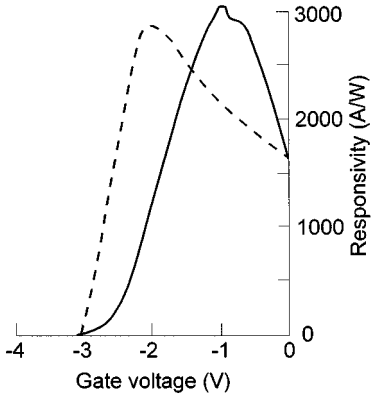

FIG. 49. Measured (solid line) and calculated (dashed line) responsivity of 0.2 μm gate GaN/AlGaN HFET photodetector backside illuminated with He–Cd laser (λ=325 nm). Drain-to-source voltage 10 V (after Ref. 147).

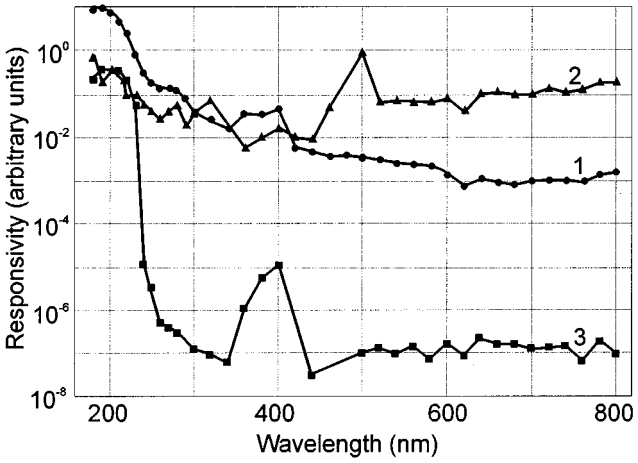

FIG. 51. Spectral responsivity (arbitrary units) of diamond photoconductive device: (1) as-fabricated, (2) following methane annealing, and (3) after methane and air annealing (after Ref. 162).

VIII. OTHER MATERIALS FOR ULTRAVIOLET DETECTORS

A straightforward way to make a highly selective (blindless) UV detectors is to use wide band-gap semiconductors. However, due to technological difficulties with those materials, the UV detectors are fabricated also with Si and GaAs. Their principal advantage lies in the high crystalline quality of the materials and their well-known processing methods. Recently, Constant *et al.*[160] have presented GaAs photoconductive detectors with static responsivity values of 10^{7}–10^{8} A/W in UV spectral range. Some applications require the measurement of UV radiation in the presence of visible light. The final design of the devices can include additional blocking filters or dielectric coating to fit them for the wavelength of interest.

Misra *et al.*[161] have presented preliminary results concerning fabrication and characterization of BN_xP_{1-x} photoconductive detectors. This alloy system is an attractive material for UV application because its band gap can be tuned in the UV region (between 200 and 400 nm) by adjusting the boron phosphide (BP) to boron nitride (BN) ratio in the ternary compound.

Also recently, for the first time, to the best of our knowledge, the dramatic improvement in diamond photoconductive characteristics (10^{6} higher response to 200 nm than visible wavelengths, $<$0.1 nA dark current) has been achieved following methane-air treatment of the polycrystalline material.[162] Figure 51 (curve 3) shows the dramatic change in the response (for wavelengths less than 225 nm) after 700 °C treatment in a methane ambient (1 h) and second treatment at 400 °C in air (1 h). The improvement in the device characteristics indicates an active role for methane-air gases in modifying the surface, or near surface, region of the thin-film polycrystalline diamond.

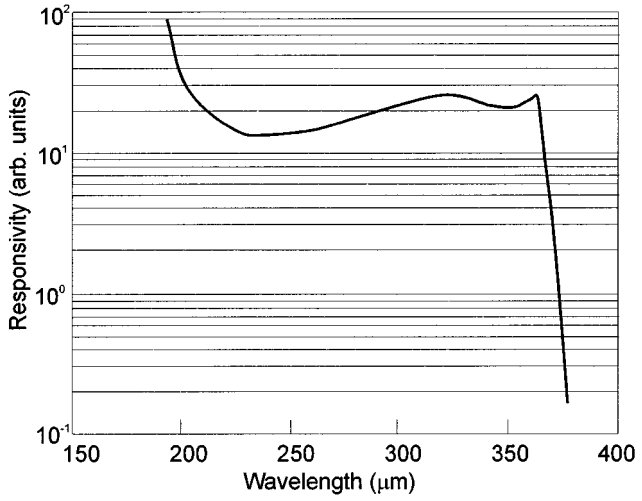

FIG. 50. Measured spectral responsivity of 0.2 μm gate GaN/AlGaN HFET photodetector (after Ref. 147).

IX. CONCLUSIONS

Currently, the old detection techniques used in UV technology (photographic films, detectors based on gas photoionization, and photoemissive detectors) are replaced by semiconductor photon detectors where higher sensitivity, more quantitatively accurate photometric information, or more immediate data availability are required. The semiconductor detectors offer small size, ruggedness, and ease of use. Expansion of the semiconductor industry and the continuing emphasis on the development of low-light level imaging systems for military and civilian surveillance applications ensure the dominant position of these detectors in the near future. Manufactured using proven wafer-scale silicon or III–V processing techniques, they are inherently cheaper and provide high quantum efficiency. At present, a new class of video-rate imagers based on thinned, back-illuminated silicon charge coupled devices (CCDs) with improved UV sensitivity (to 50% quantum efficiency at 200 nm) is available to replace conventional image intensifiers.[162] However, Si photodetectors require bulky band filters to block the visible solar radiation background and are intolerant of elevated temperatures and caustic environments. With the use of wide band-gap semiconductors (like GaN or diamond), the need

for these filters will be largely eliminated simplifying the design of the spectroscopic monitoring equipment. Moreover, these devices are potentially free from the mentioned shortcomings; they are capable of operating at high temperatures and in hostile environments.

Interest in a new generation of wide band-gap semiconductor detectors stems in part from the fact that the Earth's atmosphere is opaque at wavelength below 300 nm. To take advantage of this optical window, Earth to space communication will need detectors that are UV sensitive but blind to the ambient visible radiation. Another area where these detectors can find applications is in the combustion monitoring of gases where UV emission is a normal by-product.

Semiconductor diamond is of considerable interest for UV detectors. Unfortunately, diamond of a good enough quality is not readily available, and appropriate technology is far from being mature. However, recent progress in diamond thin-film technology is promising for future applications.

Unlike SiC, which is another wide band-gap semiconductor with demonstrated n- and p-type doping and excellent power device performance, one notable advantage of III–V nitrides is that they form direct band-gap heterostructures, have better ohmic contacts and heterostructures. Because of this, it is anticipated that III–V nitrides may eventually prove to be more promising than SiC for optoelectronic devices.

The future direction in research and development of GaN-based UV detectors (mainly photodiodes) can be judged from the remarkable progress in their performance attained over the last few years. A late newspaper at an International Electron Device Meeting announces the first observation of stimulated emission from a current injected InGaN/AlGaN double-heterostructure diode.[163,164] The major obstacle prohibiting the sort of improvement needed is the large concentration of defects, although some attribute some of the shortcomings to processing-related problems. Large concentrations of defects (10^7–10^{10} cm^{-2}) in GaN structures manifest themselves as short carrier lifetimes and reduced photoluminescence intensity. Further progress will more likely be due to the use of better matched substrates. A great deal of effort is presently being expended in laboratories everywhere to search for a better substrate or compliant base to decrease the defect generation, and thus increase quantum efficiency and photoconductive gain of detectors.[165]

[1] J. A. R. Samson, *Techniques of Vacuum Ultraviolet Spectroscopy* (Wiley, New York, 1967).
[2] *The Middle Ultraviolet: Its Science and Technology*, edited by A. E. S. Green (Wiley, New York, 1966).
[3] L. R. Koller, *Ultraviolet Radiation* (Wiley, New York, 1965).
[4] A. N. Zaidel and E. Ya. Shreider, *Vacuum Ultraviolet Spectroscopy* (Humphrey, Ann Arbor, MI, 1970).
[5] J. Hennes and L. Dunkleman, *The Middle Ultraviolet: Its Science and Technology*, edited by A. E. S. Green (Wiley, New York, 1966), Chap. 15.
[6] R. E. Huffman, *Atmospheric, Ultraviolet Remote Sensing*, International Geophysics Series (Academic, New York, 1992), Vol. 52.
[7] R. E. Huffman, *Ultraviolet Optics and Technology*, SPIE Milestone Series (SPIE Optical Engineering, Bellingham, Washington, 1993), Vol. MS 80.
[8] G. R. Carruthers, *Electro-Optics Handbook*, edited by R. W. Waynant and M. N. Ediger (McGraw-Hill, New York, 1994), Chap. 15.
[9] J. G. Timothy and R. P. Madden, *Handbook on Synchrotron Radiation*, edited by E. E. Koch (North-Holland, Amsterdam, 1983), pp. 315–366.
[10] M. J. Eccles, M. E. Sim, and K. P. Tritton, *Low Light Level Detectors in Astronomy* (Cambridge University Press, Cambridge, England, 1983).
[11] J. G. Timothy, Publ. Astron. Soc. Pac. **95**, 810 (1983).
[12] J. R. Janesick, T. Elliott, S. Collins, H. Marsh, M. Blouke, and M. Freeman, Proc. SPIE **501**, 2 (1984).
[13] B. Y. Welsh and M. Kaplan, Proc. SPIE **1743**, 452 (1992).
[14] C. L. Joseph, Wisconsin Astrophy. No. 562, 1 (1995).
[15] M. P. Ulmer, M. Razeghi, and E. Bigan, Proc. SPIE **2397**, 210 (1995).
[16] J. R. Janesick, D. Campbell, T. Elliott, and T. Daud, Opt. Eng. **26**, 825 (1987).
[17] R. A. Stern, R. C. Catura, R. Kimble, A. F. Davidsen, M. Winzenread, M. M. Blouke, R. Hayes, D. M. Walton, and J. L. Culhane, Opt. Eng. **26**, 875 (1987).
[18] G. Naletto, G. Tondello, G. Bonanno, R. Di Benedetto, and S. Scuderi, Opt. Eng. **38**, 2544 (1994).
[19] M. M. Blouke, M. W. Cowens, J. E. Hall, J. A. Westphal, and A. B. Christensen, Appl. Opt. **19**, 3318 (1980).
[20] M. W. Cowens, M. M. Blouke, T. Fairchild, and J. A. Westphal, Appl. Opt: **19**, 3727 (1980).
[21] J. R. Janesick, T. Elliott, G. Fraschetti, S. Collins, M. Blouke, and B. Corrie, Proc. SPIE **1071**, 153 (1989).
[22] A. Rose, *Concepts in Photoconductivity and Allied Problems* (Interscience, New York, 1963).
[23] J. Piotrowski, *Infrared Photon Detectors*, edited by A. Rogalski (SPIE Optical Engineering, Bellingham, Washington, 1995), Chap. 11.
[24] P. W. Kruse, L. D. McGlauchlin, and R. B. McQuistan, *Elements of Infrared Technology* (Wiley, New York, 1962).
[25] P. W. Kruse, *Optical and Infrared Detectors*, edited by R. J. Keyes (Springer, Berlin, 1977), pp. 5–69.
[26] D. H. Seib and L. W. Aukerman, *Advances in Electronics and Electron Physics*, edited by L. Morton (Academic, New York, 1973), Vol. 34, pp. 95–221.
[27] W. Van Roosbroeck, Bell Syst. Tech. J. **29**, 560 (1950).
[28] X. Zhang, P. Kung, D. Walker, J. Piotrowski, A. Rogalski, A. Saxler, and M. Razeghi, Appl. Phys. Lett. **67**, 2028 (1995).
[29] R. A. Smith, *Semiconductors* (Cambridge University Press, Cambridge, England, 1978).
[30] E. S. Rittner, *Photoconductivity Conference at Atlantic City 1954*, edited by R. Breckenbridge, B. Russel, and E. Hahn (Wiley, New York, 1956), pp. 215–268.
[31] C. T. Elliott, *Handbook on Semiconductors*, edited by C. Hilsum (North-Holland, Amsterdam, 1993), Vol. 4, pp. 841–936.
[32] A. Van der Ziel, *Fluctuation Phenomena in Semiconductors* (Butterworths, London, 1959).
[33] F. N. Hooge, Phys. Lett. **29** A, 123 (1969).
[34] R. D. Nelson, Opt. Eng. **16**, 275 (1977).
[35] V. Gopal, Infrared Phys. **25**, 615 (1985).
[36] H. J. Hovel, *Semiconductors and Semimetals*, edited by R. K. Willardson and A. C. Berr (Academic, New York, 1975), Vol. 11.
[37] T. S. Moss, G. J. Burrel, and B. Ellis, *Semiconductor Optoelectronics* (Butterworths, London, 1973).
[38] M. J. Buckingham and E. A. Faulkner, Radio Electron. Eng. **44**, 125 (1974).
[39] C. T. Sah, R. N. Noyce, and W. Shockley, Proc. IRE **45**, 1228 (1957).
[40] S. C. Choo, Solid-State Electron. **11**, 1069 (1968).
[41] S. M. Sze, *Physics of Semiconductor Devices* (Wiley, New York, 1981).
[42] R. J. McIntyre, IEEE Trans. Electron Devices **ED-13**, 164 (1966).
[43] A. Rose, Phys. Rev. **97**, 1538 (1955).
[44] M. A. Lampert, Phys. Rev. **103**, 1648 (1956).
[45] M. A. Lampert and P. Mark, *Current Injections in Solids*, edited by H. G. Booker and N. DeClaris (Academic, New York, 1970).
[46] J. A. Edmond, K. Das, and R. F. Davis, J. Appl. Phys. **63**, 922 (1988).
[47] D. E. Sawyer and R. H. Rediker, Proc. IRE **46**, 1122 (1958).
[48] W. W. Gartner, Phys. Rev. **116**, 84 (1959).
[49] E. R. Rhoderick, IEE Proc. **129**, 1 (1982).
[50] A. M. Cowley and S. M. Sze, J. Appl. Phys. **36**, 3212 (1965).
[51] W. Schottky and E. Spenke, Wiss. Veroff. Siemens-Werken. **18**, 225 (1939).
[52] E. Spenke, *Electronic Semiconductors* (McGraw-Hill, New York, 1958).
[53] H. A. Bethe, MIT Radiation Laboratory Report No. 43-12, 1942.
[54] C. R. Crowell and S. M. Sze, Solid-State Electron. **9**, 1035 (1966).
[55] G. Ottaviani, K. N. Tu, and J. M. Mayer, Phys. Rev. Lett. **44**, 284 (1980).
[56] M. Krumrey and E. Tegeler, Nucl. Instrum. Methods A **288**, 114 (1990).
[57] S. Strite and H. Morkoc, J. Vac. Sci. Technol. B **10**, 1237 (1992).
[58] H. Morkoc, S. Strire, G. B. Gao, M. E. Lin, B. Sverdlov, and M. Burns, J. Appl. Phys. **76**, 1363 (1994).

[59] S. N. Mohammad, A. A. Salvador, and H. Morkoc, Proc. IEEE **83**, 1306 (1995).
[60] E. O. Johnson, RCA Rev. **26**, 163 (1965).
[61] R. W. Keyes, Proc. IEEE **60**, 225 (1972).
[62] M. Marchywka, S. C. Binari, P. E. Pehrsson, and D. Moses, Proc. SPIE **2282**, 20 (1994).
[63] Y. Talmi and R. W. Simpson, Appl. Opt. **19**, 1401 (1980).
[64] R. Korde, L. R. Canfield, and B. Wallis, Proc. SPIE **932**, 153 (1988).
[65] E. Kooi, IEEE Trans. Electron Devices **ED-13**, 238 (1966).
[66] T. E. Hansen, Phys. Scr. **18**, 471 (1978).
[67] R. Korde and J. Geist, Appl. Opt. **26**, 5284 (1987).
[68] United Detector Technology Inc., Data Sheet (1980).
[69] R. Korde and J. Geist, Solid-State Electron. **30**, 89 (1987).
[70] L. R. Canfield, J. Kerner, and R. Korde, Appl. Opt. **28**, 3940 (1989).
[71] S. G. Chamberlain, J. Appl. Phys. **50**, 7228 (1979).
[72] H. Ouchi, T. Mukai, T. Kamei, and M. Okamura, IEEE Trans. Electron Devices **ED-26**, 1965 (1979).
[73] C. M. Botchek, *VLSI Basic MOS Engineering* (Pacific Technical, Sarasota, FL, 1984), Vol. 1, p. 275.
[74] Z. A. Weinberg, D. R. Young, J. A. Calise, S. A. Cohen, J. C. DeLuca, and V. R. Deline, Appl. Phys. Lett. **45**, 1204 (1984).
[75] R. S. Popovic, K. Solt, U. Falk, and Z. Stoessel, Sensors and Actuators **A21–A23**, 553 (1990).
[76] R. F. Wolffenbuttel, Sensors and Actuators **A21–A23**, 559 (1990).
[77] W. Huang, C. Salupo, L. F. Szabo, G. P. Ceaser, and W. Iavurek, Mater. Res. Soc. Symp. Proc. **118**, 411 (1988).
[78] Y. K. Fang, S. B. Hwang, K. H. Chen, C. R. Liu, M. J. Tsai, and L. C. Kuo, IEEE Trans. Electron Devices **ED-39**, 292 (1992).
[79] R. C. Alig, S. Bloom, and C. W. Struck, Phys. Rev. B **22**, 5565 (1980).
[80] E. Sakai, Nucl. Instrum. Methods **196**, 121 (1982).
[81] T. Kabayashi, Appl. Phys. Lett. **21**, 150 (1972).
[82] L. R. Canfield and J. Kerner, Proc. SPIE **1344**, 372 (1990).
[83] L. R. Canfield, R. Vest, T. N. Woods, and R. Korde, Proc. SPIE **2282**, 31 (1984).
[84] M. Lavagna, J. P. Pigue, and Y. Marfaing, Solid-State Electron. **20**, 235 (1977).
[85] R. D. Baertsch and J. R. Richardson, J. Appl. Phys. **40**, 229 (1969).
[86] H. Fabricius, T. Skettrup, and P. Bisgaard, Appl. Opt. **25**, 2764 (1986).
[87] M. Krumrey, E. Tegler, J. Barth, M. Krisch, F. Schafers, and R. Wolf, Appl. Opt. **27**, 4336 (1988).
[88] E. Tegeler and M. Krumrey, Nucl. Instrum. Methods A **282**, 701 (1989).
[89] A. D. Wilson and H. Lyall, Appl. Opt. **25**, 4530 (1986).
[90] M. Marchywka, J. F. Hochedez, M. W. Geis, D. G. Socker, D. Moses, and R. T. Goldberg, Appl. Opt. **30**, 5010 (1991).
[91] G. Zhao, T. Stacy, E. M. Charlson, E. J. Charlson, M. Hajsaid, R. Roychoudhury, A. H. Khan, J. M. Meese, Z. He, and M. Prelas, Mater. Res. Soc. Symp. Proc. **339**, 191 (1994).
[92] M. C. Hicks, C. R. Wronski, S. A. Grot, G. Sh. Gildenblat, A. R. Badzian, T. Badzian, and R. Messier, J. Appl. Phys. **65**, 2139 (1989).
[93] R. B. Campbell and H. Chang, Solid-State Electron. **10**, 949 (1967).
[94] P. Glasow, G. Ziegler, W. Suttrop, G. Pensl, and R. Helbig, Proc. SPIE **868**, 40 (1987).
[95] D. M. Brown, E. T. Downey, M. Ghezzo, J. W. Kretchmer, R. J. Saia, Y. S. Liu, J. A. Edmond, G. Gati, J. M. Pimbley, and W. E. Schneider, IEEE Trans. Electron Devices **ED-40**, 325 (1993).
[96] J. A. Edmond, H. S. Kong, and C. H. Carter Jr., Phys. B **185**, 453 (1993).
[97] Y. Hirabayashi, S. Karasawa, K. Kobayashi, S. Misawa, and S. Yoshida, Sensors and Actuators A **43**, 164 (1994).
[98] Y. K. Fang, S. B. Hwang, K. H. Chen, C. R. Liu, M. J. Tsai, and L. C. Kuo, IEEE Trans. Electron Devices **ED-39**, 292 (1992).
[99] G. Cesare, F. Irrera, F. Palma, M. Tucci, E. Jannitti, G. Naletto, and P. Nicolosi, Appl. Phys. Lett. **67**, 335 (1995).
[100] C. Fröjdh, G. Thungström, H. E. Nilsson, and C. S. Petersson, Phys. Scr. T **54**, 169 (1994).
[101] C. Fröjdh, G. Thungström, H. E. Nilsson, and C. S. Petersson, Mater. Res. Soc. Symp. Proc. **339**, 215 (1994).
[102] M. M. Anikin, A. N. Andreev, S. N. Pyatko, N. S. Savkina, A. M. Strelchuk, A. L. Syrkin, and V. E. Chelnokov, Sensors and Actuators A **33**, 91 (1992).
[103] M. M. Anikin, A. N. Andreev, A. A. Lebedev, S. N. Pyatko, M. G. Rastegaeva, N. S. Savkina, A. M. Strelchuk, A. L. Syrkin, and V. E. Chelnokov, Sov. Phys. Semicond. **25**, 198 (1991).
[104] L. G. Matus, J. A. Powell, and C. S. Salupo, Appl. Phys. Lett. **59**, 1770 (1991).
[105] P. G. Neudeck, D. J. Larkin, J. A. Powell, L. G. Matus, and C. S. Salupo, Appl. Phys. Lett. **64**, 1386 (1994).
[106] S. Nakamura, T. Mukai, M. Senoh, and N. Iwasa, Jpn. J. Appl. Phys. **31**, L139 (1992).
[107] Y. Ohba and A. Hatano, Jpn. J. Appl. Phys. **33**, L1367 (1994).
[108] I. Akasaki and H. Amano, J. Electrochem. Soc. **141**, 2266 (1994).
[109] M. A. Khan, Q. Chen, C. J. Sun, M. S. Shur, M. F. Macmillan, R. P. Devaty, and J. Choyke, Proc. SPIE **2397**, 283 (1995).
[110] S. Strite, M. E. Lin, and H. Morkoc, Thin Solid Films **231**, 197 (1993).
[111] R. F. Davis, Proc. IEEE **79**, 702 (1991).
[112] S. Nakamura, Y. Harada, and M. Senoh, Appl. Phys. Lett. **58**, 2021 (1991).
[113] V. W. Chin, T. L. Tansley, and T. Osotchan, J. Appl. Phys. **75**, 7365 (1994).
[114] R. P. Joshi, Appl. Phys. Lett. **64**, 223 (1994).
[115] M. A. Khan, J. N. Kuznia, J. M. Van Hove, D. T. Olson, S. Krishnankutty, and R. M. Kolbas, Appl. Phys. Lett. **58**, 526 (1991).
[116] H. Amano, M. Kito, K. Hiramatsu, and I. Akasaki, Jpn. J. Appl. Phys. **28**, L2112 (1989).
[117] S. Nakamura, N. Iwasa, M. Senoh, and T. Mukai, Jpn. J. Appl. Phys. **31**, 1258 (1992).
[118] T. D. Moustakas and R. J. Molnar, Mater. Res. Soc. Proc. **281**, 753 (1993).
[119] M. E. Lin, G. Xue, G. L. Zhu, J. E. Greene, and H. Morkoc, Appl. Phys. Lett. **63**, 932 (1993).
[120] D. K. Gaskill, L. B. Rowland, and K. Doverspike, in *Properties of Group III Nitrides*, edited by J. H. Edgar (INSPEC, IEE, London, 1994), pp. 101–116.
[121] M. Rubin, N. Newman, J. S. Chan, T. C. Fu, and J. T. Ross, Appl. Phys. Lett. **66**, 64 (1994).
[122] S. J. Pearton, C. B. Vartuli, J. C. Zolper, C. Yuan, and R. A. Stall, Appl. Phys. Lett. **67**, 1435 (1995).
[123] R. G. Wilson, S. J. Pearton, C. R. Abernathy, and J. M. Zavada, Appl. Phys. Lett. **66**, 2238 (1995).
[124] C. H. Qiu, C. Hoggatt, W. Melton, M. W. Leksono, and J. I. Pankove, Appl. Phys. Lett. **66**, 2712 (1995).
[125] J. S. Foresi and T. D. Moustakas, Appl. Phys. Lett. **62**, 2859 (1993).
[126] K. Kurtin, T. C. McGill, and C. A. Mead, Phys. Rev. Lett. **22**, 1433 (1969).
[127] C. M. Wolfe, N. Holonyak, Jr., and G. S. Stillman, *Physical Properties of Semiconductors* (Prentice-Hall, Englewood Cliffs, NJ, 1989).
[128] J. I. Pankove and H. E. P. Schade, Appl. Phys. Lett. **25**, 53 (1974).
[129] K. W. Böer, *Survey of Semiconductor Physics* (Van Nostrand, New York, 1990).
[130] M. E. Lin, Z. Ma, F. Y. Huang, Z. F. Fan, L. H. Allen, and H. Morkoc, Appl. Phys. Lett. **64**, 1003 (1994).
[131] M. E. Lin, F. Y. Huang, and H. Morkoc, Appl. Phys. Lett. **64**, 2557 (1994).
[132] S. J. Pearton, C. R. Abernathy, F. Ren, J. R. Lothian, P. W. Wisk, and A. Katz, J. Vac. Sci. Technol. A **1**, 1772 (1993).
[133] S. J. Pearton, C. R. Abernathy, F. Ren, J. R. Lothian, P. Wisk, A. Katz, and C. Constantine, Semicond. Sci. Technol. **8**, 310 (1993).
[134] I. Adesida, A. Mahajan, E. Andideh, M. A. Khan, D. T. Olsen, and J. N. Kuznia, Appl. Phys. Lett. **63**, 2777 (1993).
[135] M. E. Lin, Z. F. Fan, Z. Ma, L. H. Allen, and H. Morkoc, Appl. Phys. Lett. **64**, 887 (1994).
[136] S. J. Pearton, C. R. Abernathy, and F. Ren, Appl. Phys. Lett. **64**, 2294 (1994).
[137] S. J. Pearton, C. R. Abernathy, and F. Ren, Appl. Phys. Lett. **64**, 3643 (1994).
[138] S. J. Pearton, C. R. Abernathy, F. Ren, and J. R. Lothian, J. Appl. Phys. **76**, 1210 (1994).
[139] S. J. Pearton, C. R. Abernathy, and C. B. Vartuli, Electron. Lett. **30**, 1985 (1994).
[140] S. J. Pearton, C. R. Abernathy, F. Ren, and J. R. Lothian, Mater. Res. Soc. Symp. Proc. **339**, 179 (1994).
[141] S. J. Pearton, C. B. Vartuli, R. J. Shul, and J. C. Zolper, Mater. Sci. Eng. B **31**, 309 (1995).
[142] A. T. Ping, I. Adesida, and M. A. Khan, Appl. Phys. Lett. **67**, 1250 (1995).

[143] H. Lee, D. B. Oberman, and J. S. Harris, Appl. Phys. Lett. **67**, 1754 (1995).
[144] M. A. Khan, J. N. Kuznia, D. T. Olson, J. M. Van Hove, M. Blasingame, and L. F. Reitz, Appl. Phys. Lett. **60**, 2917 (1992).
[145] M. A. Khan, J. N. Kuznia, D. T. Olson, M. Blasingame, and A. R. Bhattarai, Appl. Phys. Lett. **63**, 2455 (1993).
[146] M. A. Khan, Microwave J. **67** (November 1993).
[147] M. A. Khan, M. S. Shur, Q. Chen, J. N. Kuznia, and C. J. Sun, Electron. Lett. **31**, 398 (1995).
[148] M. S. Shur and M. A. Khan, Proc. SPIE **2397**, 294 (1995).
[149] K. S. Stevens, M. Kinniburgh, and R. Beresford, Appl. Phys. Lett. **66**, 3518 (1995).
[150] P. Kung, X. Zhang, D. Walker, A. Saxler, J. Piotrowski, A. Rogalski, and M. Razeghi (to be published).
[151] M. Misra, T. D. Moustakas, R. P. Vaudo, R. Singh, and K. S. Shah, Proc. SPIE **2519**, 78 (1995).
[152] Q. Chen, M. A. Khan, C. J. Sun, and J. W. Yang, Electron. Lett. **31**, 1781 (1995).
[153] B. Goldenberg, J. D. Zook, and R. J. Ulmer, in *Topical Workshop on III–V Nitrides Proc.* (North Holland, Nagoya, 1995).
[154] Y. Morimoto and S. Ushio, Jpn. J. Appl. Phys. **13**, 365 (1974).
[155] S. C. Binari, H. B. Dietrich, G. Kelner, L. B. Rowland, K. Doverspike, and D. K. Gaskill, Electron. Lett. **30**, 909 (1994).
[156] P. Hacke, T. Detchprohm, K. Hiramatsu, and N. Sawaki, Appl. Phys. Lett. **63**, 2676 (1993).
[157] J. D. Guo, M. S. Feng, R. J. Guo, F. M. Pan, and C. Y. Chang, Appl. Phys. Lett. **67**, 2657 (1995).
[158] X. Zhang, P. Kung, D. Walker, J. Piotrowski, A. Rogalski, A. Saxler, and M. Razeghi, Appl. Phys. Lett. **76**, 2028 (1995).
[159] M. A. Khan, J. N. Kuznia, D. T. Olson, W. Schaff, J. Burm, and M. S. Shur, Appl. Phys. Lett. **65**, 1121 (1994).
[160] M. Constant, D. Loridant, J. C. Camart, S. Meziere, L. Boussekey, and M. Chive, Proc. SPIE **2367**, 229 (1995).
[161] M. Misra, C. Zhou, P. B. Bennett, M. R. Squillants, and F. Ahmad, Proc. SPIE **2282**, 49 (1994).
[162] R. D. McKeag, S. S. M. Chan, and R. B. Jackman, Appl. Phys. Lett. **67**, 2117 (1995).
[163] G. M. Williams and M. M. Blouke, Laser Focus World **129** (September 1995).
[164] Compound Semiconductor **8** (Nov./Dec. 1995).
[165] Compound Semiconductor **9** (Nov./Dec. 1995).